DISCLAIMER

DOE/ET/34212-50
BAW-1874

October 1986
UC-78

THE HOT CELL EXAMINATION OF OCONEE 1 FUEL RODS AFTER FIVE CYCLES OF IRRADIATION

L. W. Newman
Project Engineer

DOE/ET/34212--50

DE87 002850

Prepared for

The United States Department of Energy
Under Contract DE-AC02-78ET34212

by

BABCOCK & WILCOX
Nuclear Power Division
P. O. Box 10935
Lynchburg, Virginia 24506-0935

BABCOCK & WILCOX
Research & Development Division
Lynchburg Research Center
P. O. Box 11165
Lynchburg, Virginia 24506-1165

Submitted by

BABCOCK & WILCOX
Contract Research Division
P. O. Box 835
Alliance, Ohio 44601

DUKE POWER COMPANY
P. O. Box 33189
Charlotte, North Carolina 28482

Babcock & Wilcox
a McDermott company

ACKNOWLEDGMENT

The work reported herein is the product of the efforts of many individuals at The Babcock & Wilcox Company, Duke Power Company, and The United States Department of Energy. The authors gratefully recognize their help and efforts in the Extended Burnup Program. In particular, the efforts of R. G. Snipes, J. D. Kortheuer, and T. Snead of Duke Power Company and Dr. P. M. Lang of The Department of Energy are acknowledged.

Principal Authors

L. W. Newman
T. P. Papazoglou
G. M. Bain
W. A. McInteer
T. D. Pyecha
P. L. Holman
P. C. Aadland

Babcock & Wilcox
Nuclear Power Division
Lynchburg, Virginia

Report BAW-1874

October 1986

The Hot Cell Examination of Oconee 1 Fuel Rods After Five Cycles of Irradiation

L. W. Newman

Key Words: UO2 Fuel, Zircaloy-4, Irradiation Testing, Fuel Performance, Fuel Cladding Performance

ABSTRACT

Babcock & Wilcox Mark B (15x15) fuel rods were examined in the hot cell after three, four, and five cycles of irradiation in the Oconee Unit 1 pressurized water reactor. The burnups of these rod groups were 31,940, 39,180, and 49,570 MWd/mtU, respectively. Nondestructive and destructive examinations were performed to gather fuel performance data, and to assess the impact of high burnup on key fuel and fuel rod characteristics. This effort is part of a Department of Energy program to improve uranium utilization and decrease the number of spent fuel assemblies discharged annually by extending the burnup of light water reactor fuel.

Of the fuel and fuel rod cladding phenomena investigated, fuel-cladding mechanical interaction, cladding waterside oxidation and hydrogen absorption, cladding mechanical properties, and fission gas release were identified as being the more significant concerns for implementing extended burnup. Of these phenomena, cladding waterside corrosion at burnups greater than 55,000 MWd/mtU remains the one with no immediate design solution. Advanced cladding designs are being developed, but require irradiation exposure and subsequent investigation to mitigate this concern.

CONTENTS

CONTENTS (Cont'd)

List of Tables

Tables (Cont'd)

List of Figures

Figures (Cont'd)

Figures (Cont'd)

1. INTRODUCTION

The Babcock & Wilcox Company (B&W) and Duke Power Company are participating in a United States Department of Energy (DOE) research and development program to qualify current design pressurized water reactor (PWR) fuel assemblies for extended burnup (>40,000 MWd/mtU).[1-9] The information obtained from this program will also provide a basis for future design improvements in light water reactor (LWR) fuel assemblies.[10-25] An extension of the current assembly design to higher burnups will result in the following benefits: (1) lower uranium ore requirements, (2) greater fuel cycle efficiency, (3) reduced spent fuel storage requirements, and (4) increased flexibility in tailoring fuel batch sizes to more effectively meet the varying energy requirements of utilities.

To obtain experimental information on the high burnup performance of Mark B (15x15) fuel assemblies, five assemblies were selected to undergo a fourth cycle of irradiation in cycle 5 of the Oconee Nuclear Station Unit 1 reactor. Four of the five assemblies were symmetrically located throughout their operating history. Each of the four achieved an assembly-average burnup of 31,500 MWd/mtU after three cycles of irradiation and 40,000 MWd/mtU after four cycles. The fifth assembly accumulated a slightly lower burnup of about 28,800 MWd/mtU after three cycles and 36,800 MWd/mtU after four cycles. One of the four symmetrically irradiated assemblies was reinserted in Oconee 1 cycle 7 and achieved a cumulative burnup of 50,160 MWd/mtU after five cycles of irradiation. Nondestructive examinations to characterize these high-burnup assemblies were conducted in the Oconee 1 and 2 spent fuel storage pool during the Oconee Unit 1 refueling outages for the end of cycles (EOCs) 4, 5, and 7.[26] Fuel rods were removed from a three-, four-, and five-cycle assembly for detailed nondestructive and destructive examinations in the hot cell facility at the B&W Lynchburg Research Center. These fuel rod groups have burnups of 31,940, 39,180, and 49,570 MWd/mtU.

This report presents detailed data from the hot cell examination of fuel rods from assembly 1D45 after five cycles of irradiation and summarizes the data for fuel rods examined after three and four cycles of irradiation.[27] Section 2 contains a summary of the results from the hot cell examinations. Secti 3 describes the Mark B assembly and the operating histories of the assemblies and fuel rods examined. Section 4 presents and discusses the results of the measurements and examinations conducted during the three-, four-, and five-cycle hot cell work. Section 5 discusses the potentially limiting trends observed at burnups beyond 40,000 MWd/mtU. The test scope of the five-cycle examination is summarized in Table 1-1.

Table 1-1. Workscope for the Hot Cell Examination of Five-Cycle Fuel Rods

Operation	Scope
Visual examination (section 4.2)	16 rods
Rod length measurements (section 4.3)	16 rods
Rod diameter profilometry (section 4.4)	16 rods
Fuel column gamma scans (section 4.5)	16 rods
Eddy-current oxide thickness (section 4.6)	16 rods
Eddy-current inspection (section 4.7)	16 rods
Plenum Kr-85 gamma scans (section 4.8)	16 rods
Fission gas analysis (section 4.9)	16 rods
Rod sectioning (section 4.10)	4 rods
Cladding examinations (section 4.11)	--
-Oxide thickness (section 4.11.1)	11 samples
-Hydrogen pickup (section 4.11.2)	11 samples
-Mechanical properties (section 4.11.3)	16 samples (8 axial, 8 ring)
-Unusual surface features (section 4.11.4)	--
-SEM characterization of cladding surface (section 4.11.5)	3 samples
Fuel examinations (section 4.12)	--
-Microstructure (section 4.12.1)	10 samples
-Density (section 4.12.2)	12 samples
-Radial fission product migration (section 4.12.3)	18 samples
-Chemical burnup (section 4.12.4)	5 samples

2. SUMMARY

This report summarizes the results of the hot cell examinations of fuel rods from Mark B (15x15) fuel assemblies discharged from the Oconee 1 reactor after completing three, four, and five cycles of irradiation with assembly-average burnups of 31,500, 40,000 and 50,160 MWd/mtU, respectively. The examinations were conducted in support of a Department of Energy-sponsored Extended Burnup Program that includes the qualification of current design PWR fuel assemblies for burnups on the order of 50,000 MWd/mtU. The fuel performance data gathered in this program are being used to support the routine irradiation of PWR assemblies to higher burnups and to enlarge the fuel performance data base for future design improvements in LWR fuel assemblies.

A standard B&W fuel assembly was subjected to a wide variety of nondestructive and destructive tests following five cycles of irradiation. In general, the test program confirmed the soundness of the Mark B design to high burnups. Key results were as follows:

1. The growth rate of the fuel column, the fuel rod, and the oxide layer each increased during the fifth cycle as compared with the fourth. However, these factors produced no adverse effects on fuel performance.
2. Rod diameter scans, after correcting for the oxide layer, were essentially unchanged from the four-cycle values. This indicates that fuel pellet swelling is not significantly affecting the cladding diametral strain.
3. Eddy-current flaw scanning on 16 rods showed no indication of cladding defects, and rod puncturing confirmed that all rods were sound.
4. Fractional fission gas release remained low (below 4% for all 16 rods), and increased slightly (0.1% on the average) during the fifth cycle.

5. Cladding hydrogen concentrations ranged from about 100 to 400 ppm. Essentially all zirconium hydride platelets were circumferentially oriented.

6. Cladding mechanical tests showed that tensile strength changed little during the fifth cycle, but that elongation continued to decrease.

7. Fuel density and fuel column growth data showed that fuel swelling occurs primarily in the axial direction, with little or no diametral change.

8. Fuel and cladding microstructural examinations revealed nothing unusual, except for a more obvious reaction zone at the fuel-cladding interface. Fuel grain growth was minimal through five cycles of irradiation.

Post-irradiation examinations through 50,000 MWd/mtU have identified two areas of concern when routinely irradiating batches of fuel assemblies to this burnup level. These concerns are the pellet-cladding reaction zone (and its effect on fuel rod growth and performance) and cladding waterside oxidation and hydriding conditions (and their effects on cladding ductility). Additional data in these areas are needed to model and predict confidently their extended burnup behavior. Design changes that impart a greater margin for operation can be made to alleviate these concerns -- changes such as increased assembly length or reduced fuel rod lengths, and thicker cladding may permit irradiation to 55,000 MWd/mtU. Advanced cladding types may also reduce these concerns, and development and investigations should continue in this area.

3. MARK B DESIGN DESCRIPTION AND ASSEMBLY OPERATING HISTORIES

3.1. Introduction

One portion of the DOE/Duke/B&W Extended Burnup Program is to demonstrate the high burnup capability (approximately 50,000 MWd/mtU) of the standard Mark B fuel assembly. To accomplish this task, several fuel assemblies were irradiated for additional cycles and then examined to evaluate their performance. After three cycles of irradiation,[28] five standard Mark B assemblies were selected for a fourth cycle of irradiation in Oconee 1 cycle 5 and achieved an average burnup of about 40,000 MWd/mtU. A poolside nondestructive examination on all five assemblies[29] was performed in conjunction with a destructive hot cell examination on selected rods of one assembly.[27] One of these four-cycle assemblies (1D45) was selected for a fifth cycle of irradiation in Oconee 1 cycle 7.

Fuel assembly 1D45, a standard Mark B assembly, completed its fifth cycle of irradiation in June 1983. This assembly achieved 50,160 MWd/mtU burnup during 1553 effective full power days (EFPDs) of incore residence. A general description of the Mark B assembly and an irradiation summary of assembly 1D45 are presented in section 3.2.

3.2. Mark B Assembly Description -- Irradiation History of Assembly 1D45

Duke Power Company's Oconee Unit 1 is a B&W-designed PWR with a core composed of 177 Mark B (15x15) fuel assemblies. The structural cage of the assembly comprises 16 control rod guide tubes (CRGTs) of cold-worked, stress-relieved, Zircaloy-4 permanently attached to the upper and lower end fittings. The Inconel 718 spacer grids form the structural link between the guide tubes and the fuel rods (cold-worked, stress-relieved, Zircaloy-4 cladding), but are free to move with the fuel rods as the rods grow. For reference, the six intermediate spacer grids are numbered sequentially from 1 to 6 (from top to

bottom), and the grid span levels are numbered from 1 to 7 as shown in Figure 3-1. Fuel assembly lift resulting from coolant flow is prevented by the helical holddown spring in the upper end fitting of the assembly.

Figure 3-1. Mark B Fuel Assembly

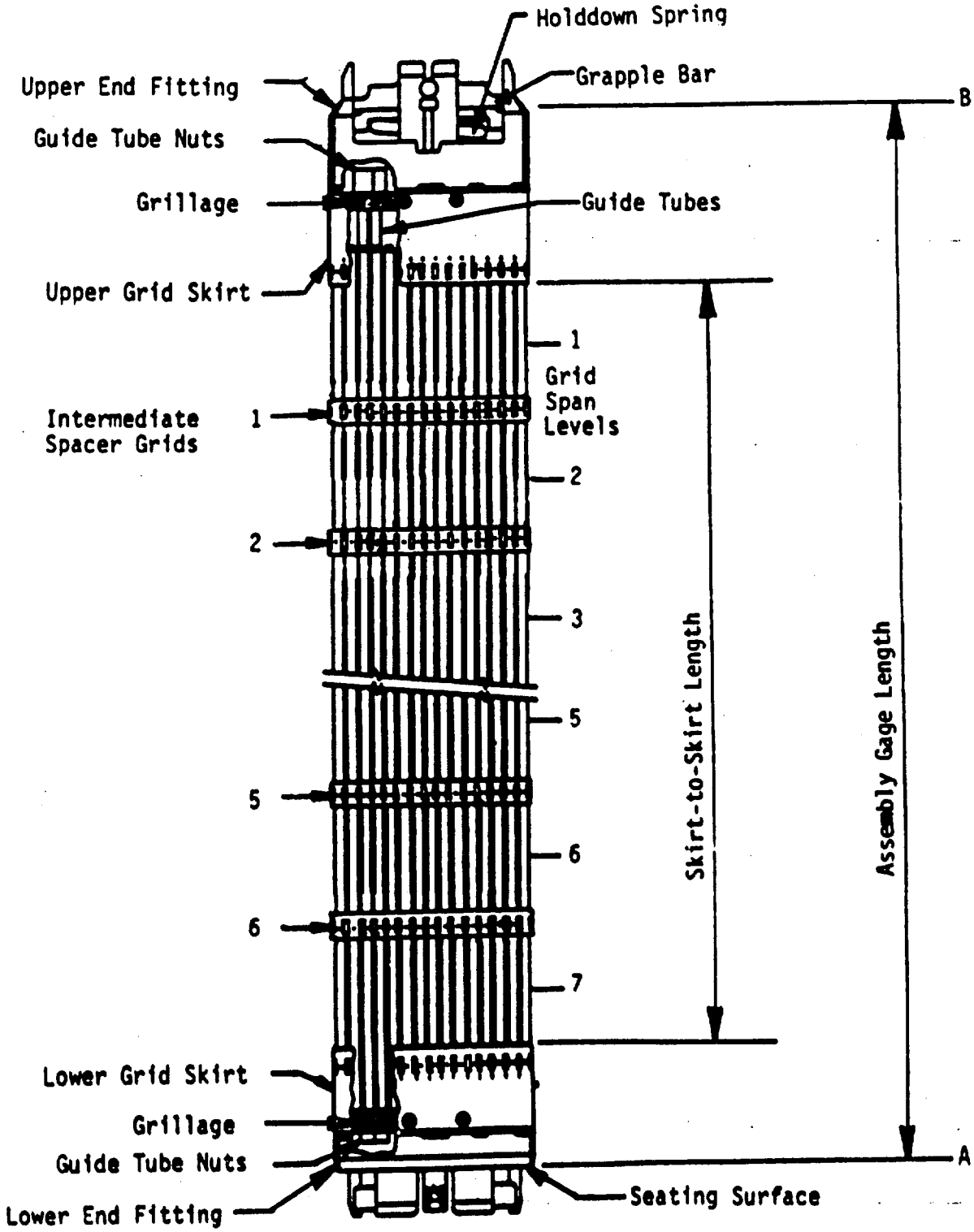

Each fuel assembly consists of a 15x15 lattice arrangement with 16 positions occupied by guide tubes and one position, the center lattice site, occupied by an incore instrumentation tube. The remaining 208 lattice positions contain fuel rods. Figure 3-2 is a schematic cross section of a typical fuel assembly showing the fuel rod numbering convention for peripheral rods. The fuel in the rods is enriched UO_2 in the form of dished and chamfered cylindrical pellets (sintered). The nominal design parameters and operating conditions of Oconee 1 fuel are summarized in Table 3-1.

Table 3-1. Oconee 1 Nominal Fuel Design Parameters[a]

Reactor core	
Core power rating, MWt	2568
Core average linear heat rate, kW/ft	5.78
Core inlet coolant temperature, F	555
Core outlet coolant temperature, F	606
Core operating pressure, psia	2200
Fuel assemblies and fuel rods	
Number of fuel assemblies in core	177
Number of fuel rods per fuel assembly	208
Number of CRGTs per assembly	16
Fuel rod outside diameter, in.	0.430
Fuel tubing (cladding) thickness, in.	0.0265
Fuel rod pitch, in.	0.568
Fuel assembly pitch, in.	8.587
Fuel	
Material	UO_2 (sintered)
Fuel pellet length, in.	0.70
Fuel pellet diameter, in.	0.3670
Active fuel length, in.	141.0
Fuel density, % theoretical	95.0

[a] Design parameters are for Oconee 1 cycle 2, the first cycle of irradiation for assembly 1D45.

Figure 3-2. Fuel Assembly Cross Section Displaying Numbering Convention

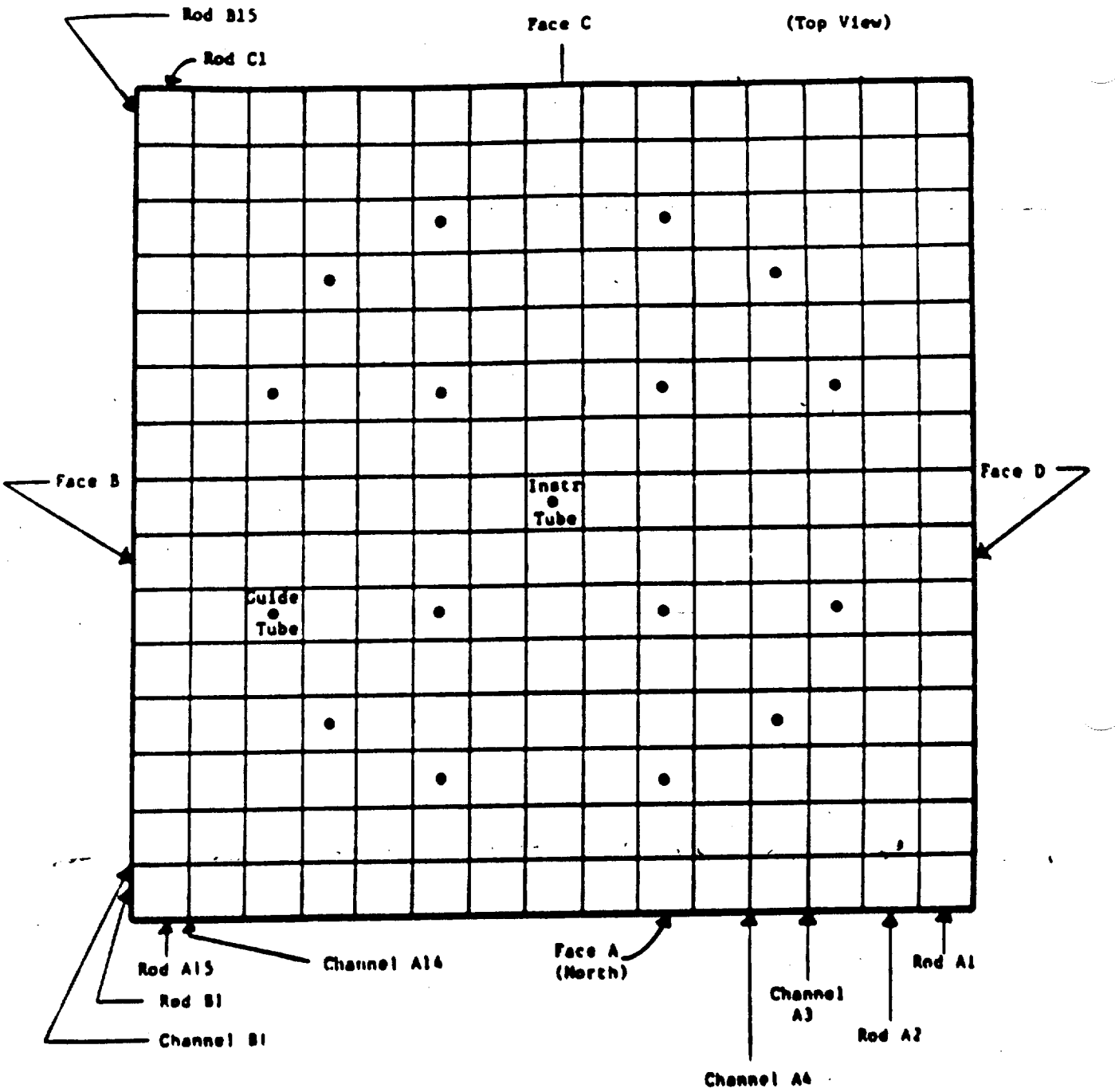

Assembly 1D45 was inserted in Oconee 1 during the EOC-1 refueling outage. The assembly was irradiated in cycles 2, 3, 4, 5, and 7. The core location of this assembly during each of the five cycles is shown on the core map in Figure 3-3. Assembly 1D45 achieved an assembly-average burnup of 50,160 MWd/mtU during its incore residence time of 1553 EFPDs.

The reactor power histories for Oconee 1 cycles 2 through 5 and 7 and physics data for assembly 1D45 are given in Appendix A.

Assembly burnups and fast neutron (E>1 MeV) fluences were calculated using the PDQ07[30] and FLAME[31] computer codes. Assembly-average burnups and fast fluences at the end of each cycle for the high-burnup assembly are given in Table 3-2.

The maximum and minimum fuel rod burnups calculated with PDQ07 were 50,957 and 49,480 MWd/mtU, respectively. Axial power profiles for assembly 1D45 were relatively flat in the central portion of the assembly (from 20 to 120 inches in the active fuel region), with the characteristic decrease toward the ends of the fuel column. Figure 3-4 displays the relative average axial power profile for assembly 1D45 at the end of each of its cycles.

These axial shapes do not include flux depressions caused by spacer grids. Assembly 1D45 contained a partially inserted control rod cluster during its first and second cycle of irradiation. Also, in its second and third cycles of irradiation, assembly 1D45 was positioned diagonally adjacent to a fuel assembly having axial power shaping rods (APSRs). The result of this positioning is to shift power to the lower portion of the assembly (control rod effect) and to depress power in the center of the assembly with an accompanying increase at the 20- and 120-inch levels (APSR effect). These combined effects are carried throughout assembly 1D45's lifetime, causing the highest burnup to occur in the lower portion of the assembly as shown in Figure 3-5.

Figure 3-3. Location of Extended Burnup Assembly 1D45 During Each Cycle of Irradiation

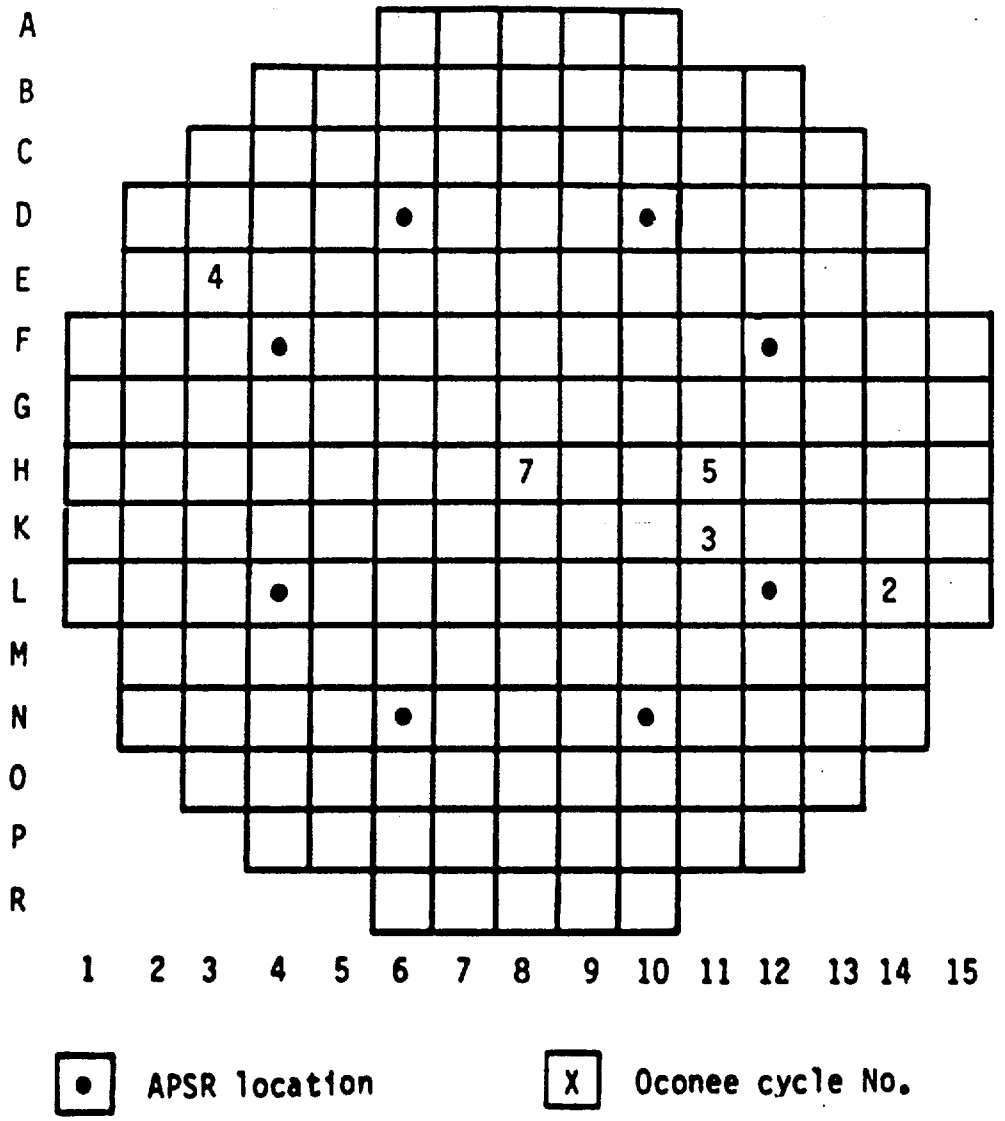

Assembly 1D45 cycle	Oconee 1 cycle
1	2
2	3
3	4
4	5
5	7

Table 3-2. Assembly-Average Burnups and Fluences -- Oconee 1, EOCs 2 Through 5 and 7

Assembly cycle	Reactor cycle	Core location	Cycle length, EFPD	Average burnup, MWd/mtU	Fluence, n/cm^2 >1 MeV
1	2	L14	292.2	12,267	1.799×10^{21}
2	3	K11	308.3	24,281	3.807×10^{21}
3	4	E3	245.9	31,459	5.164×10^{21}
4	5	H11	303.6	39,949	6.874×10^{21}
5	7	H8	403.3	50,160	9.172×10^{21}

Figure 3-4. Cycles[(a)] 1 Through 5 Average Axial RPD Profile -- Assembly 1D45

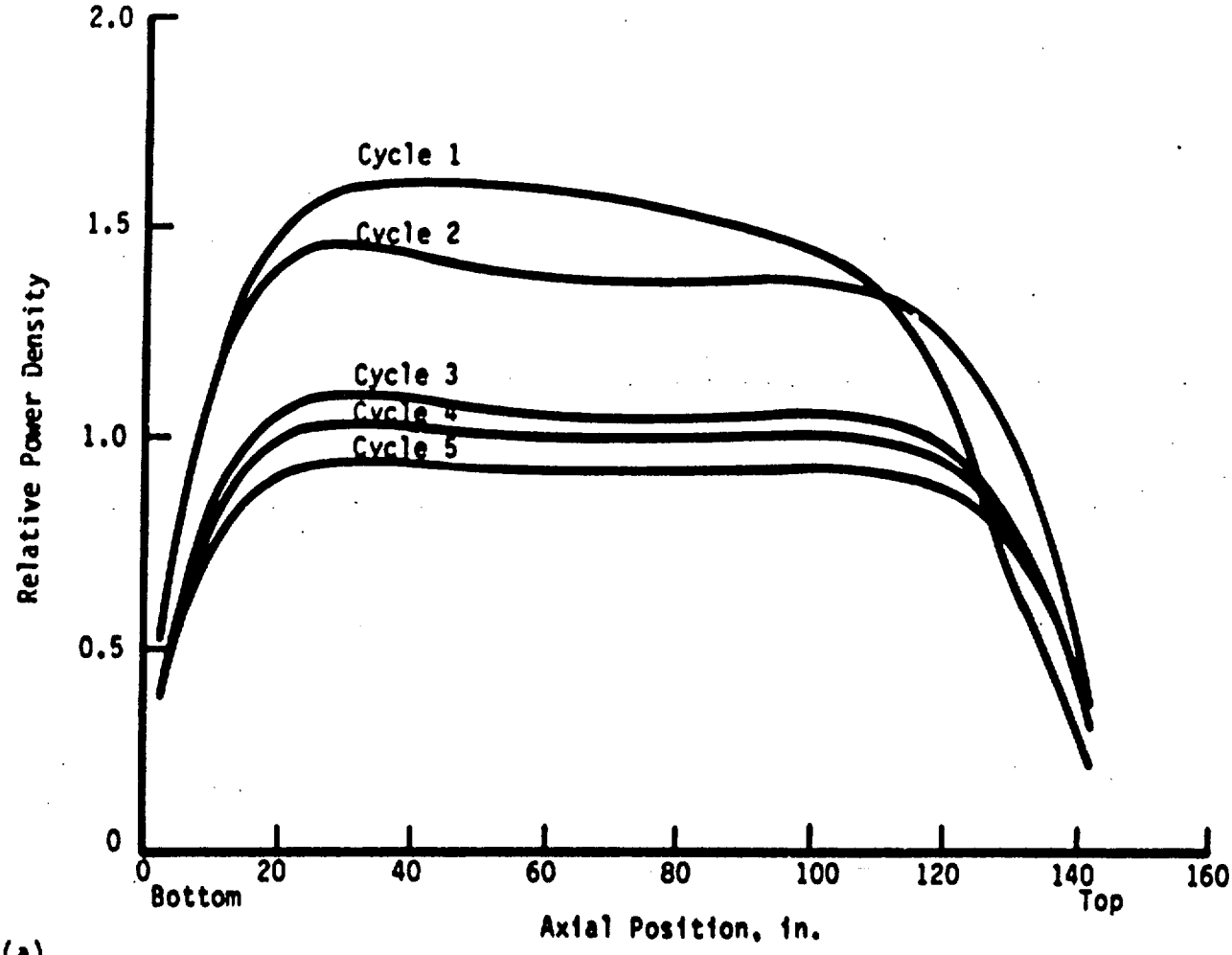

[(a)]Denotes assembly cycle.

Figure 3-5. Calculated Assembly-Average Axial Burnup Profile -- Assembly 1D45 at the EOC 7

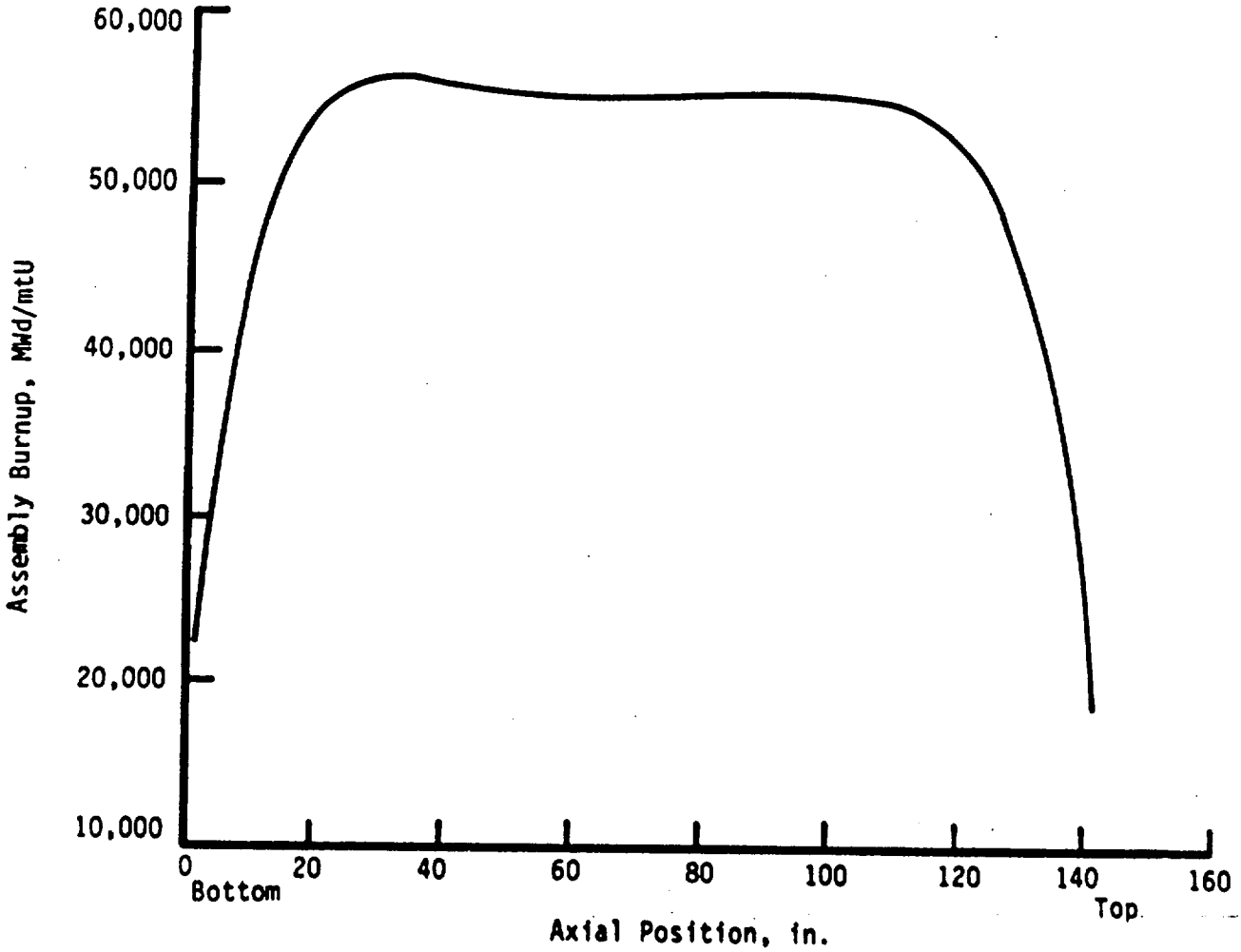

4. HOT CELL EXAMINATION OF RODS FROM FIVE-CYCLE ASSEMBLY 1D45

4.1. Introduction

Hot cell examinations were conducted on 16 peripheral rods removed from the five-cycle fuel assembly 1D45. The scope of the hot cell examination is shown in Table 4-1.

The rods selected for examination are identified in Figure 4-1, which shows a plan view schematic of assembly 1D45. Selection criteria for these rods were as follows:

1. The four corner rods due to the more extensive data already available on these rods from previous poolside examinations.
2. Seven face C rods (non-corner) due to an unusual region of spots with a blistered appearance.
3. Two face D rods, D2 and D3, that operated in near contact due to bow during the fourth and fifth cycles of irradiation.
4. Three face B rods, B12 through B14, because their locations corresponded to those of rods extracted for hot cell examination from the four-cycle sister assembly 1D13.

Each hot cell operation is discussed and results are presented in the ensuing sections. The nondestructive examinations are discussed in sections 4.2 through 4.9 and the destructive examinations in sections 4.10 through 4.12.

4.2. Visual Examination

All 16 rods from assembly 1D45 were examined in the hot cell using closed-circuit television (CCTV) and optical periscope methods. Television scans were taken along the full length of each rod in two orientations 180 degrees apart, and videotapes were made of all the scans. Additionally, particular areas were examined with the in-cell periscope and documented with photographs.

Table 4-1. Workscope for the Hot Cell Examination of Five-Cycle Fuel Rods

Operation	Scope
Visual examination (section 4.2)	16 rods
Rod length measurements (section 4.3)	16 rods
Rod diameter profilometry (section 4.4)	16 rods
Fuel column gamma scans (section 4.5)	16 rods
Eddy-current oxide thickness (section 4.6)	16 rods
Eddy-current inspection (section 4.7)	16 rods
Plenum Kr-85 gamma scans (section 4.8)	16 rods
Fission gas analysis (section 4.9)	16 rods
Rod sectioning (section 4.10)	4 rods
Cladding examinations (section 4.11)	--
- Oxide thickness (section 4.11.1)	11 samples
- Hydrogen pickup (section 4.11.2)	11 samples
- Mechanical properties (section 4.11.3)	16 samples (8 axial, 8 ring)
- Unusual surface features (section 4.11.4)	--
- SEM characterization of cladding surface (section 4.11.5)	3 samples
Fuel examinations (section 4.12)	--
- Microstructure (section 4.12.1)	10 samples
- Density (section 4.12.2)	12 samples
- Radial fission product migration (section 4.12.3)	18 samples
- Chemical burnup (section 4.12.4)	5 samples

Figure 4-1. Assembly 1D45 Rods for Hot Cell Examination

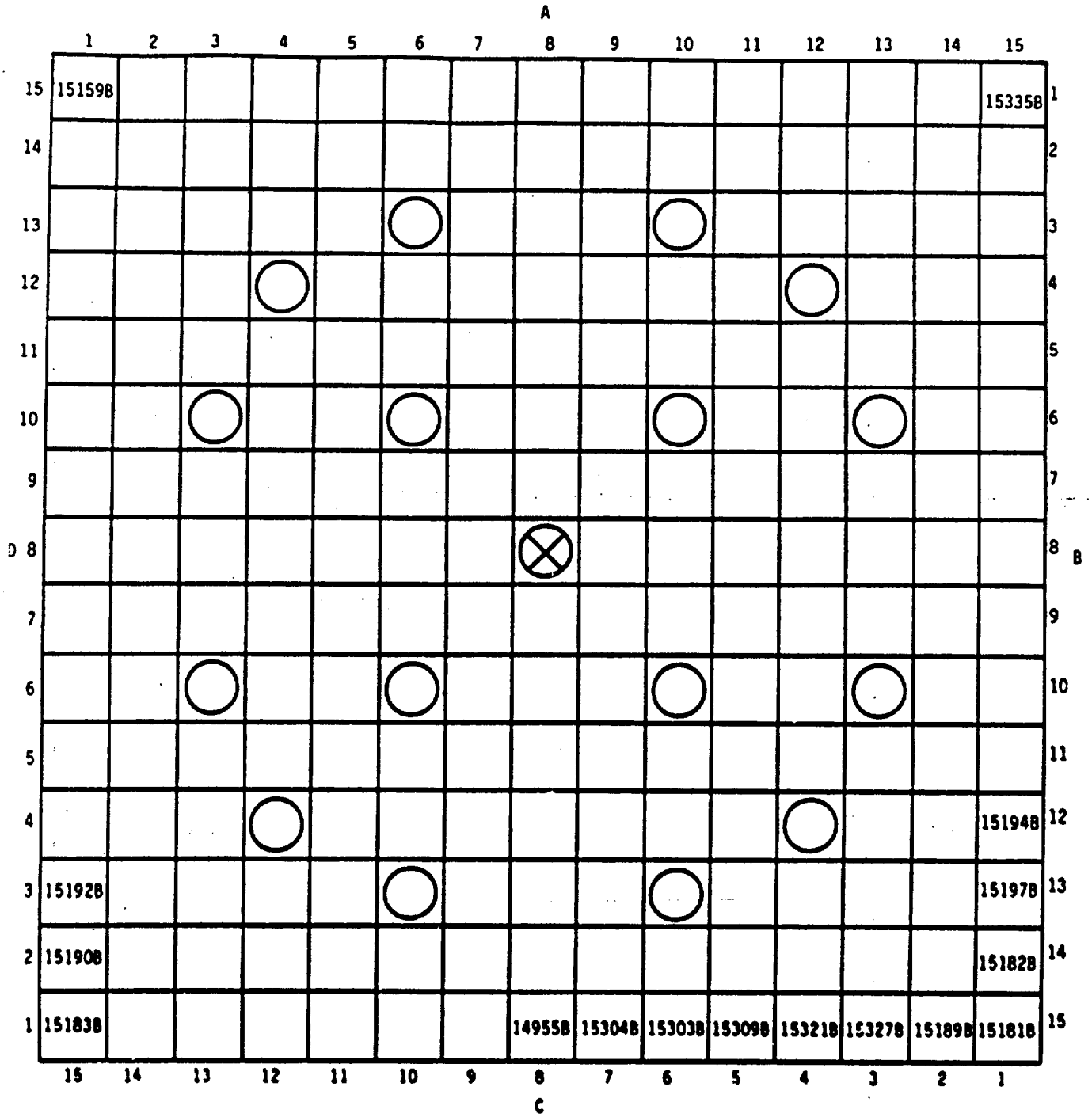

In general, the rods appeared to be in good condition. Crud patterns were somewhat marked on the upper 20% of the rod surface, while the remainder was mostly light and uniform. Dark circumferential bands at the pellet interfaces were not as obvious as they appeared in the poolside examinati No evidence of either rod defects or cladding distortion was observed. Two anomalous areas were examined in detail: a region of spots with a blistered appearance (in the six inches or so below the first intermediate grid), and a region of near contact between two rods in span 5 (between grids 4 and 5).

The majority of the spots were located in the upper part of span 2 on the face C rods. The most interesting areas were found on rods C7 and C8, which are shown in Figure 4-2. Many of the spots had a fairly regular shape, either circular or elliptical, and revealed no large relief; profilometry showed a slight protrusion. A few similar spots were seen on rods C3, C5, C15, and B12 at the same general axial location. The other rods with spots, including other face C rods, did not show the same degree of regularity in the markings. Further hot cell testing revealed these anomalous surface features to be waterside oxidation (see section 4.11).

Rods D2 and D3 were in near contact at about 95 inches from the top of the rods, as shown in the photomosaic in Figure 4-3. Although the photogra appear to show relief in the surface features, inspection and profilometry indicated that the protrusion was minimal. These areas were also subjected to further hot cell analyses (see section 4.11).

Except for the near-contact region and the spotted areas, the features on the rods were typical of rods examined after three and four cycles of irradiation. Examples of the general appearance are given in Figure 4-4, which shows clean areas and fading dark bands in the lower two-thirds of the rods.

4.3. Rod Length Measurements

The length of each fuel rod was determined by measuring the difference in elevation between a standard rod of known length and the fuel rod when placed in the same storage basket hole. No correction was made for either rod bow or thermal effects. These errors are small due to the lateral constraint on the rods and a negligible temperature difference. The estimated uncertainty in the measured growth of the rods is ±0.025 inches, or 0.016% $\Delta L/L_0$.

Figure 4-2. Spotty Region on Rods C7 and C8 After Five Cycles of Irradiation

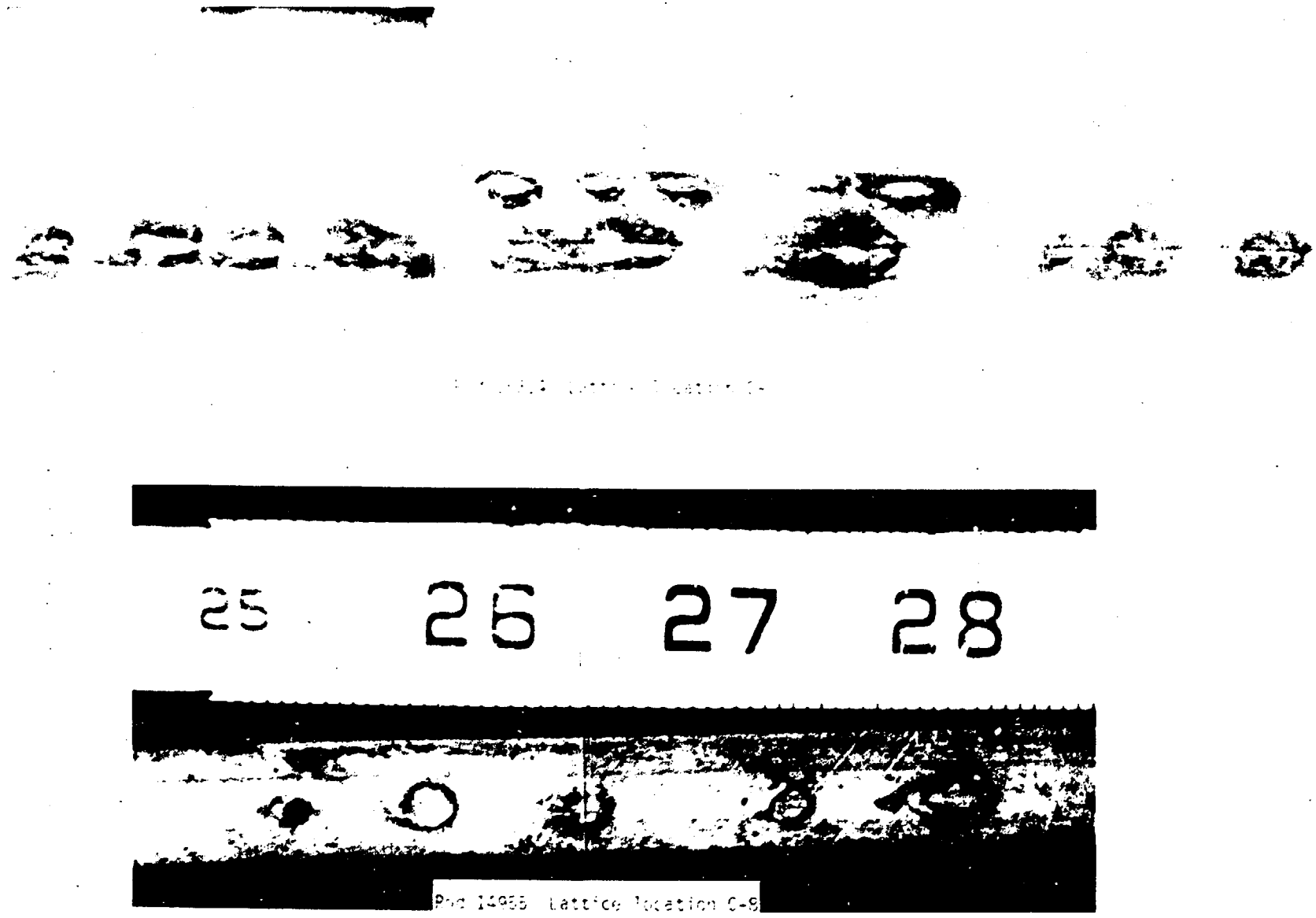

Figure 4-3. Bowed to Near-Contact Rods D2 and D3 After Five Cycles of Irradiation

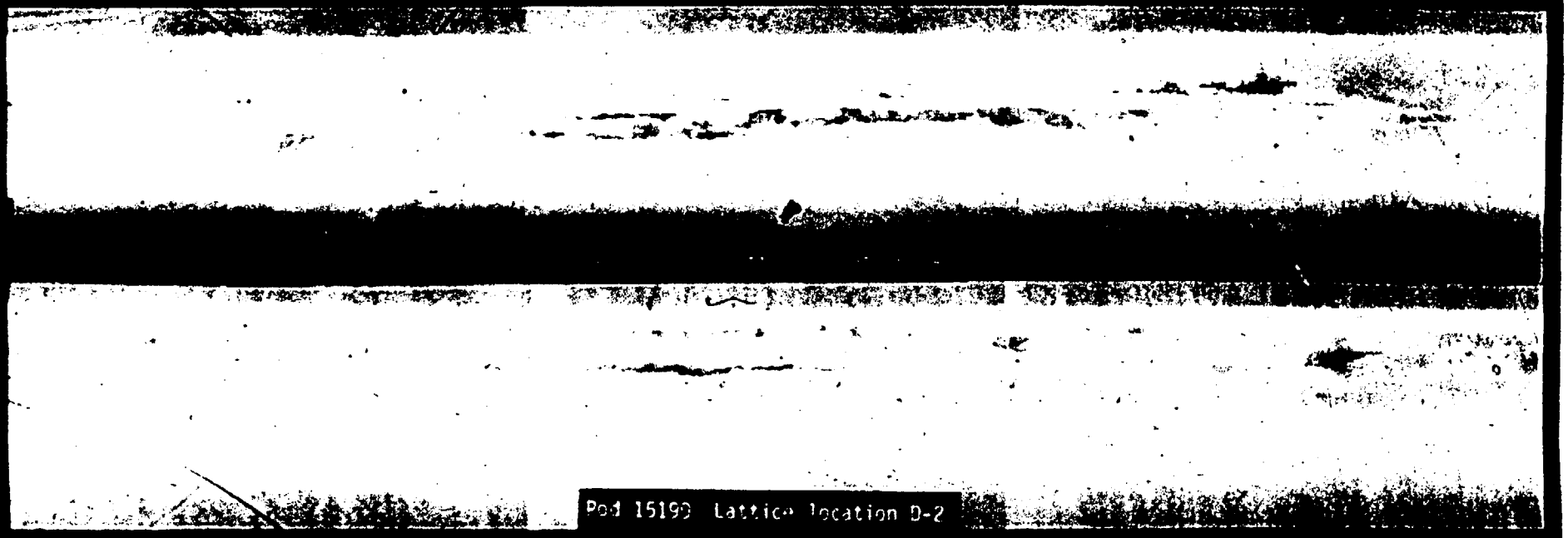

Figure 4-4. Typical Crud Pattern in the Lower Two-Thirds of the Fuel Rods After Five Cycles of Irradiation

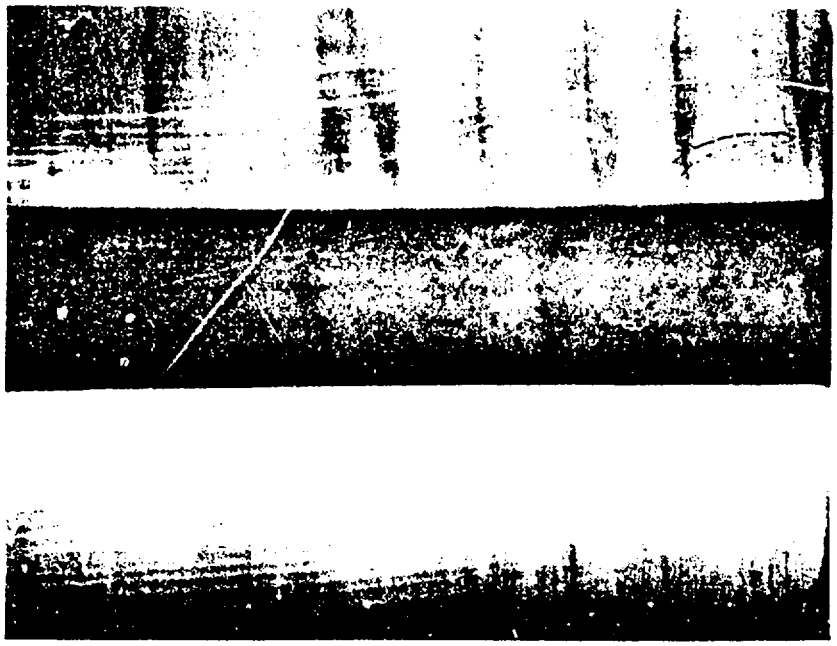

Rod 15321 Lattice location C-4

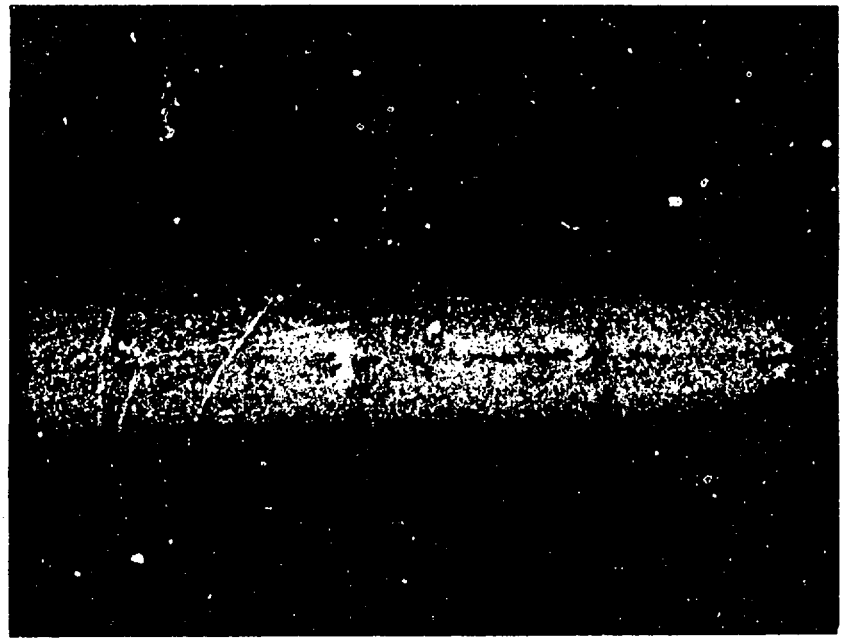

Rod 15321 Lattice location C-4

Table 4-2 shows the length and growth determined for each rod extracted from assembly 1D45. In Figure 4-5, the data are plotted as a function of fast neutron fluence, along with earlier hot cell data on rods from Oconee Units 1 and 2. Rod growth for the five-cycle rods ranged from 0.79 to 0.91% $\Delta L/L_o$ with an average of 0.85% $\Delta L/L_o$ for the 16 rods. A least-squares line through the data set in Figure 4-5, excluding the latest five-cycle data, shows a good linear fit through the origin and has a slope of about 0.075% $\Delta L/L_o$ per 10^{21} n/cm^2 (E>1 MeV). However, the five-cycle data clearly show an increase in the growth rate at burnups >40,000 MWd/mtU (6.875 x 10^{21} n/cm^2, E>1 MeV). Based on an extrapolation of the heretofore linear growth rate, the five-cycle rods are expected to have an average axial growth of about 0.66% -- about 0.19% lower than the measured axial growth of 0.85%. This additional axial growth is attributed to the effects of fuel-cladding mechanical interaction in conjunction with fuel swelling at high burnups. These factors also affected the cladding diameter and pellet stack elongation of these rods, which are discussed further in sections 4.4 and 4.5.

4.4. Rod Diameter Profilometry

Fuel rod outside diameters were measured with a contacting linear variable differential transducer (LVDT) profilometry system. Data were recorded at 0.050-inch axial increments from full-length linear diameter scans taken at four azimuthal orientations, 45 degrees apart. The four measured diameters were used to calculate maximum, minimum, and average diameters and the rod ovality (maximum diameter minus minimum diameter) at each axial increment. Reference 6 provides more details concerning the method.

The profilometry data indicate that the height and axial extent of pellet-to-pellet interface ridges caused by pellet-to-cladding interaction increased during the fifth cycle. Typical diameter scans from three-, four-, and five-cycle rods are shown in Figure 4-6. The axial extent of hard contact increased during the fifth cycle to include the region from 15 to 120 inches from the bottom of the rod. The figure shows that this region of hard contact on the five-cycle rod extends approximately 10 inches above that of the three-cycle rod and about 10 inches below that of the four-cycle rod.

Table 4-2. Fuel Rod Length Results

Rod No.	Location in FA	Average burnup, MWd/mtU	Average fluence (E>1MeV), 10^{21} n/cm^2	Length (L), in.	Change[(a)] in length (ΔL), in.	Growth,[(a)] % $\Delta L/L_o$
15335	B1	49,493	8.78	154.904	1.217	0.792
15159	A1	49,493	8.78	154.944	1.257	0.818
15183	D1	49,493	8.78	154.997	1.310	0.852
15182	B14	49,493	8.78	154.910	1.223	0.795
15197	B13	49,922	8.88	154.995	1.308	0.851
15194	B12	49,922	8.88	154.975	1.288	0.838
15192	D3	49,933	8.88	155.013	1.326	0.863
15190	D2	49,493	8.78	154.983	1.296	0.843
14955	C8	49,494	8.78	155.057	1.370	0.891
15309	C5	49,480	8.78	155.053	1.366	0.889
15303	C6	49,480	8.78	155.081	1.394	0.907
15321	C4	49,480	8.78	155.063	1.376	0.895
15181	C1	49,493	8.78	154.904	1.217	0.792
15327	C3	49,480	8.78	155.036	1.349	0.877
15189	C2	49,493	8.78	154.978	1.291	0.840
15304	C7	49,494	8.78	155.031	1.344	0.874
Average	--	49,570	8.80	154.995	1.308	0.851

(a) The change and growth are based on the nominal beginning-of-life (BOL) length, L_o = 153.6875 in.

Figure 4-5. Individual Fuel Rod Axial Growth Vs Rod-Average Fast Fluence, Hot Cell Measurements

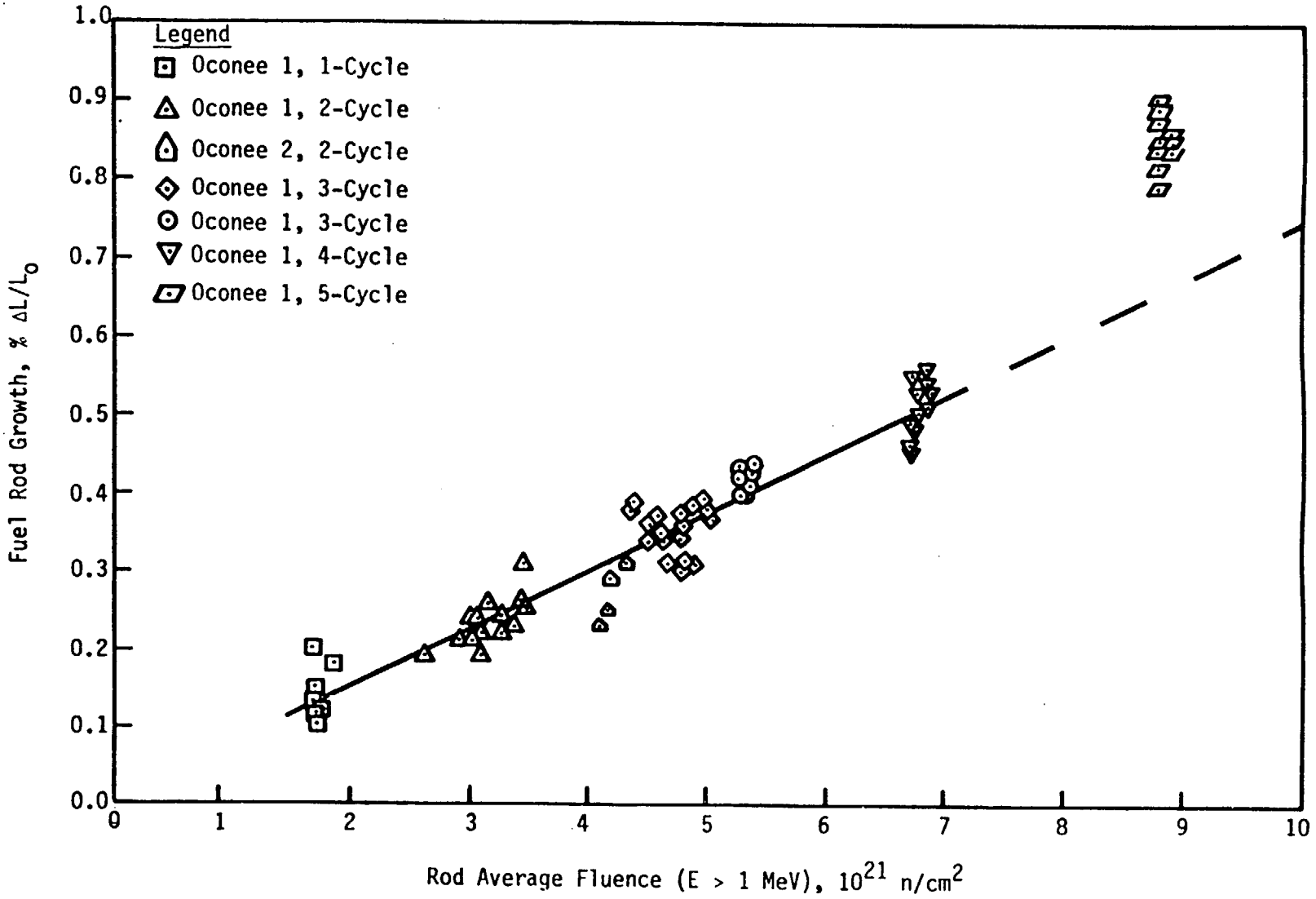

Figure 4-6. Typical Linear Diameter Scans from Three-, Four-, and Five-Cycle Fuel Rods

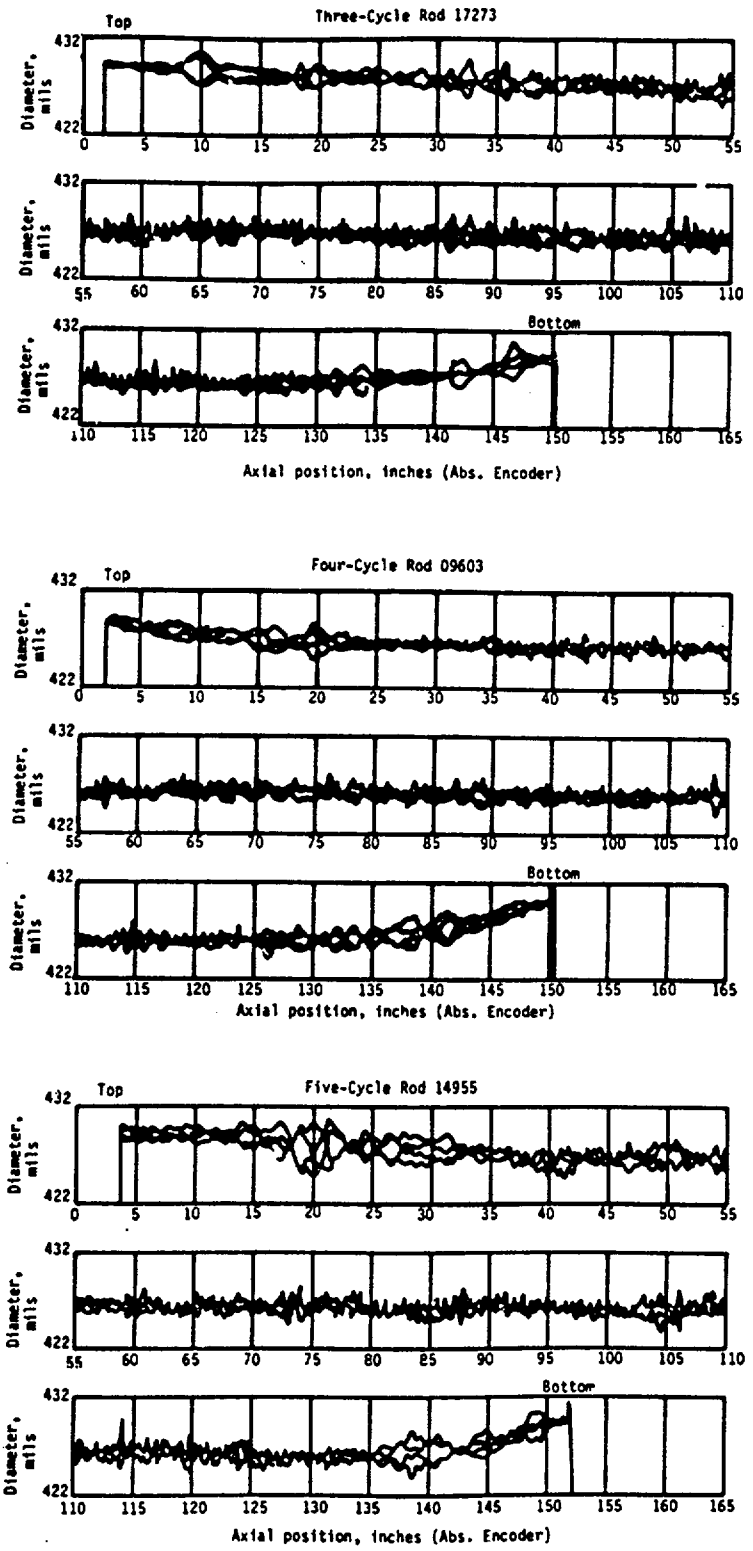

The five-cycle profilometry data indicate harder pellet-to-cladding contact with ridge heights about 1 mil greater than typical four-cycle values.

Rod span-average diameters with and without correction for oxide thickness are given in Table 4-3. The composite average diameter (uncorrected) for the 16 five-cycle rods was 0.4268 inch (Table 4-4), which is 0.5 mil greater than that for the four-cycle rods from sister assembly 1D13. This is consistent with four- and five-cycle poolside results, which indicate that the 1D45 rod average diameter increased by 0.7 mil during the fifth cycle.

The diameter increase during the fifth cycle is attributed to an increase in oxide thickness (see Table 4-4). Oxide thickness is discussed in section 4.11.1. When diameter measurements are corrected for oxide thickness, the diameters of the four- and five-cycle rods are nearly equal. The corrected rod diameters for the four- and five-cycle rods are shown in Figure 4-7. Thus, creepdown during the fifth cycle of irradiation is minimal, and fuel swelling in the radial direction has not overcome the compressive forces of the cladding.

Diameter data not corrected for oxide thickness were averaged over span lengths equivalent to those measured in the poolside examinations; the results are given in Table 4-3 and shown in Figure 4-8. Average results for the individual rod spans were generally in good agreement with poolside values. Figure 4-8 shows that the 16-rod average is skewed toward the minimum in spans 3, 4, and 5. This implies that the hardest pellet-to-cladding contact occurred over this region (about 60 inches). Based on fifth-cycle fuel column elongation, hard cladding contact with the fuel for 60 inches would result in an additional rod growth of about 0.36 inch (0.23%). This additional elongation is consistent with the observed 0.19% rod growth increase over that predicted from previous growth data.

More detailed profilometry was performed on the spotty features observed below the first intermediate spacer grid on the face C rods and over the near-contact region of bowed rods D2 and D3. Linear scans at 10-degree increments and full circumference measurements at small axial increments were made to determine the dimensions of these unusual features noted during the visual examination of the rods. The spotty patterns observed on the face C rods were found to be raised from the surface by 1.0 to 1.5 mils. An example

Table 4-3. Five-Cycle Span-Average Diameters

FA location	Rod No.	Poolside equivalent span diameter, in. 1	2	3	4	5	6	7
AB corner	15335	0.4277 (0.4268)	0.4274 (0.4264)	0.4272 (0.4263)	0.4267 (0.4259)	0.4264 (0.4257)	0.4263 (0.4257)	0.4265 (0.4261)
B12	15194	0.4277 (0.4266)	0.4274 (0.4261)	0.4276 (0.4264)	0.4274 (0.4264)	0.4264 (0.4256)	0.4262 (0.4255)	0.4263 (0.4259)
B13	15197	0.4277 (0.4266)	0.4275 (0.4263)	0.4272 (0.4260)	0.4267 (0.4257)	0.4260 (0.4252)	0.4260 (0.4253)	0.4262 (0.4258)
B14	15182	0.4276 (0.4266)	0.4270 (0.4259)	0.4268 (0.4258)	0.4264 (0.4255)	0.4262 (0.4254)	0.4260 (0.4253)	0.4264 (0.4260)
BC	15181	0.4271 (0.4262)	0.4268 (0.4258)	0.4269 (0.4260)	0.4267 (0.4259)	0.4265 (0.4258)	0.4266 (0.4259)	0.4267 (0.4263)
C2	15189	0.4273 (0.4264)	0.4269 (0.4258)	0.4266 (0.4256)	0.4265 (0.4256)	0.4260 (0.4252)	0.4258 (0.4252)	0.4261 (0.4257)
C3	15327	0.4281 (0.4270)	0.4276 (0.4263)	0.4271 (0.4260)	0.4269 (0.4259)	0.4264 (0.4256)	0.4264 (0.4257)	0.4265 (0.4261)
C4	15321	0.4283 (0.4270)	0.4275 (0.4261)	0.4270 (0.4258)	0.4268 (0.4258)	0.4265 (0.4256)	0.4264 (0.4256)	0.4264 (0.4260)
C5	15309	0.4280 (0.4266)	0.4272 (0.4258)	0.4267 (0.4255)	0.4264 (0.4253)	0.4260 (0.4252)	0.4260 (0.4252)	0.4261 (0.4257)
C6	15303	0.4284 (0.4271)	0.4277 (0.4264)	0.4273 (0.4261)	0.4269 (0.4259)	0.4265 (0.4257)	0.4265 (0.4257)	0.4268 (0.4264)
C7	15304	0.4282 (0.4270)	0.4274 (0.4262)	0.4271 (0.4260)	0.4266 (0.4256)	0.4262 (0.4254)	0.4261 (0.4254)	0.4263 (0.4259)
C8	14955	0.4283 (0.4269)	0.4272 (0.4259)	0.4267 (0.4256)	0.4263 (0.4253)	0.4262 (0.4254)	0.4262 (0.4255)	0.4263 (0.4260)
CD	15183	0.4271 (0.4261)	0.4266 (0.4255)	0.4265 (0.4255)	0.4262 (0.4254)	0.4260 (0.4253)	0.4261 (0.4254)	0.4263 (0.4259)
D2	15190	0.4277 (0.4267)	0.4272 (0.4261)	0.4267 (0.4257)	0.4266 (0.4257)	0.4260 (0.4252)	0.4263 (0.4256)	0.4265 (0.4261)
D3	15192	0.4279 (0.4268)	0.4272 (0.4261)	0.4266 (0.4256)	0.4262 (0.4254)	0.4260 (0.4252)	0.4260 (0.4253)	0.4264 (0.4260)
AD corner	15159	0.4266 (0.4256)	0.4266 (0.4254)	0.4265 (0.4254)	0.4265 (0.4256)	0.4260 (0.4252)	0.4261 (0.4254)	0.4263 (0.4259)
Composite Average		0.4277 (0.4266)	0.4272 (0.4260)	0.4269 (0.4258)	0.4266 (0.4257)	0.4262 (0.4254)	0.4262 (0.4255)	0.4264 (0.4260)

Note: Numbers in parentheses are corrected for oxide thickness.

Table 4-4. Five-Cycle Rod-Average Diameters

Fuel Rod	Average diameter, in. Uncorrected	Corrected	Creepdown, mils
14955	0.4268	0.4258	4.2
15159	0.4265	0.4255	4.5
15181	0.4269	0.4260	4.0
15182	0.4267	0.4258	4.2
15183	0.4265	0.4256	4.4
15189	0.4266	0.4256	4.4
15190	0.4268	0.4259	4.1
15192	0.4267	0.4258	4.2
15194	0.4271	0.4261	3.9
15197	0.4268	0.4258	4.2
15303	0.4272	0.4262	3.8
15304	0.4270	0.4259	4.1
15309	0.4267	0.4256	4.4
15321	0.4271	0.4260	4.0
15327	0.4271	0.4261	3.9
15335	0.4270	0.4261	3.9
16-rod average	0.4268	0.4259	4.1
BOL nominal	0.4300	--	--

Figure 4-7. Oxide Corrected Average Diameter Profiles of Four- and Five-Cycle Fuel Rods

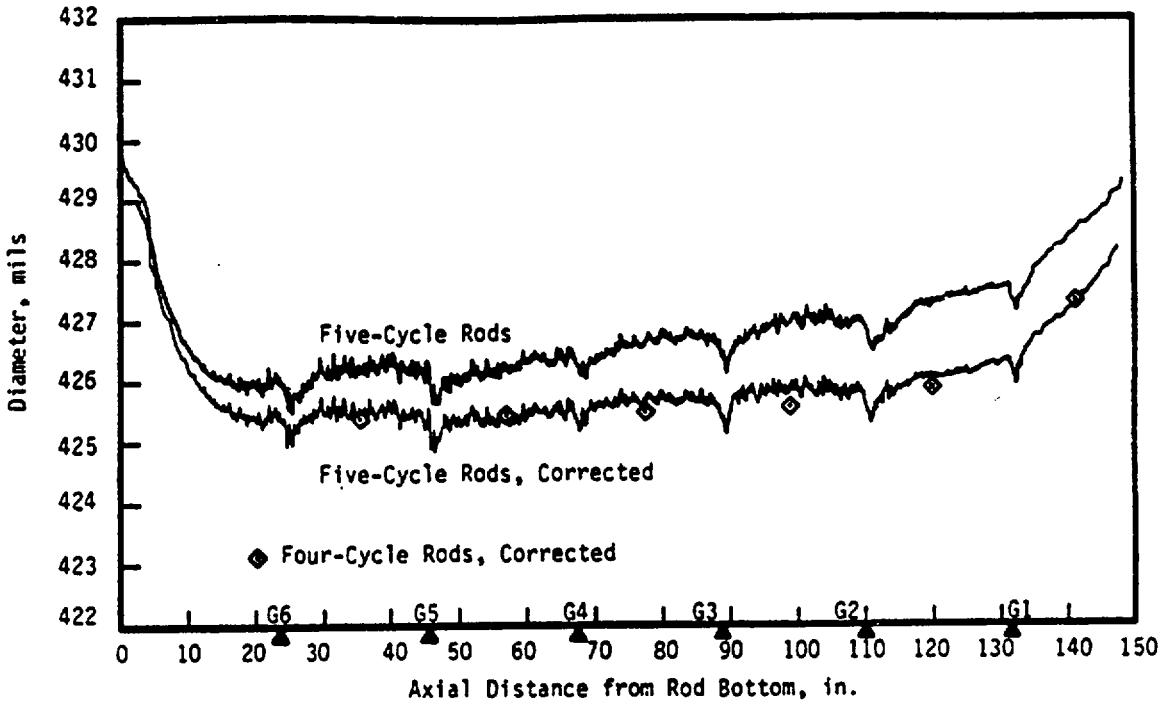

Figure 4-8. Five-Cycle Fuel Rod-Average Diameters -- 16 Rods From Assembly 1D45 (Poolside Equivalent Segments -- Not Corrected for Oxide)

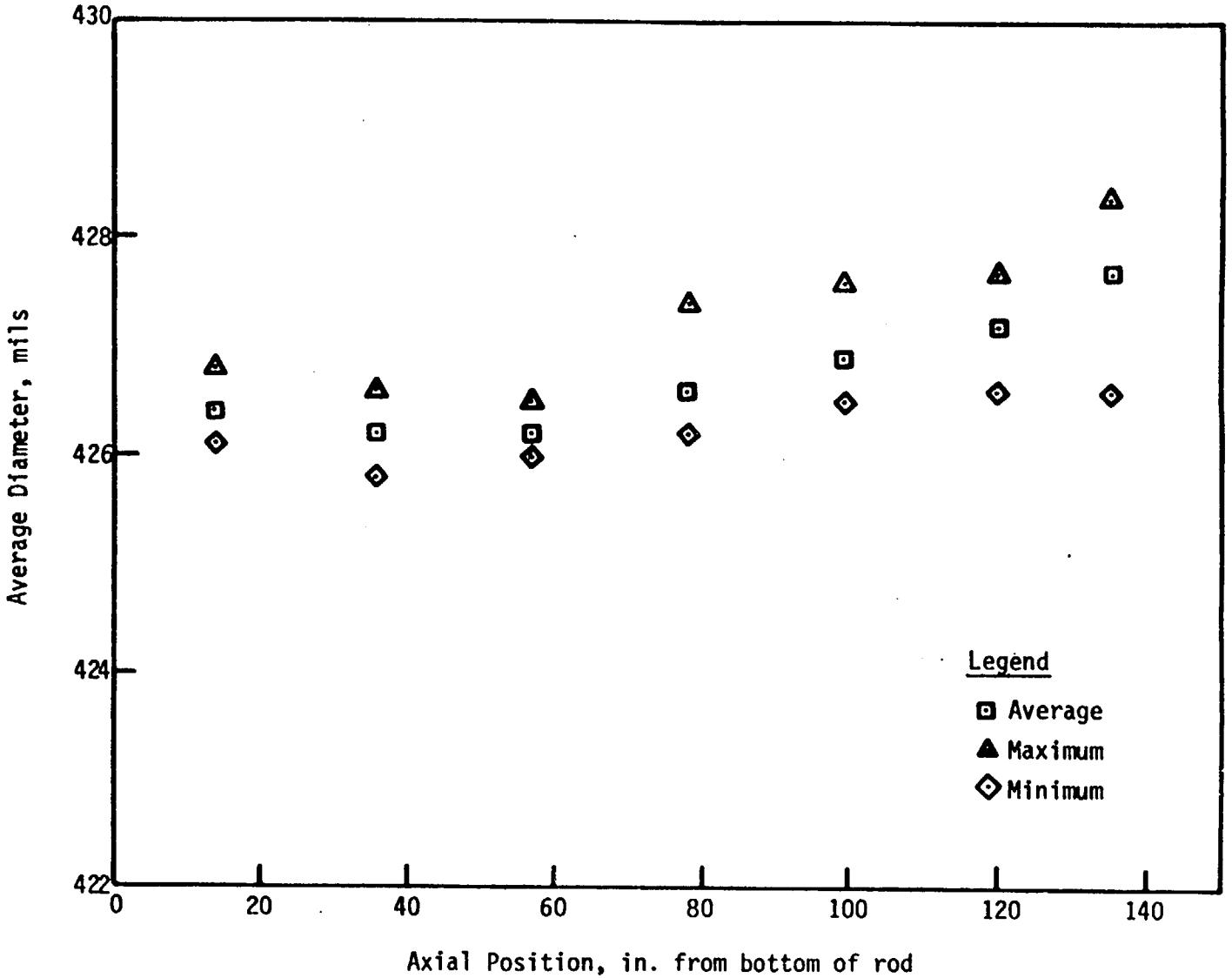

of these scans over the spotted region on rod 15304 (C7) is shown in Figure 4-9. The "near-contact" region on rods D2 and D3 (15190 and 15192) was also found to be in relief, with the maximum height observed being about 2 mils. These regions were examined by metallography during the destructive hot cell examinations and were found to be an increased thickness of oxide (see section 4.11).

4.5. Fuel Rod Gamma Scans

Gamma activity measurements were made on all 16 five-cycle rods from assembly 1D45. Full-length continuous scans of gross gamma and Cs-137 gamma activity were made to determine fuel column lengths, the size and location of fuel column gaps, and cumulative burnup profiles. Gamma energy spectra were obtained at nine axial positions along each fuel rod. Peak search software was used to determine the activity of six fission product radionuclides at each position. Measurement methods were the same as previously reported for three- and four-cycle fuel rods.[27]

4.5.1. Fuel Column Lengths and Gaps

Fuel column lengths after five cycles of irradiation ranged from 141.91 to 142.91 inches, with an average length of 142.52 inches for the 16 rods. Results for individual rods are given in Table 4-5. The average beginning-of-life (BOL) stack length for this fuel lot was 141.21 inches, indicating that the average column length increased 1.3 inches over five cycles. As shown in Table 4-6, a comparison of five-cycle data with three- and four-cycle stack lengths measured at poolside indicates that a 0.4- and a 0.9-inch increase in length occurred during the fourth and fifth cycles of operation, respectively. This increase in fuel column length in the fifth cycle corresponds favorably to the fuel rod growth increase discussed in section 4.3. No fuel column gaps >0.050 inch, the detectability limit, were observed in any of the 16 five-cycle rods.

4.5.2. Gamma Activity Axial Profiles

Gross gamma and Cs-137 activity levels from the continuous scans were tabulated at 40 axial positions per rod. Activity levels were normalized to the highest level per rod to provide relative gross and isotopic axial profiles for each rod. Examples of the normalized data from five-cycle rod

Figure 4-9. Linear Diameter Scans Over the Spotted Region on Rod 15304 (C7)

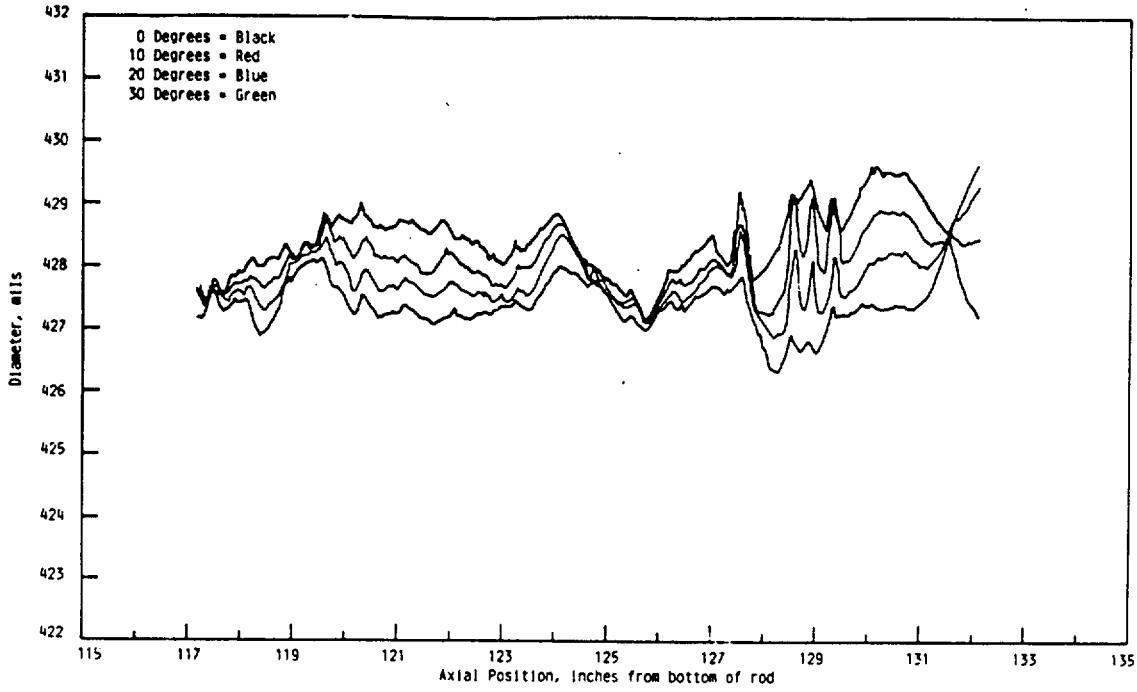

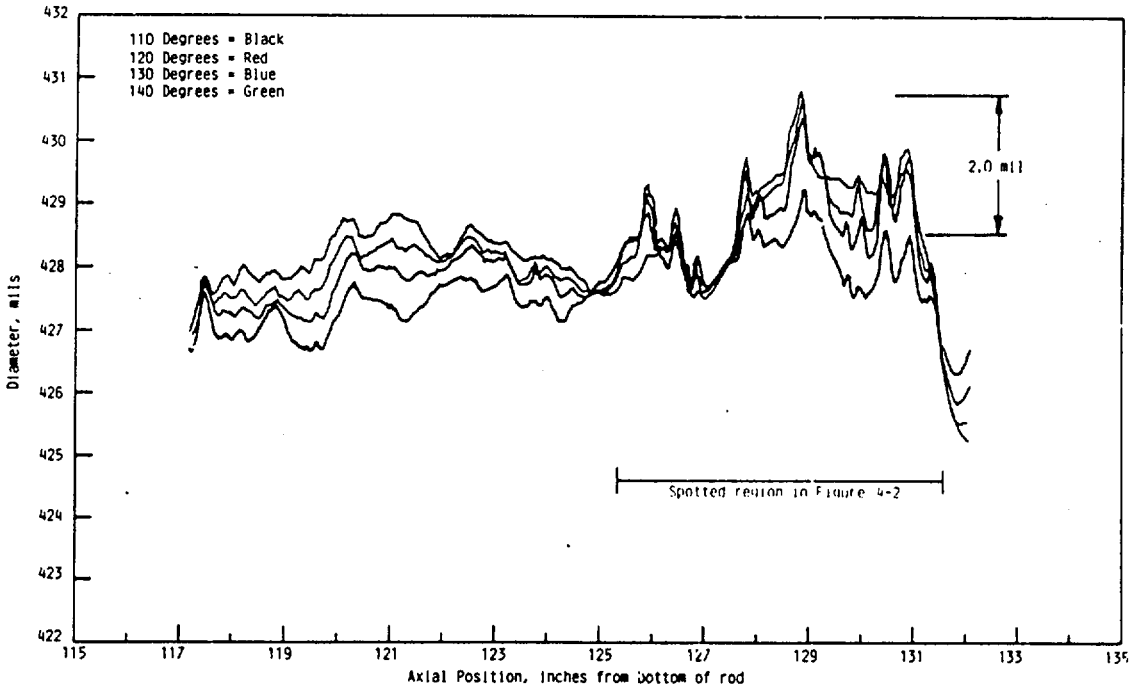

Table 4-5. Five-Cycle Fuel Column Lengths

Fuel rod No.	Stack length, in.
14955	141.96
15159	142.47
15181	142.66
15182	142.90
15183	142.36
15189	142.83
15190	142.86
15192	142.41
15194	142.71
15197	142.61
15303	142.39
15304	142.66
15309	142.91
15321	142.23
15327	142.44
15335	141.91
Average	142.52
Average BOL	141.21

Table 4-6. Fuel Column Elongation -- Fourth and Fifth Cycle

Rod location	Fuel rod	Stack length, in.			Stack length change, in.	
		5-cycle[a]	4-cycle[b]	3-cycle[b]	Cycle 5	Cycle 4
AB corner	15335	141.9	140.9	140.7	1.0	+0.3
BC corner	15181	142.7	141.9	141.6	+0.8	+0.3
CD corner	15183	142.4	141.5	--	+0.9	--
AC corner	15159	142.5	141.6	141.1	+0.9	+0.5

(a) Hot cell measurements.
(b) Poolside measurements.

Note: The average BOL stack length = 141.21 in.

15190 are shown in Figure 4-10. Since no significant axial fission product migration was observed in the continuous scans, activity profiles from the long-lived Cs-137 isotope were assumed to be proportional to cumulative fuel burnup profiles. A composite, normalized Cs-137 activity profile was derived from the profiles of the 16 rods. The integrated average of the curve was equated with the average calculated burnup for the 16 rods (49,570 MWd/mtU) to generate the cumulative burnup profile for the five-cycle rods shown in Figure 4-11. Also shown in the figure are profiles for the three- and four-cycle rods examined in the hot cell. The peak burnup from the curve for the five-cycle rods is 54,800 MWd/mtU. A comparison of the normalized Cs-137 activity profiles is shown in Figure 4-12. The highest burnup region is in the third, fourth, and fifth span regions from the top of the five-cycle rods, and the effect of the flux depression in the grid regions in less than that observed in the four-cycle profile.

4.5.3. Fission Product Activity Profiles

Gamma energy spectra were acquired at nine axial locations along the fuel column of each of the 16 five-cycle rods. Activities of six fission product isotopes (Zr-95, Ru-103, Ru-106, Cs-134, Cs-137, and Ce-144) were determined at each location. Locations along the fuel column correspond to the ends and the midspan positions. Gamma counting conditions remained constant throughout the measurements, and activity levels were decay-corrected to the same date (March 6, 1984) to allow the direct comparison of results from the 16 rods. Typical axial activity profiles for five isotopes are shown for one rod in Figure 4-13.

The Cs-134 and Cs-137 axial profiles for each rod were integrated over the fuel column length to obtain rod average activity levels. The ratio of Cs-134 to Cs-137 average activities was then determined for each rod to provide a relative burnup ranking among the 16 rods. The results are given in Table 4-7 and show that corner rods generally have the higher indicated average burnup. Face C rods had lower indicated burnups than the face B or D rods.

The average activities for four isotopes (Zr-95, Ru-106, Cs-137, and Ce-144) were determined for the 16 rods, and the results were normalized for

Figure 4-10. Normalized Continuous Activity Profiles (..od 15190)

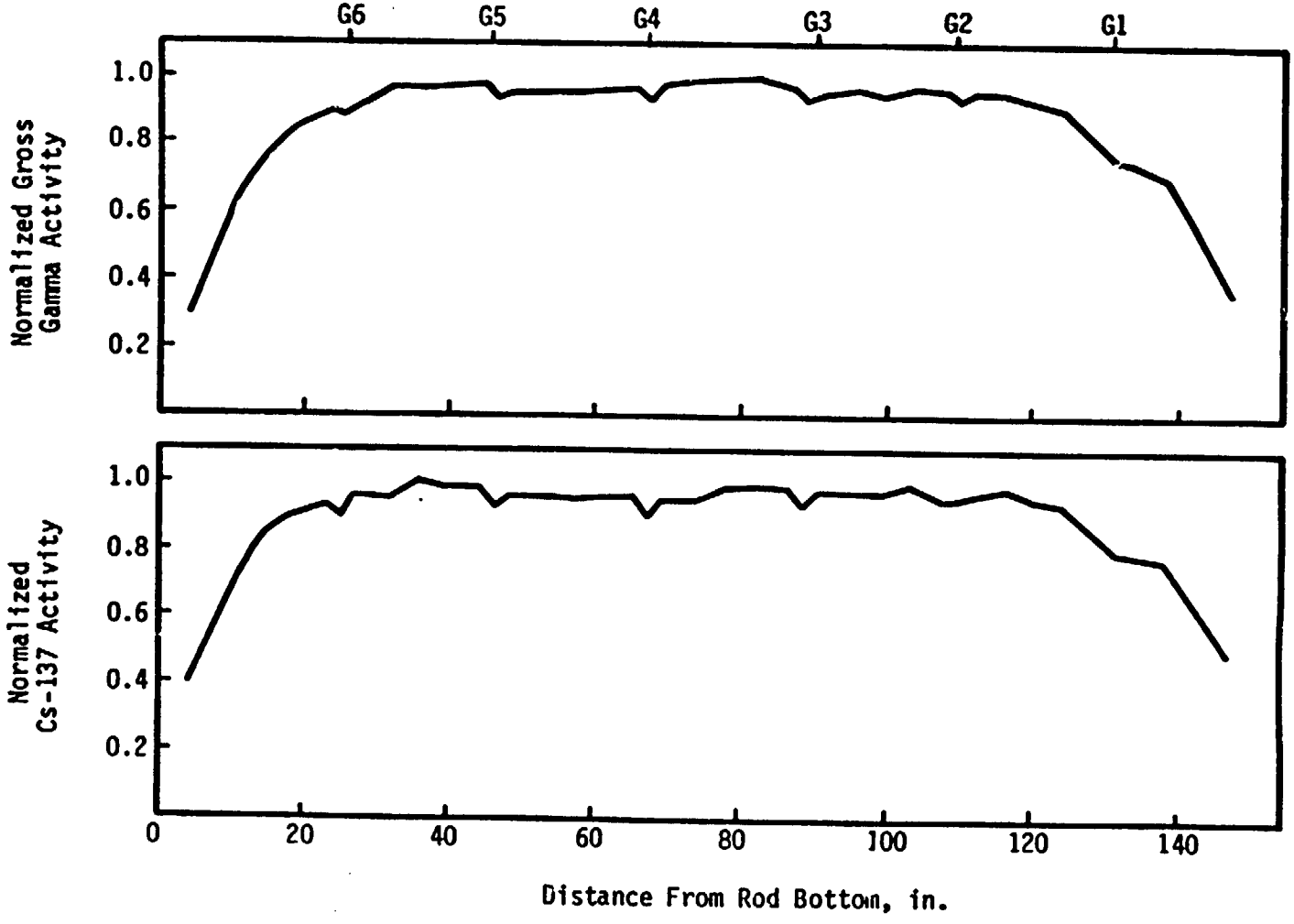

Figure 4-11. Three-, Four-, and Five-Cycle Burnup Profiles

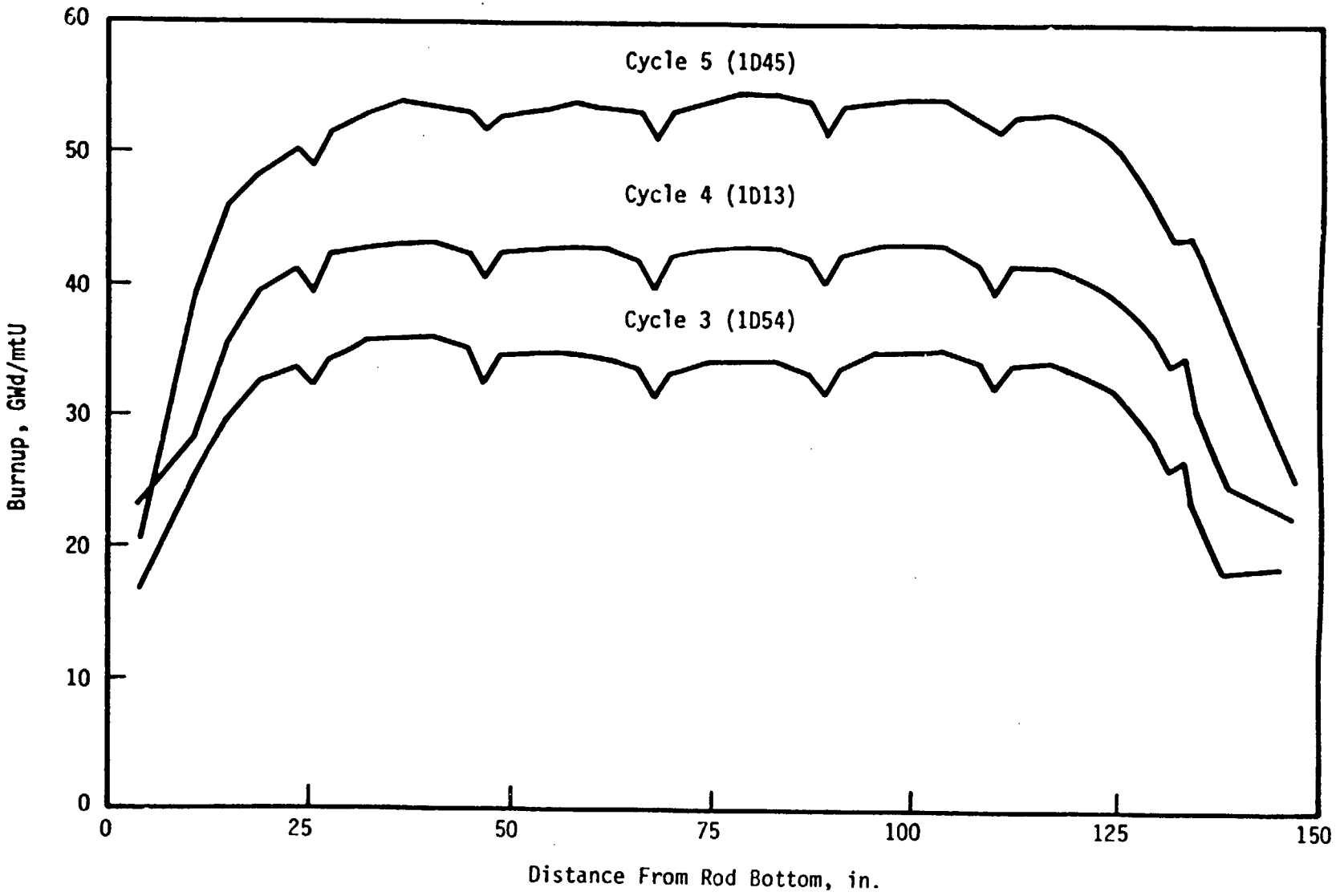

Figure 4-12. Comparison of Three-, Four-, and Five-Cycle Cs-137 Normalized Activity

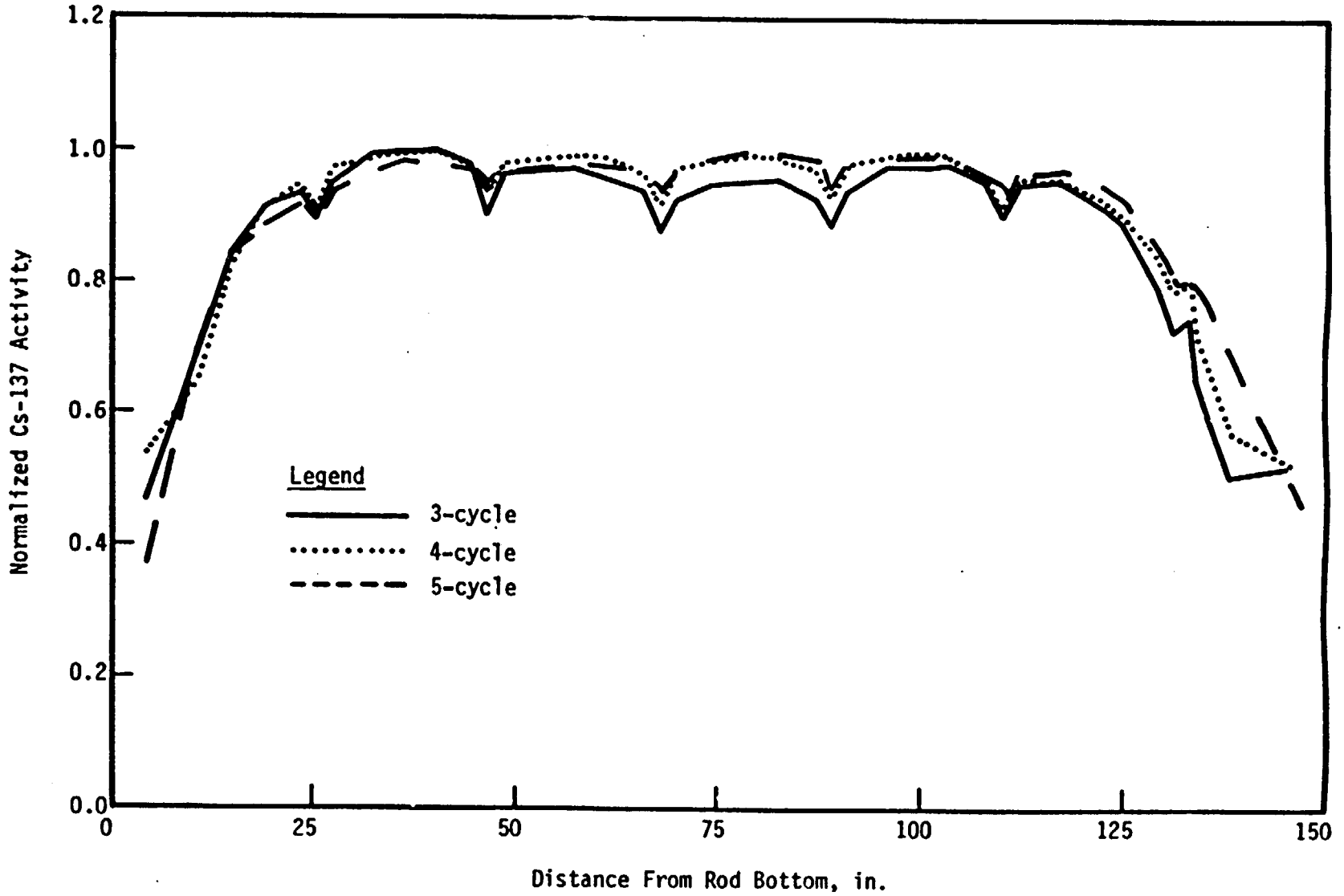

Figure 4-13. Typical Isotopic Axial Distribution After Five Cycles (Fuel Rod 15321)

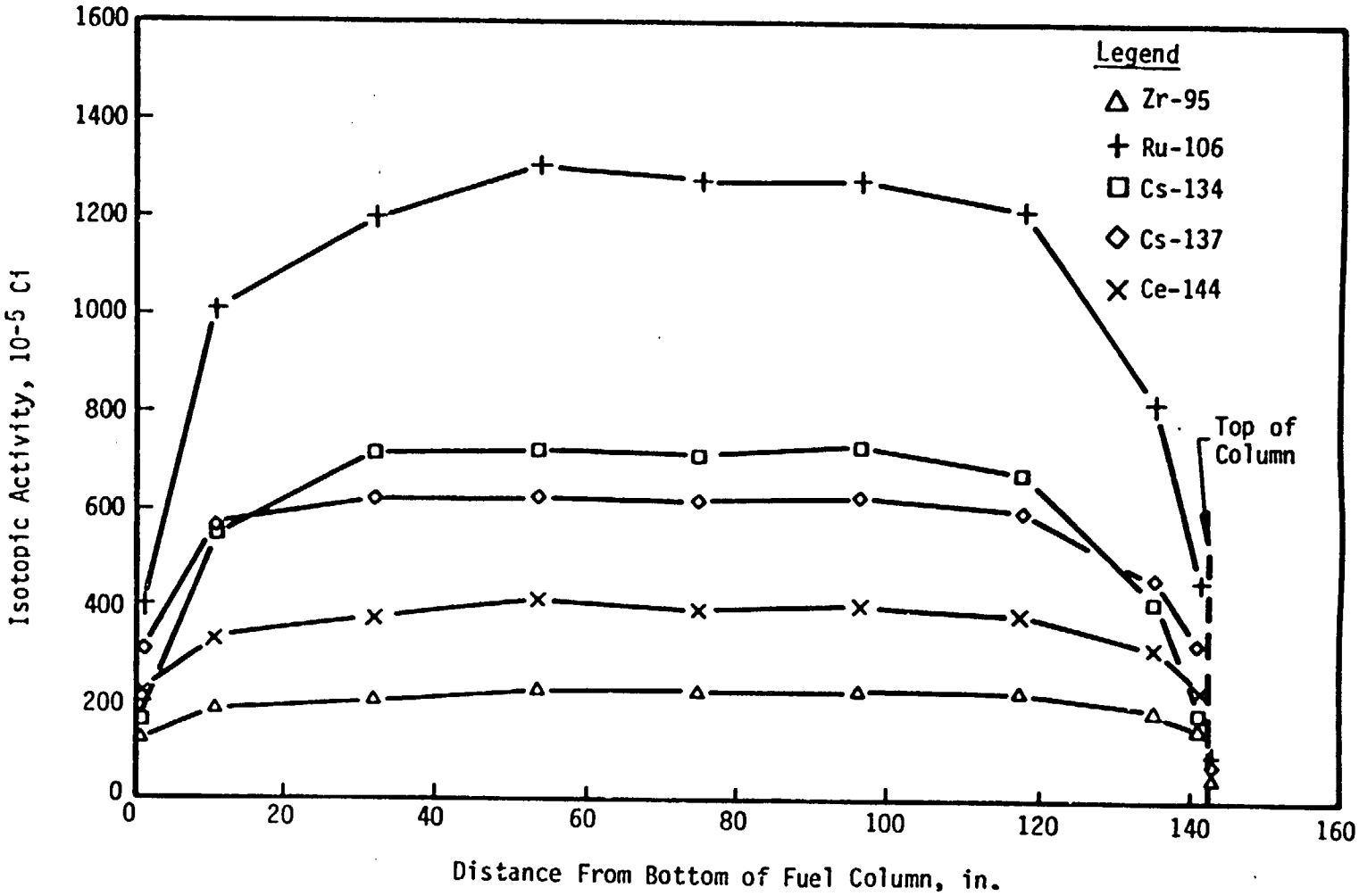

Table 4-7. Relative Burnup of Five-Cycle Fuel Rods

Fuel rod location	Rod No.	Integrated average activity, 10^{-5} Ci[a] Cs-137	Cs-134/Cs-137
C6	15303	568.5	1.06
C8	14955	627.9	1.06
C5	15309	596.6	1.07
C3	15327	598.9	1.07
C7	15304	553.7	1.08
B13	15197	580.6	1.08
C4	15321	586.3	1.09
D3	15192	582.6	1.10
C2	15189	614.2	1.11
AB	15335	617.0	1.11
CD	15183	599.7	1.12
B14	15182	626.2	1.13
B12	15194	635.1	1.13
D2	15190	595.4	1.15
BC	15181	632.2	1.16
AD	15159	624.8	1.17

[a]Decay-corrected to March 6, 1984.

comparison with the axial profiles. Results are shown in Figure 4-14. The long-lived Cs-137 axial profile represents the cumulative burnup profile, and the shape agrees well with the continuous gamma scans (Figure 4-12). The Ru-106 and Ce-144 profiles reflect the shape during the fifth cycle, and the Zr-95 profile reflects the shape during the latter part of the fifth cycle.

4.6. Eddy-Current Oxide Thickness

The nondestructive eddy-current technique[8] was used to measure oxide thickness on the 16 fuel rods. Axial line scans of the surface oxide layer were made at four azimuthal orientations (0, 90, 180, and 270 degrees) on each of the 16 rods. Oxide thickness data were recorded with the hot cell data acquisition system at 0.05-inch intervals during each scan. Areas that showed higher-than-average oxidation and unusual surface features were scanned in greater detail at 10-degree azimuthal intervals. The data were analyzed by dividing the continuous scans into segments that correspond to the distance between grids along the fuel rods as measured at poolside. A statistical analysis was performed on the oxide thickness data from within these poolside-equivalent spans; average ($\bar{x}$) and maximum ($\bar{x}+2\sigma$) oxide thicknesses were determined for each rod grid span. This methodology facilitates the direct comparison of oxide data acquired in the hot cell with that acquired at poolside during previous campaigns. Additionally, the thickest oxide measured at any point on the rod within each grid span (peak local oxide thickness) was compared with the value of the respective statistical maximum ($\bar{x}+2\sigma$) to assess the validity of this methodology. Scans of the unusual surface features were not included in the analysis, but were analyzed separately.

Several typical oxide thickness profiles are shown in Figure 4-15. The profiles show oxide thickness increasing from the bottom to the top of the rod, with reductions of 20 to 30% occurring in the areas of the intermediate spacer grids. Span-average oxide thicknesses ($\bar{x}$) for these rods are listed in Table 4-8, which also includes hot cell oxide data from three- and four-cycle rods from sister assemblies 1D54 and 1D13, respectively.[9] The average and range of these values are shown plotted versus axial location in Figure 4-16.

Figure 4-14. Normalized Isotopic Axial Distribution After Five Cycles (Average of 16 Rods)

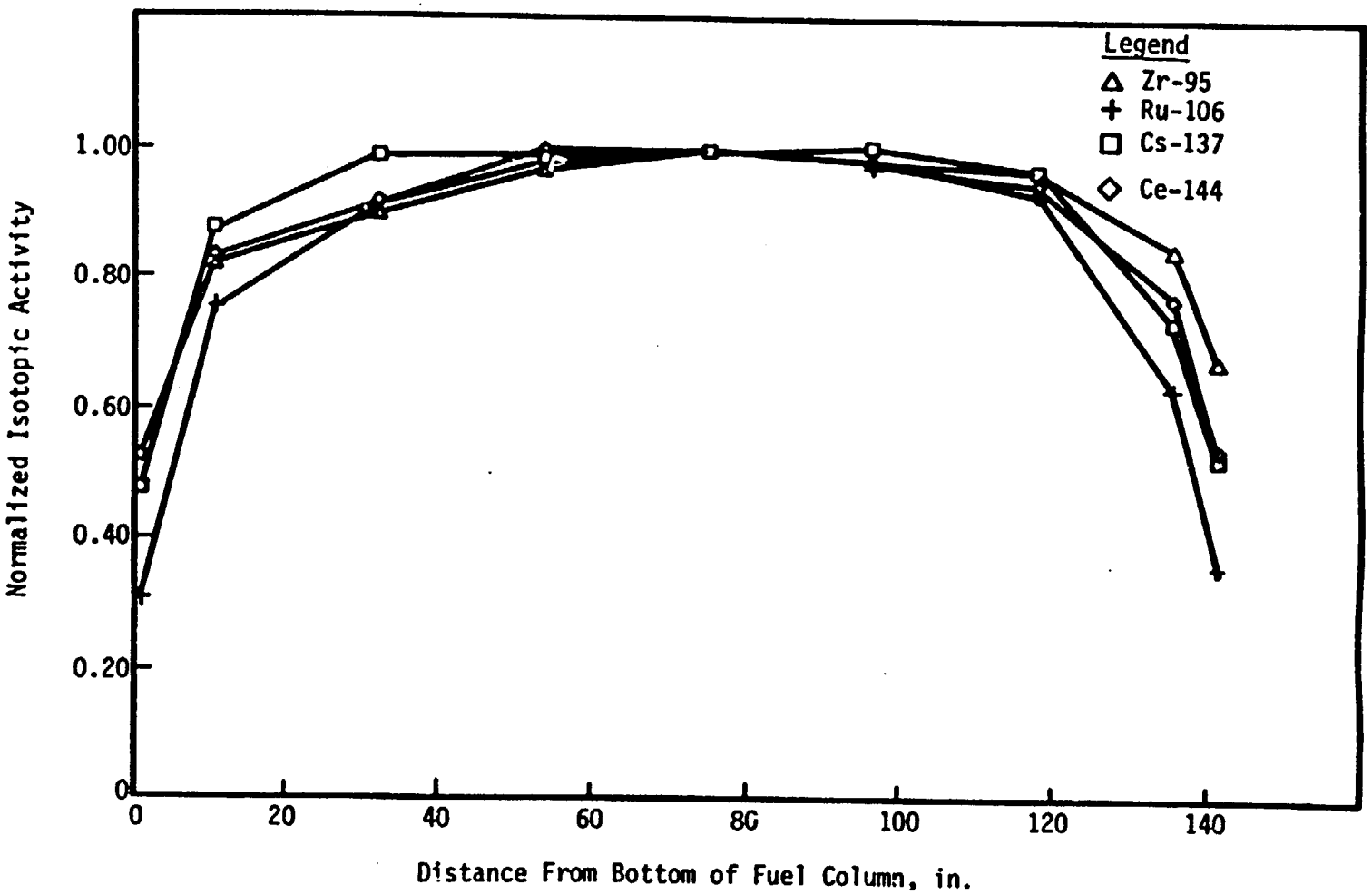

Figure 4-15. Typical Oxide Profiles of Rod 14955 at Four Orientations

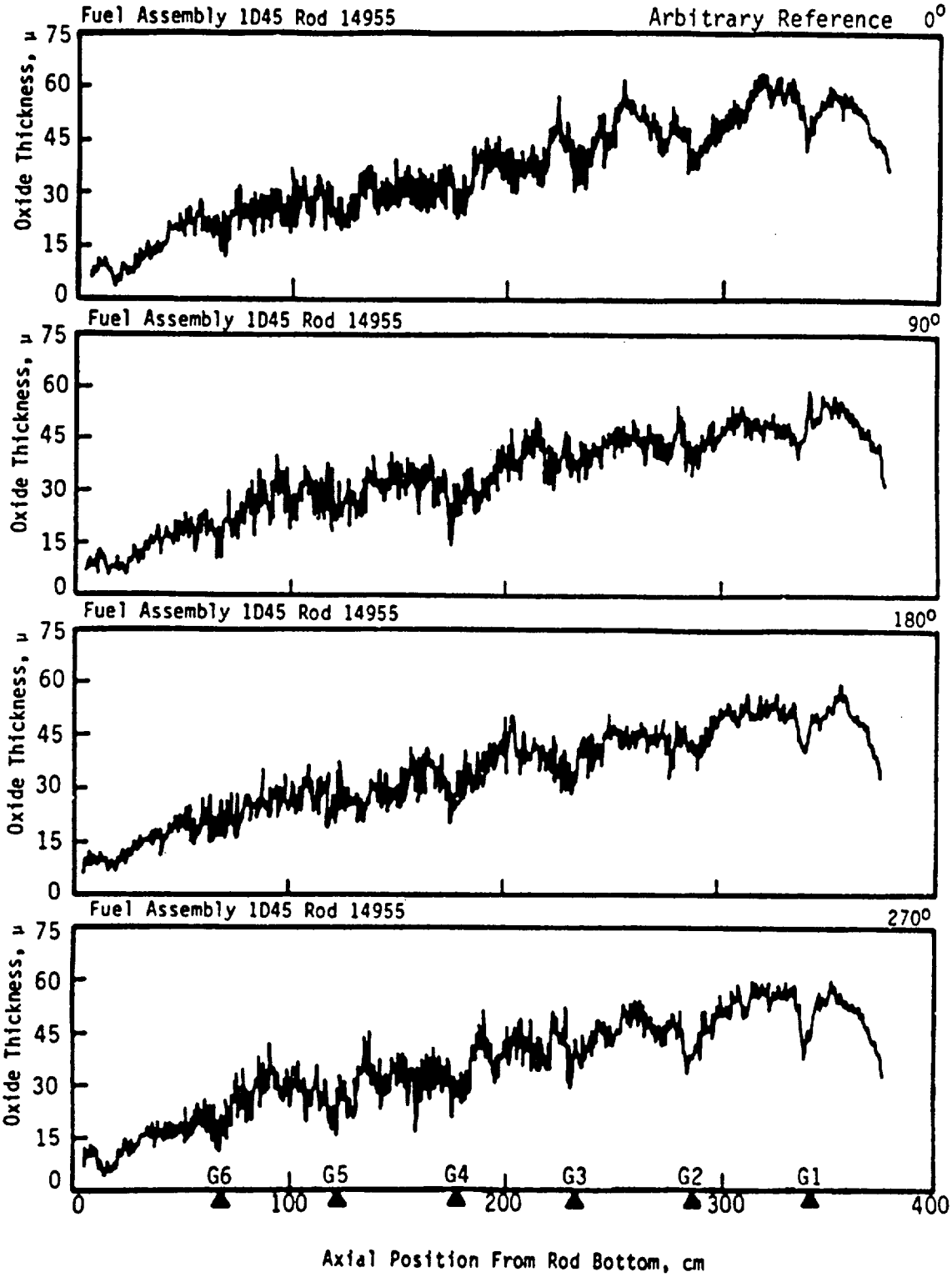

Table 4-8. Span-Average Oxide Thickness

Fuel Assembly	Location[a] in FA	Fuel rod No.	Span-average oxide thickness ($\bar{x}$), μ (Top) Span 1	2	3	4	5	6	(Bottom) 7
1D45[b] (5 cycles)	C8	14955	49.7	51.3	44.9	38.1	30.8	25.7	16.1
	AD	15159	38.2	44.2	39.9	34.6	29.1	25.4	17.2
	BC	15181	34.6	38.4	36.4	32.3	28.2	25.1	16.2
	B14	15182	35.8	40.7	38.5	34.8	29.4	25.1	16.5
	CD	15183	38.4	41.0	36.8	31.3	26.4	23.0	15.6
	C2	15189	37.8	41.2	39.0	35.6	29.8	24.6	15.4
	D2	15190	39.4	42.6	37.2	32.4	27.0	23.7	15.4
	D3	15192	43.6	47.8	42.0	36.0	30.2	25.7	17.8
	B12	15194	42.0	48.0	44.0	38.1	31.5	27.0	16.6
	B13	15197	41.1	46.2	44.1	36.9	31.0	26.0	17.2
	C6	15303	46.6	49.9	46.2	38.8	30.8	26.6	17.6
	C7	15304	45.8	47.5	43.6	37.6	30.2	25.9	16.5
	C5	15309	50.0	55.6	47.4	40.0	31.8	27.0	17.2
	C4	15321	47.9	54.0	46.8	39.0	33.0	27.4	15.8
	C3	15327	43.0	47.1	41.9	37.5	30.2	28.0	15.4
	AB	15335	33.2	37.1	35.8	29.8	26.9	22.4	16.3
	Max		50.0	55.6	47.4	40.0	33.0	28.0	17.8
	Mean		41.7	45.8	41.5	35.8	29.8	25.5	16.4
	Min		33.2	37.1	35.8	29.8	26.4	22.4	15.4
1D13[c] (4 cycles)	Max		27.2	28.8	26.5	23.6	17.3	14.0	10.3
	Mean		23.7	25.6	23.3	19.0	14.0	12.1	7.8
	Min		19.3	21.8	21.3	14.2	11.2	8.4	6.0
1D54[c] (3 cycles)	Max		22.4	23.9	19.6	16.8	11.1	8.1	5.1
	Mean		20.5	21.9	18.4	14.8	9.8	6.3	3.3
	Min		18.8	18.9	16.0	13.0	6.5	3.1	1.3

(a) See Figure 4-1.

(b) Average of four azimuthal orientations per rod.

(c) Maximum values of $\bar{x}$ among the four azimuthal orientations on the two rods.

Figure 4-16. Span-Average Oxide Thickness (Average and Range) Vs Axial Position -- Hot Cell Eddy-Current Results

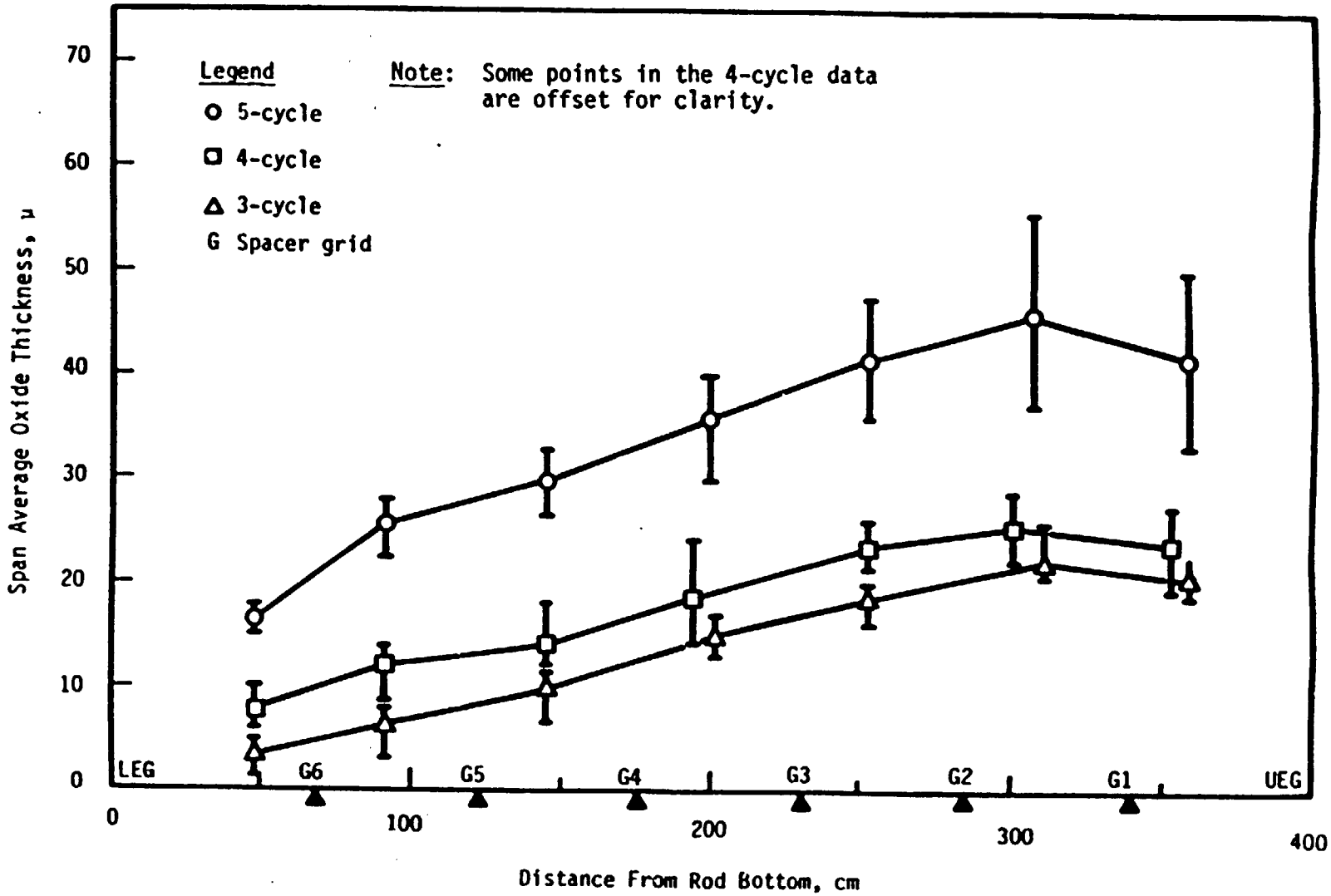

In all cases, the maximum span-average ($\bar{x}_{max}$) oxide layer occurred in span 2 (between intermediate grids 1 and 2). The maximum span-average oxide thickness on the five-cycle rods ranged from 37.1 (corner rod AB) to 55.6μ (rod C5), with an average of 45.8μ. This value compares to a maximum span-average thickness of 21.9μ on the three-cycle rods and 25.6μ on the four-cycle rods. The maximum span-average oxide thickness (average and range) is shown plotted versus both EFPD and burnup in Figures 4-17 and 4-18, respectively. Both figures show a significant increase in the oxidation rate during the fifth cycle of irradiation.

Maximum ($\bar{x}+2\sigma$) and peak local oxide thickness values were determined for each span of the 16 rods. The maximum values obtained at any of the four azimuthal orientations on each rod are compared in Table 4-9. Also included in this table are the maximum ($\bar{x}+2\sigma$) values determined for the three- and four-cycle fuel rods in previous hot cell examinations. For the five-cycle fuel rods, local peak oxide thicknesses ranged from 46.3 to 66.4μ, and averaged 57.1μ; the rod maxima values ($\bar{x}+2\sigma$) ranged from 46.1 to 70.1μ, and averaged 57.2μ. Thus, the local peak oxide thickness is approximated well by the statistical maximum ($\bar{x}+2\sigma$). The average of these maxima for the three-, four-, and five-cycle fuel rods are 27.2, 31.0, and 57.2μ, respectively. The mean and range of these maxima, as given in Table 4-7 for span 2, are plotted versus burnup in Figure 4-19. Also shown in this figure are the previously reported oxide data[23] and the published Kraftwerk Union (KWU) bounds.[32] As with the maximum span-average data, the oxidation rate shows a significant increase in the fifth cycle of irradiation.

The final step in this analysis is the evaluation of oxide thickness on the unusual surface features; i.e., the series of spots on some rods and the bowed-to-contact region.[23] Rods C3, C4, C5, C6, C7, C8, C15, and B12 showed unusual spots in span 2. Rods D2 and D3 were bowed to contact in span 5. Seven of these rods were examined and showed sharp deviations in the oxide layer thickness over these features. Typical oxide thickness traces of the unusual features on rods C5 and D3 are shown in Figure 4-20. The unusual spots on rod C5 show sharp peaks of over 100μ in the oxide layer. The bowed-to-contact region of rod D3 shows an area 10 to 13 cm in length with a

Figure 4-17. Maximum Span-Average Oxide Thickness (Average and Range) Vs Exposure Hot Cell Data on Three-, Four-, and Five-Cycle Rods

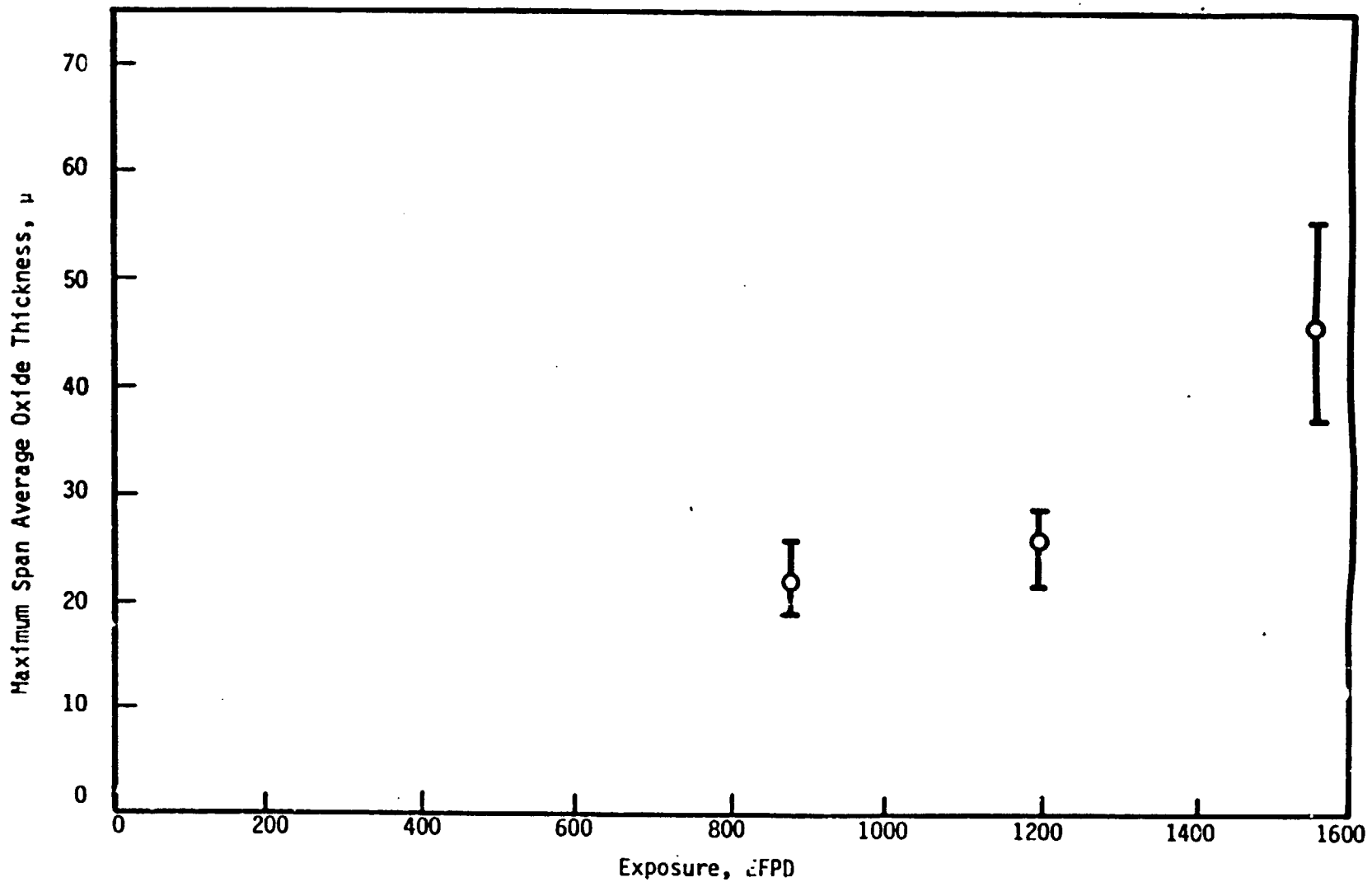

Figure 4-18. Maximum Span-Average Oxide Thickness (Average and Range) Vs Burnup Hot Cell Data on Three-, Four-, and Five-Cycle Rods

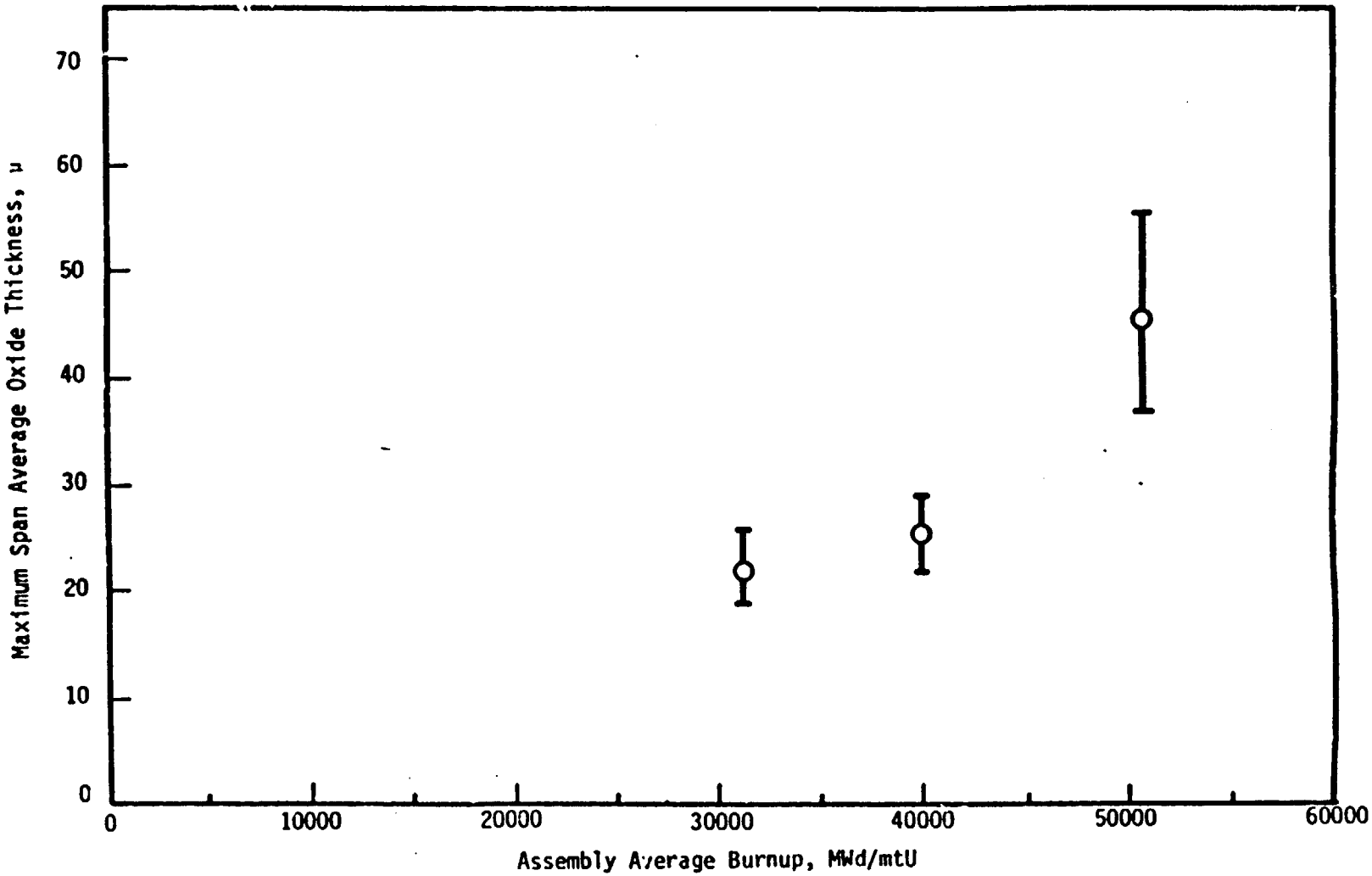

Figure 4-19. Oxide Thickness Maxima (Average and Range) Vs Assembly-Average Burnup

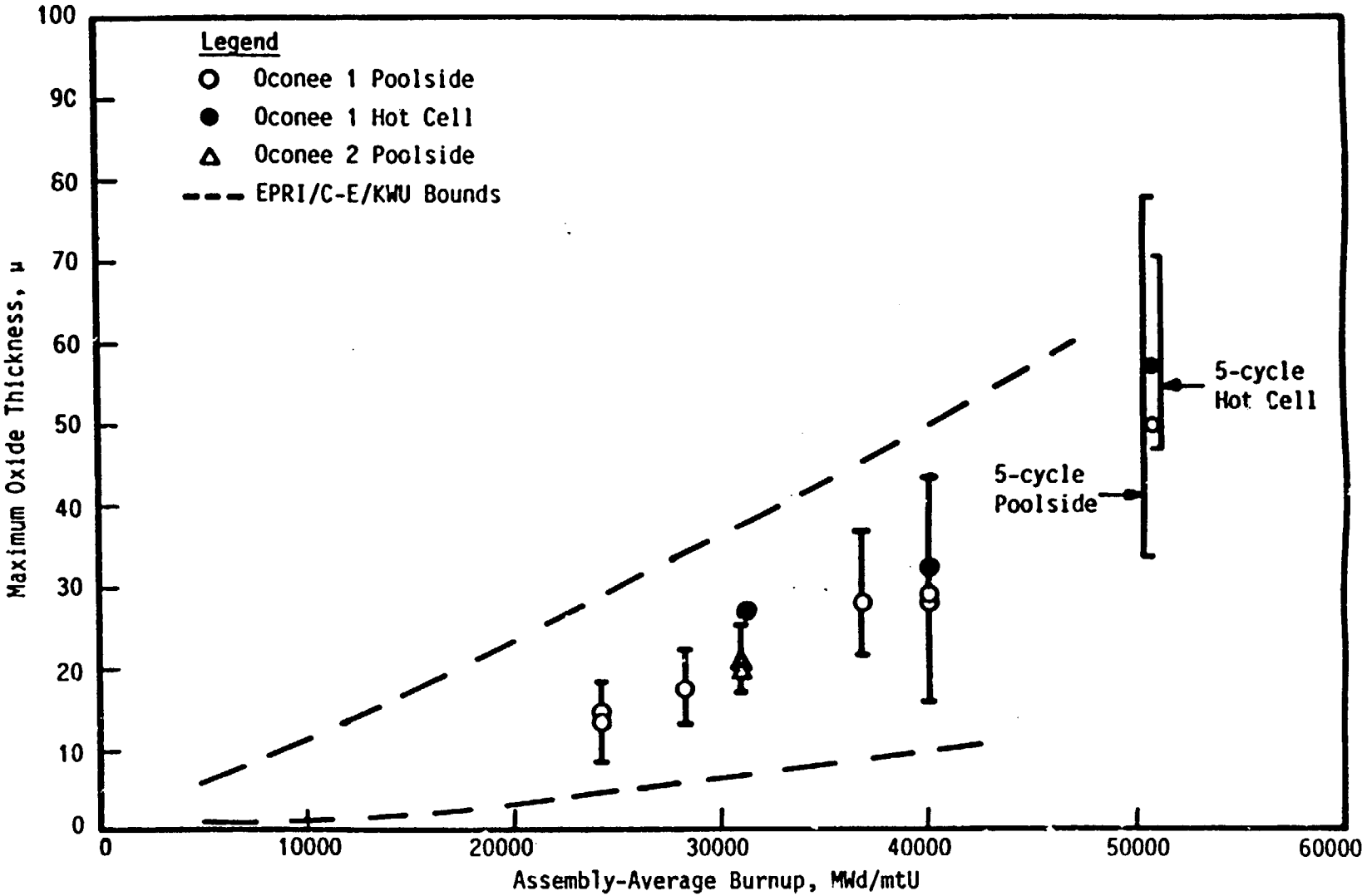

Table 4-9. Oxide Thickness Span Maxima

Fuel Assembly	Location[a] in FA	Fuel rod No.	Oxide Thickness Maxima ($\bar{x}+2\sigma$), μ[b] (Top) Span 1	2	3	4	5	6	(Bottom) 7	Oxide Thickness Maxima (Local Peak), μ[b] (Top) Span 1	2	3	4	5	6	(Bottom) 7
1045 (5 cycles)	C8	14955	63.1	64.5	57.6	49.6	60.6	37.4	27.1	59.3	63.0	60.6	56.4	44.5	41.5	27.8
	A0	15159	46.7	51.7	48.0	47.2	39.3	40.3	29.9	46.9	53.0	51.2	51.8	43.9	44.0	29.8
	B0	15181	46.1	49.1	47.0	45.8	38.3	35.4	32.0	46.2	50.7	49.6	49.8	41.5	40.1	30.8
	B14	15182	46.7	51.0	52.1	50.2	38.0	36.2	27.3	45.5	51.5	53.4	52.4	40.5	41.1	31.4
	C0	15183	48.6	53.1	48.3	47.2	38.6	34.1	25.8	47.3	59.3	50.1	52.7	44.7	37.6	27.2
	C2	15189	49.4	53.4	49.7	46.6	40.4	35.6	28.0	48.0	58.0	51.1	51.9	46.8	42.9	30.4
	D2	15190	48.7	52.0	52.8	44.8	38.6	38.4	24.6	49.2	53.0	54.4	50.4	47.2	40.4	25.8
	D3	15192	55.8	55.7	53.2	47.1	41.3	38.6	28.7	53.9	61.0	53.9	51.6	48.1	41.9	30.1
	B12	15194	55.3	60.3	57.7	49.5	42.4	38.6	29.3	52.7	66.4	60.7	49.3	46.9	44.5	30.3
	B13	15197	51.9	56.3	61.0	49.6	41.6	36.7	28.9	50.1	59.2	62.7	50.9	52.2	38.8	34.6
	C6	15303	60.4	65.7	58.2	46.9	39.2	37.1	29.2	59.2	59.3	58.8	47.8	43.1	43.7	31.7
	C7	15304	56.0	61.5	51.3	49.0	39.1	36.7	27.8	52.1	53.8	54.6	51.4	41.6	37.3	31.7
	C5	15309	64.4	64.5	59.6	49.7	40.0	36.9	27.3	59.6	64.8	59.4	52.1	49.1	41.9	29.5
	C4	15321	61.5	70.1	54.4	51.2	49.1	39.0	26.4	56.4	61.7	54.3	53.4	53.0	43.7	29.7
	C3	15327	55.0	62.5	49.7	48.3	39.9	36.3	27.9	53.0	54.5	51.8	52.0	45.2	36.5	26.9
	A8	15335	44.7	43.4	46.1	38.3	39.1	35.3	27.4	42.7	45.9	46.3	39.7	45.4	38.7	30.4
	Max		64.4	70.1	61.0	51.2	49.1	40.3	32.0	59.6	66.4	62.7	56.4	53.9	44.5	34.6
	Mean		53.4	57.2	52.9	47.6	40.3	37.0	28.0	51.4	57.1	54.6	50.8	45 9	40.9	29.6
	Min		44.7	43.4	46.1	38.3	38.0	34.1	24.6	42.7	45.9	46.3	39.7	40.5	36.5	25.8
1013 (4 cycles)	Max		30.3	32.2	31.8	30.5	22.4	19.5	12.4							
	Mean		30.2	31.0	29.7	26.8	21.0	18.9	12.1							
	Min		30.1	29.9	27.7	23.0	19.6	18.3	12.0							
1054 (3 cycles)	Max		27.6	27.8	25.5	21.6	16.8	12.5	9.6							
	Mean		25.7	27.2	24.8	21.4	15.8	12.0	8.9							
	Min		23.8	26.7	24.1	21.2	14.8	11.5	8.2							

[a] See Figure 4-1.

[b] Maximum among the four azimuthal orientations on each rod.

Figure 4-20. Typical Oxide Thickness Traces of Unusual Features on Rods C5 and D3

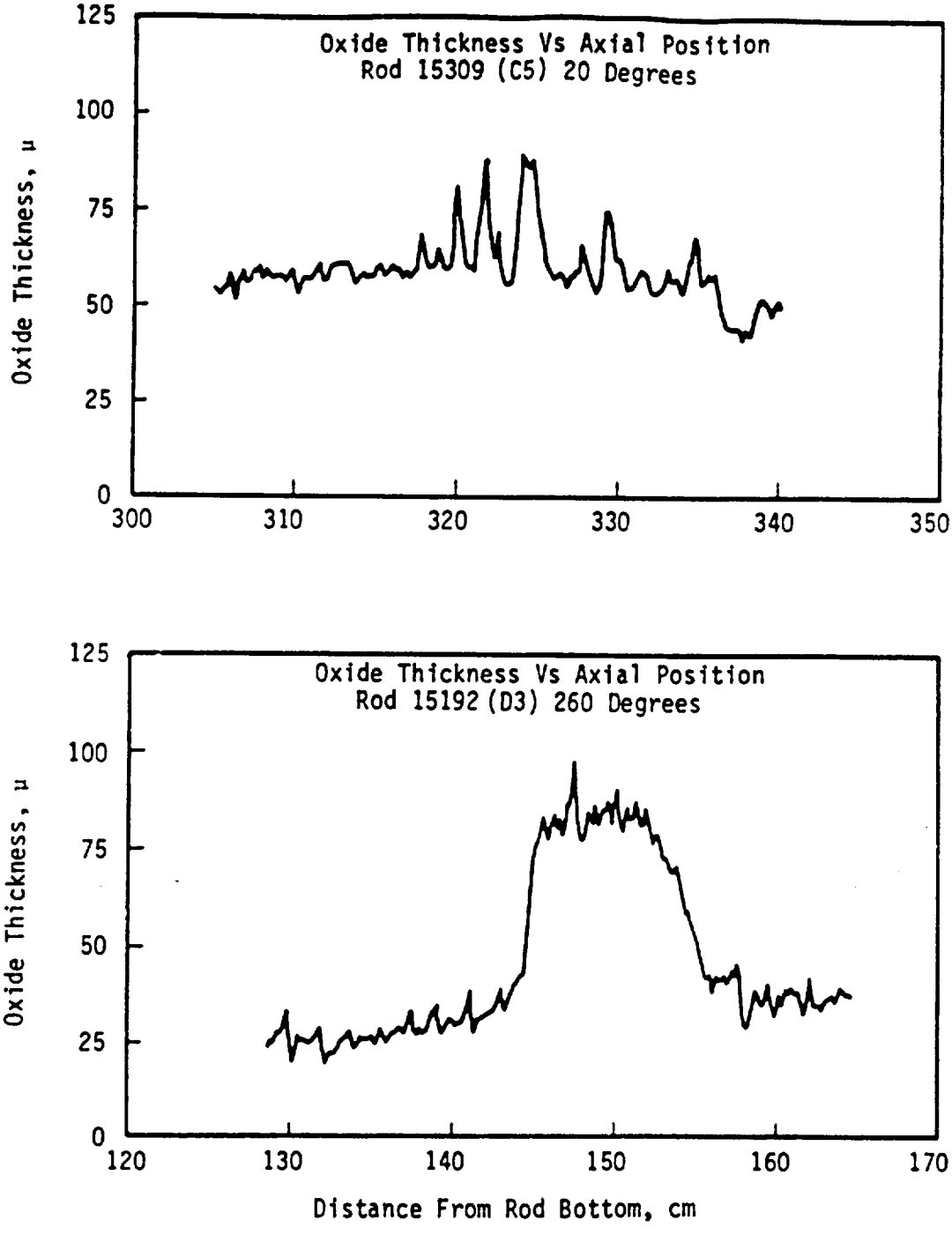

peak oxide thickness of about 120μ. The regions adjacent to these areas show oxide thicknesses typical of the other rods in the assembly. The destructive examination of these regions is discussed in section 4.11.

4.7. Eddy-Current Inspection

An eddy-current inspection was performed on all 16 fuel rods. A multi-frequency encircling differential coil was used to inspect the cladding for anomalies or defects. Axial scans of the rods were made at frequencies of 230, 500, and 930 kHz in a differential mode, and at 510 kHz in an absolute mode. Areas of the rods that showed interesting features were reexamined with a mix of 550 and 930 kHz frequencies to suppress the response to ridging in the cladding. Calibration of the eddy-current system was achieved by scanning a defect standard that contains a variety of simulated inside and outside diameter defects.

This examination showed the cladding to be in good condition. No through-wall defects were detected; however, several small indications were noted. In all, six small indications were detected on the 16 rods. Close examination of the Lissajous patterns showed that the indications were quite similar in phase angle and amplitude. Their phase angle suggests that the anomalies are located on the inside surface of the cladding. In comparisons with the calibration standards, the indications did not appear to be caused by loss-of-metal defects. These indications are expected to be caused by a localized variation in cladding conductivity, which is possibly the result of intimate pellet-cladding contact.

During the destructive examination, the areas in which several of these indications are located were metallographically characterized through a sequential grind-and-polish technique to investigate the indication.

4.8. Rod Plenum Spectroscopy

Prior to fuel rod puncturing and gas analysis, the upper plenum of each rod was examined for Kr-85 activity by gamma spectroscopy to obtain a relative ranking of fission gas release. Results of this preliminary "screening" technique are presented in Table 4-10. The intrinsic Ge detector and counting conditions for these rods were different from those previously used for three- and four-cycle rods from assemblies 1D54 and 1D13, respectively.

Table 4-10. Five-Cycle Kr-85 Plenum Count Rates

Group	Relative Kr-85 content	Fuel Rod	Count Rate, cps
1A	12	15335	0.36[a,b]
1	4-6	15197	0.12
		15159	0.13
		14955	0.12[b]
		15182	0.16[b]
		15194	0.18
2	2-3	15183	0.07
		15309	0.07
		15181	0.09[b]
		15327	0.09
		15189	0.10
3	ND[c] - 1	15192	<0.02
		15303	<0.02
		15304	<0.03
		15190	0.02
		15321	0.03

[a] The interference peaks (Rh-106 at 511 and 512 keV) were abnormally low in this rod.

[b] Revised values from those in Reference 23.

[c] ND denotes "none detected."

Therefore, no direct comparison of Kr-85 count rates with previous campaigns is appropriate. Furthermore, the positron annihilation and Rh-106 peaks (511 and 512 keV, respectively), which neighbor the Kr-85 peak (514 keV), were more intense in the current rods due to a significantly shorter cooldown period since discharge. Therefore, the counting statistics exhibit a greater uncertainty in this campaign, and the data provide only an approximate relative indication of gas release in the rods. Background-corrected count rates for Kr-85 ranged from a nondetectable level to 0.36 cps for the 16 rods. The correlation of Kr-85 count rates with measured fission gas is given in section 4.9.3.

4.9. Fission Gas Analysis

4.9.1. Rod Puncturing

All 16 five-cycle rods were punctured mechanically to determine cold internal pressure, free void volume, and released fission gas content. Measurements were made with the same equipment and techniques used for three- and four-cycle rods.[27] The results confirmed that all 16 rods were sound and fully pressurized. Volume measurements performed by backfilling the fuel rod with helium were difficult due to the extensive pellet-cladding contact and slow gas communication within the rods.

4.9.2. Rod Pressure and Volume

Internal pressure of the 16 five-cycle rods ranged from 558 to 654 psia, with an average value of 602 psia at room temperature. Free void volumes ranged from 26.2 to 28.2 cc, with an average of 27.2 cc. Results for individual rods are given in Table 4-11. Results from three-, four-, and five-cycle rods are given in Table 4-12. On the average, rod pressure increased 18% and free void volume decreased 17% during the two cycles of extended burnup operation. Thus, the increase in average pressure from the EOCs 3 through 5 can be accounted for almost entirely by the decrease in average volume (Table 4-12), with the additional amount of fission gas playing only a minimal role in affecting rod pressures (Table 4-13). The highest pressure measured (654 psia) results in a net compressive hoop stress on the cladding under operating conditions.

Table 4-11. Five-Cycle Fuel Rod Pressure and Void Volume

Fuel rod location	Rod No.	Pressure, psia	Free void volume, cc
AB	15335	640	28.0
B12	15194	632	27.0
B13	15197	619	27.7
B14	15182	634	26.4
BC	15181	654	26.2
C2	15189	610	27.0
C3	15327	576	26.9
C4	15321	558	27.5
C5	15309	575	26.9
C6	15303	586	27.1
C7	15304	573	27.2
C8	14955	572	28.2
CD	15183	597	27.8
D2	15190	586	27.7
D3	15192	608	27.2
AD	15159	611	27.0
	Average	602	27.2
	BOL	480	35

Table 4-12. Extended Burnup Fuel Rod Pressure and Void Volume

Cycle	Pressure, psia		Free void volume, cc	
	Average	Range	Average	Range
3	509	495-522	32.8	32.3-33.2
4	542	511-577	29.4	27.8-30.4
5	602	558-654	27.2	26.2-28.2

4.9.3. Fission Gas Release

The plenum fission gas content and isotopic abundance in each rod were determined with a quadrupole mass spectrometer. Fractional fission gas release was determined as the ratio of moles of plenum fission gas (measured) to the moles of fission gas generated (calculated) at a burnup of 49,000 MWd/mtU. Gas release in the five-cycle rods ranged from 0.7 to 3.8%, with an average of 1.6%. Plenum gas content and fission gas release results for the 16 rods are given in Table 4-13. The Kr-85 gamma count rate for each rod plenum is also included in the table.

The correlation between fission gas release and Kr-85 plenum count rate is shown in Figure 4-21. Even though the rod with the highest gas release also had the highest Kr-85 plenum count rate, considerable scatter in the rest of the data exists. Although a positive correlation exists for higher count rates, there is much uncertainty in fission gas release for count rates below 0.1 cps.

Plenum fission gas content and fission gas release from three-, four-, and five-cycle rods are summarized in Table 4-14 and shown as a function of burnup in Figures 4-22 and 4-23. The plenum fission gas content shows the expected increasing trend with burnup; however, the increase is considerably lower over the fifth cycle than over the fourth cycle. Fractional fission gas release after five cycles is essentially the same as that after four cycles, meaning that the gas release rate is nearly constant. Thus, the data from these rods do not support the exponential burnup-dependent enchancement terms suggested by the Nuclear Regulatory Commission (NRC) for use in high-burnup release models in the absence of more applicable data.

Fission gas isotopes of Kr and Xe and their isotopic abundances in the five-cycle fuel rods are given in Table 4-15. Average results from the four-cycle analysis are also given. The four- and five-cycle results are in good agreement, indicating that the isotopic composition of the released fission gas is different from the fission yield isotopic fractions. As expected, the Xe/Kr ratios given in Table 4-13 are higher than those calculated from the fission yield, indicating that the Xe isotope precursors have a higher migration rate from the fuel than the Kr isotopes. This is

Table 4-13. Five-Cycle Fission Gas Release

Fuel rod location	Plenum fission gas content					Fission gas release, %	Kr-85 plenum gamma count rate, cps (b)
	Rod No.	Kr vol. %	Xe vol. %	Xe/Kr(a)	Total, m mole		
AB	15335	0.94	8.49	9.0	4.7	3.8	0.36(c)
B12	15194	0.73	6.23	8.5	3.3	2.6	0.18
B13	15197	0.72	6.00	8.3	3.1	2.5	0.12
B14	15182	0.69	6.03	8.7	3.1	2.6	0.16(c)
BC	15181	0.86	7.47	8.7	4.0	3.2	0.09(c)
C2	15189	0.41	3.33	8.1	1.7	1.4	0.10
C3	15327	0.34	2.00	5.9	1.0	0.8	0.09
C4	15321	0.27	2.10	7.8	1.0	0.8	0.03
C5	15309	0.28	1.96	7.0	1.0	0.8	0.07
C6	15303	0.28	2.35	8.4	1.2	0.9	0.02
C7	15304	0.22	2.00	9.1	1.0	0.8	0.03
C8	14955	0.21	1.80	8.6	0.9	0.7	0.12(c)
CD	15183	0.36	2.82	7.8	1.4	1.2	0.07
D2	15190	0.25	2.00	8.0	1.0	0.8	0.02
D3	15192	0.23	2.10	9.1	1.1	0.8	0.02
AD	15159	0.56	5.60	10.0	2.8	2.2	0.13

(a) Fission yield Xe/Kr = 5.85 (see Reference 33).
(b) Counts/second above background.
(c) Revised values from those in Reference 23.

Table 4-14. Extended Burnup Fission Gas Release

Cycle	Rods	Plenum fission gas, m moles		Fission gas release, %		Average burnup, MWd/mtU
		Average	Range	Average	Range	
3	6	0.5	0.1-1.9	0.6	0.1-2.4	31,940
4	16	1.5	0.5-3.3	1.5	0.5-3.4	39,180
5	16	2.0	0.9-4.7	0.16	0.7-3.8	49,570

Figure 4-21. Five-Cycle Kr-85 Plenum Count Rate Vs Fission Gas Release

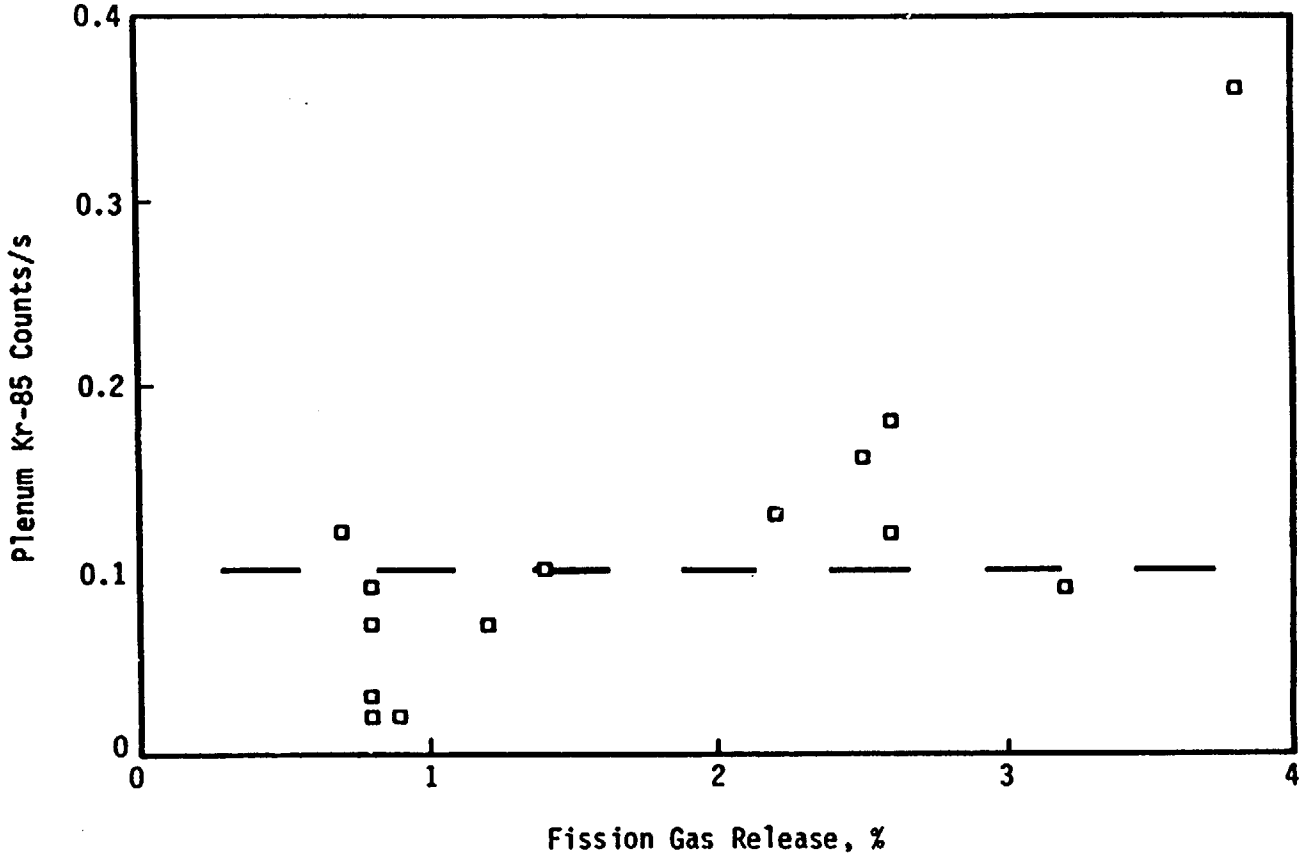

Figure 4-22. Plenum Fission Gas Release (Average and Range) After Three, Four, and Five Cycles

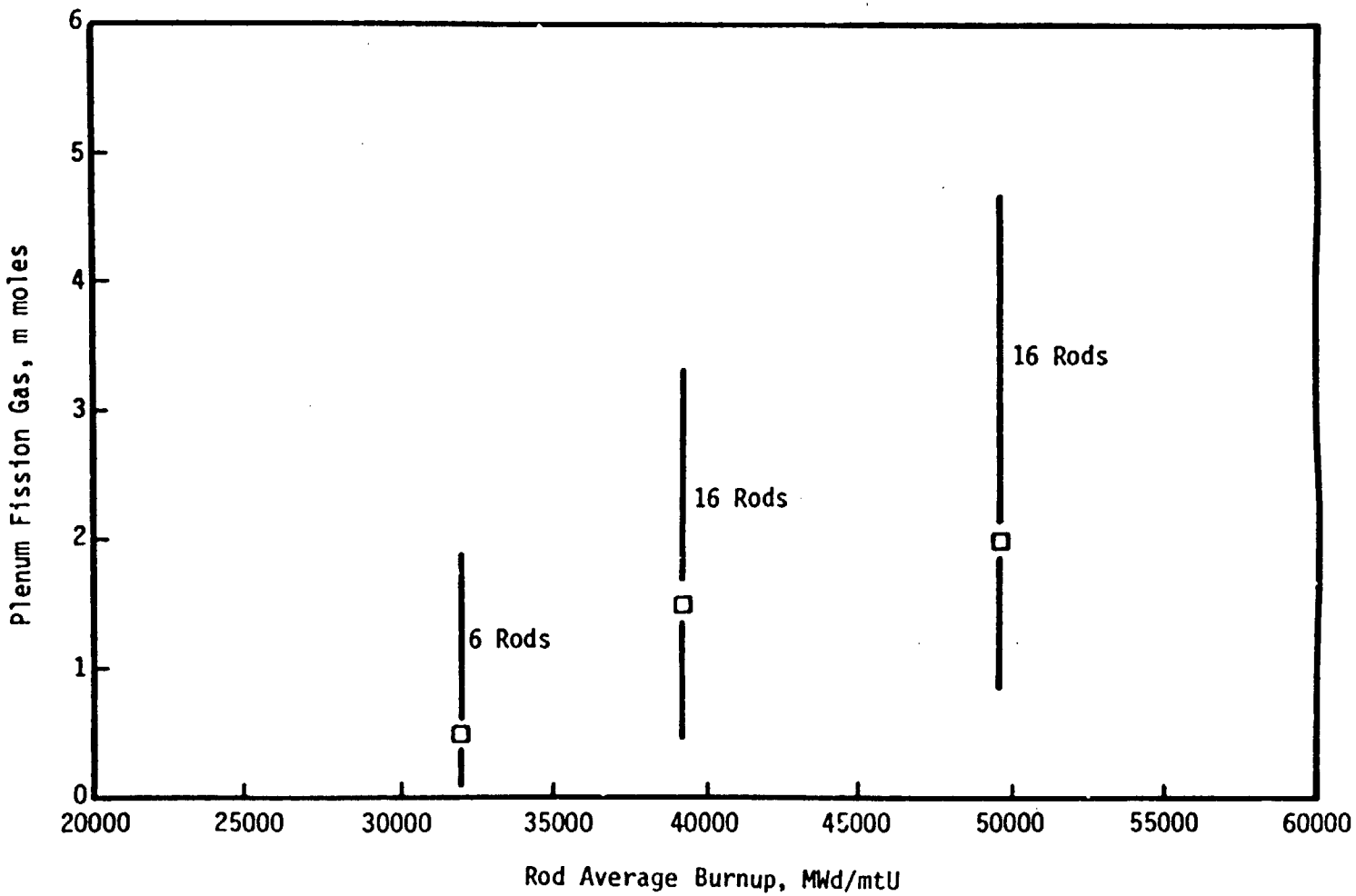

Figure 4-23. Fission Gas Release (Average and Range) After Three, Four, and Five Cycles

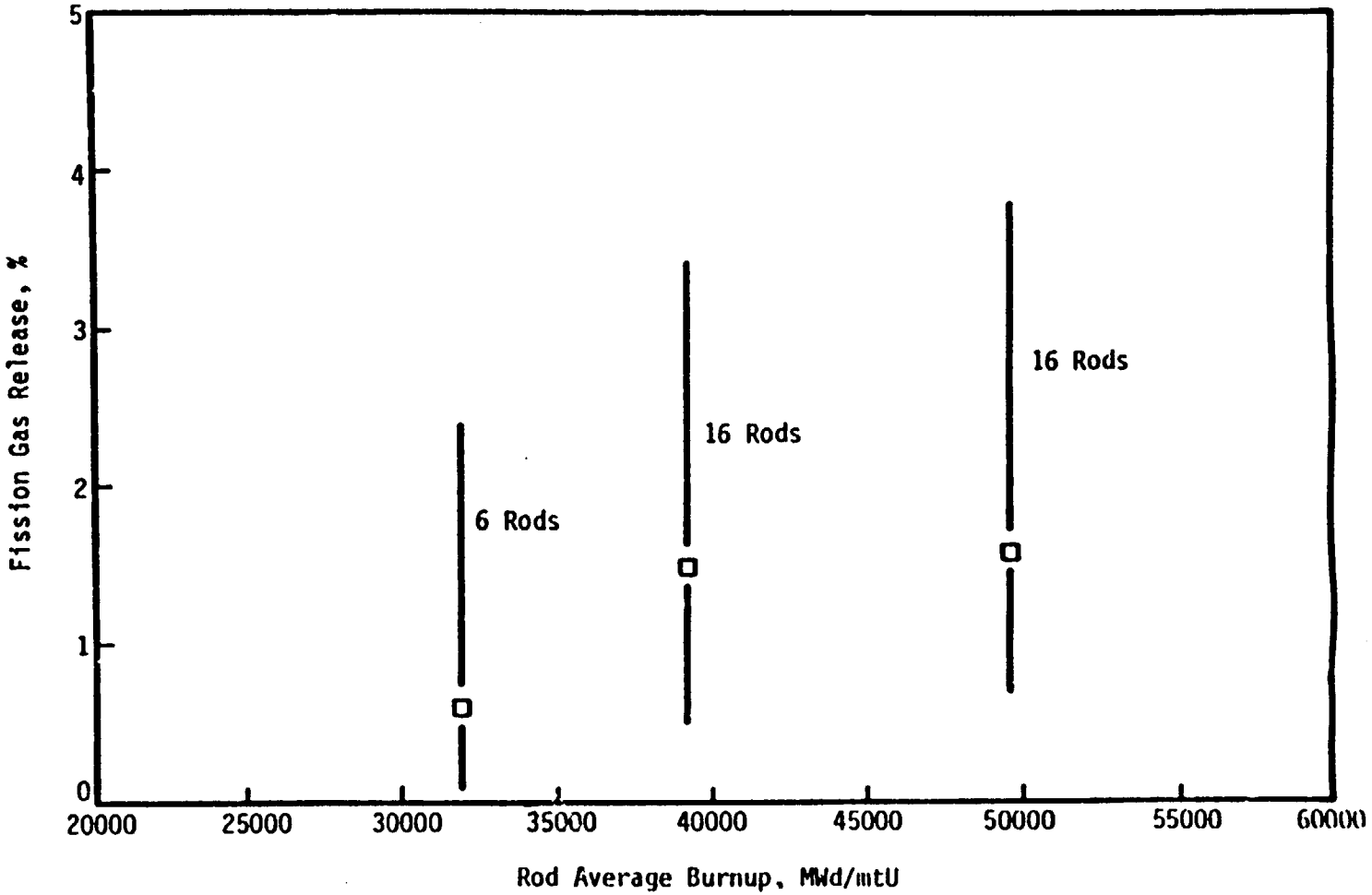

Table 4-15. Five-Cycle Fission Gas Isotopic Abundance

	Kr isotopes, %				Xe isotopes, %				
Rod	83	84	85	86	129	131	132	134	136
14955	9.6	44.8	4.2	41.4	2.0	7.6	24.7	26.6	39.1
15309	10.8	36.9	4.9	47.4	1.0	7.1	23.7	27.6	40.6
15304	11.2	38.8	5.3	44.7	1.4	7.4	24.1	27.2	39.9
15321	10.2	37.2	4.8	47.8	0.8	7.0	24.2	28.0	40.0
15190	11.8	40.0	5.3	42.9	1.5	7.7	23.5	27.5	39.8
15327	11.5	38.9	4.4	45.2	1.4	7.3	23.8	27.8	39.7
15192	11.3	39.2	4.9	44.6	1.2	7.2	24.4	27.2	40.0
15303	10.7	39.3	4.6	45.4	1.1	7.4	23.5	27.9	40.0
15183	12.5	40.4	4.5	42.6	1.6	7.6	24.0	26.7	40.1
15189	10.7	39.6	4.7	45.0	1.4	7.4	24.0	27.6	39.6
15159	9.9	37.4	4.7	48.0	0.7	6.4	23.9	27.9	41.1
15182	11.2	38.2	4.3	46.3	0.8	6.9	23.8	27.7	40.8
15197	10.4	38.9	4.4	46.3	0.7	6.2	24.2	27.7	41.2
15194	10.4	40.0	4.3	45.3	0.8	6.8	24.0	27.8	40.6
15181	10.1	38.8	4.5	46.6	0.6	6.6	23.8	27.8	41.2
15335	10.2	37.3	4.8	47.7	0.9	6.5	23.8	27.8	40.0
5-cycle avg	10.8	39.1	4.7	45.4	1.1	7.1	24.0	27.6	40.3
4-cycle avg	13.2	34.2	7.2	45.4	1.3	9.0	22.3	28.1	39.3
Fission yield	14.8	26.9	7.2	51.2	3.8	13.8	20.2	34.3	27.8

consistent with earlier results from the examinations of sister fuel assemblies after three and four cycles of operation.[27]

4.10. Fuel Rod Sectioning

A destructive examination plan was devised with emphasis placed on characterizing both the general irradiation effects and the unusual features of the rods. The results of the nondestructive phase of the hot cell examination were used to select four rods that best represented the observed phenomena. The selection criteria for these rods were as follows:

Fuel rod No.	Fuel rod location	Selection criteria
15189	C2	Average rod, moderate gas release, and moderate oxide thickness.
15192	D3	Rod bowed to contact, low gas release, and moderate oxide thickness.
15309	C5	Unusual spots, lowest gas release, and high oxide thickness.
15335	AB	Highest gas release.

A sectioning plan for these rods was devised and is shown graphically in Figures 4-24 and 4-25 and summarized in Table 4-16. The general irradiation effects on the cladding were assessed through metallography, hydrogen analyses, and mechanical testing. The metallography benchmarked the oxide thickness at several locations on the rods and characterized the amount of hydride in the cladding. Mechanical testing consisted of both axial and ring tensile tests on defueled cladding pieces. The unusual features on the rods were characterized through metallography and scanning electron microscopy (SEM). Several of the eddy-current indications were characterized metallographically through a successive grind-and-polish technique. The general condition of the fuel was assessed through ceramography, replication/SEM, density, and chemical burnup determinations. A typical rod, 15189, was selected for a fuel density axial profile. The highest gas release rod, 15335, and the lowest gas release rod, 15309, were selected for extensive fuel metallography and a surface replica SEM examination.

The destructive examinations are grouped into the following two categories and are discussed in the section indicated in parentheses:

Figure 4-24. Sectioning Diagram for Rods 15335 (AB) and 15309 (C5)

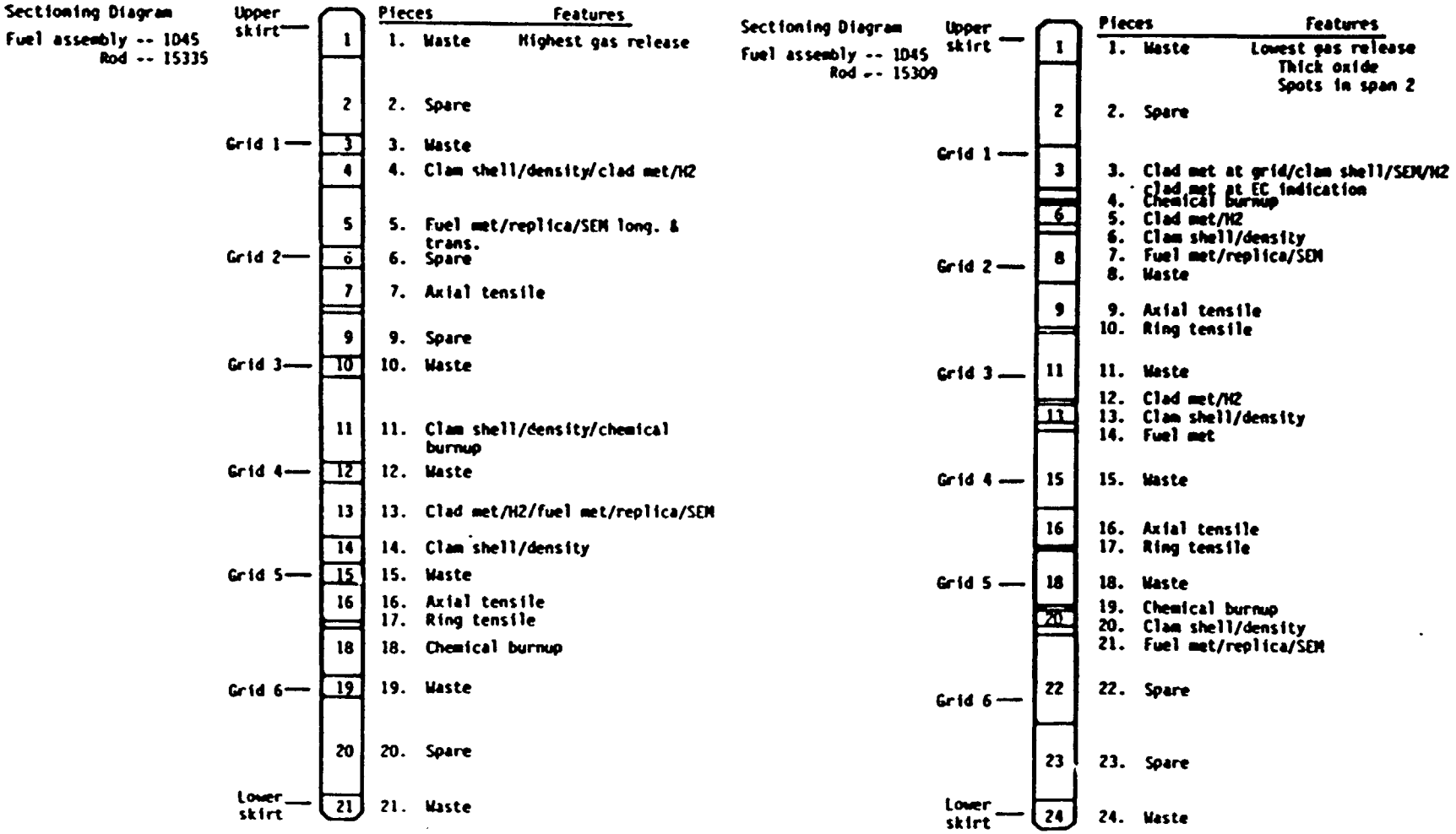

Figure 4-25. Sectioning Diagram for Rods 15189 (C2) and 15192 (D3)

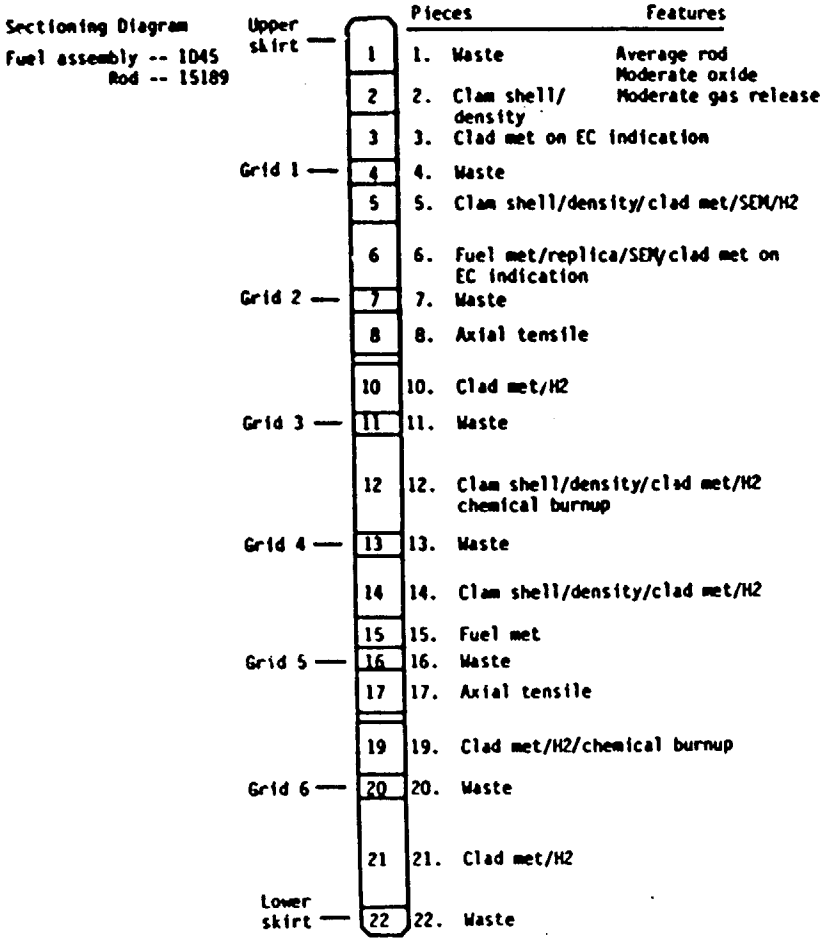

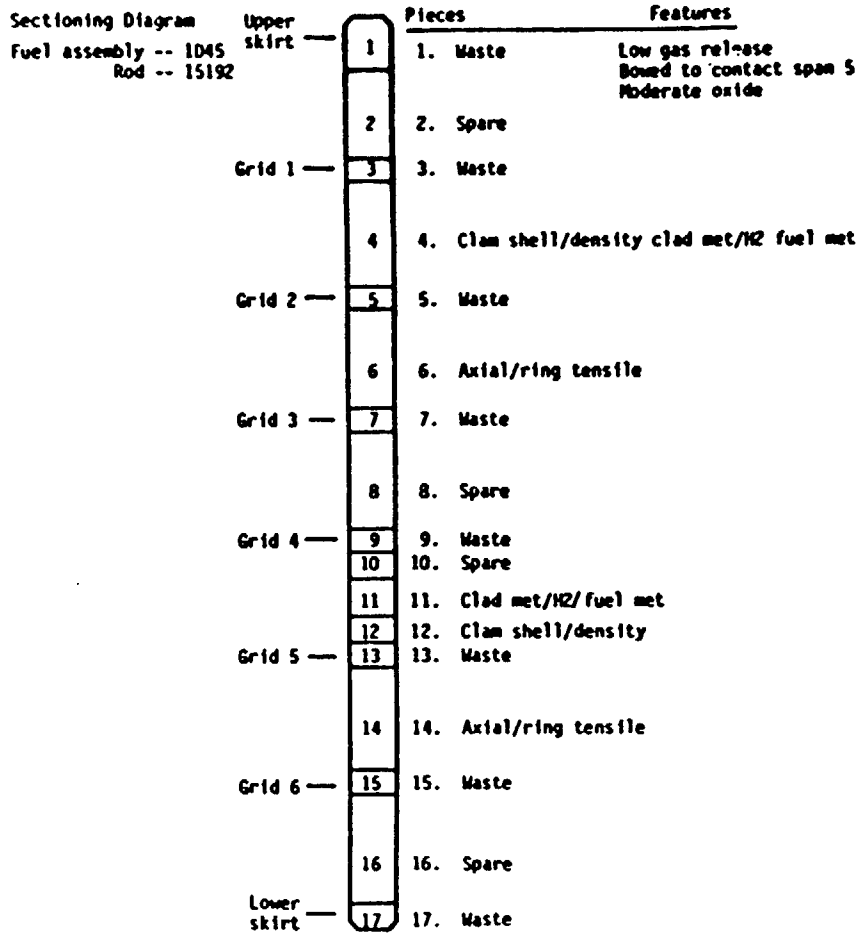

Table 4-16. Destructive Hot Cell Examination

Examination	15189	15192	15309	15'	Total No. of samples
Cladding					
Metallography	6	2[a]	3[a]	2	13
Hydrogen	6	2[a]	2	2	12
SEM	1	0	1	0	2
EC indication	2	0	1	0	3
Axial tensile	2	2	2	2	8
Ring tensile	2	2	2	2	8
Fuel					
Ceramography	2	2	3	3	10
Replica/SEM	1	0	2	3	6
Density	4	2	3	3	12
Chemical burnup	2	0	1	2	5

[a]Numbers of samples from "unusual features" regions are included.

Cladding examinations (section 4.11).

- o Oxide thickness -- metallographic results (section 4.11.1).
- o Hydrogen content (section 4.11.2).
- o Mechanical properties (section 4.11.3).
- o Unusual surface features (section 4.11.4).
- o SEM characterization of cladding surface (section 4.11.5).

Fuel examinations (section 4.12).

- o Microstructure (section 4.12.1).
- o Density (section 4.12.2).
- o Radial fission product distribution (section 4.12.3).
- o Chemical burnup analysis (section 4.12.4).

4.11. Cladding Examinations

4.11.1. Oxide Thickness -- Metallographic Results

Oxide thickness of the five-cycle fuel rod cladding was determined from photomicrographs of 11 samples taken from typical regions. Samples from regions of unusual surface features are discussed in section 4.11.4. Transverse sections from several axial locations were defueled, mounted, ground, and lightly polished to reveal the oxide layer. The samples were metallographically examined and photomicrographs were taken at four orientations at 100 and 500X magnifications. Oxide thicknesses varied with axial position: Oxide layers were thinner near the bottom and thicker toward the top of the rods. As shown previously,[9] this trend in oxide thickness is consistent with the cladding outside diameter (OD) surface temperature profile. The thickest oxide occurred at approximately 120 inches from the bottom of the rod, in the span 2 region.

Measured oxide thicknesses ranged from 12.7 to 63.5μ. These data are given in Table 4-17 and shown as a function of axial position in Figure 4-26. The data in Figure 4-26 represent the average and measured range in thickness for each of the 11 samples measured.

Regions with thicker oxide (>30μ) showed more circumferential variation in thickness, although two of the thicker samples had very uniform oxide layers. There was considerable rod-to-rod variation in oxide thickness (nearly 20μ)

Table 4-17. Hot Cell Metallographic Oxide Thickness Measurements

Sample No.	Location[a]	Orientation, deg[b]				Average, μ
		0	90	180	270	
15189-21	12.6	13.5	12.7	15.9	--	14.0
15189-19	35.9	23.8	25.4	25.4	25.4	25.0
15189-14	58.0	28.6	33.3	28.6	30.2	30.2
15189-12	79.5	36.5	34.9	36.5	34.9	35.7
15189-10	100.1	38.1	38.1	44.5	49.2	42.5
15189-5	127.0	57.2	42.9	36.5	44.5	45.3
15192-4	122.6	52.4	52.4	51.6	52.4	52.2
15309-12	80.7	41.3	39.7	44.5	41.3	41.7
15309-5	120.0	60.3	61.9	55.6	63.5	60.3
15335-13	54.8	27.8	27.0	23.8	24.6	25.8
15335-4	127.3	35.7	50.8	41.3	38.1	41.5

[a]Location is in inches from the bottom of the rod.
[b]Arbitrary reference.

Note: The first five digits of the sample number correspond to the fuel rod number.

Figure 4-26. Five-Cycle Cladding Oxide Thickness Vs Sample Position -- Hot Cell Metallography

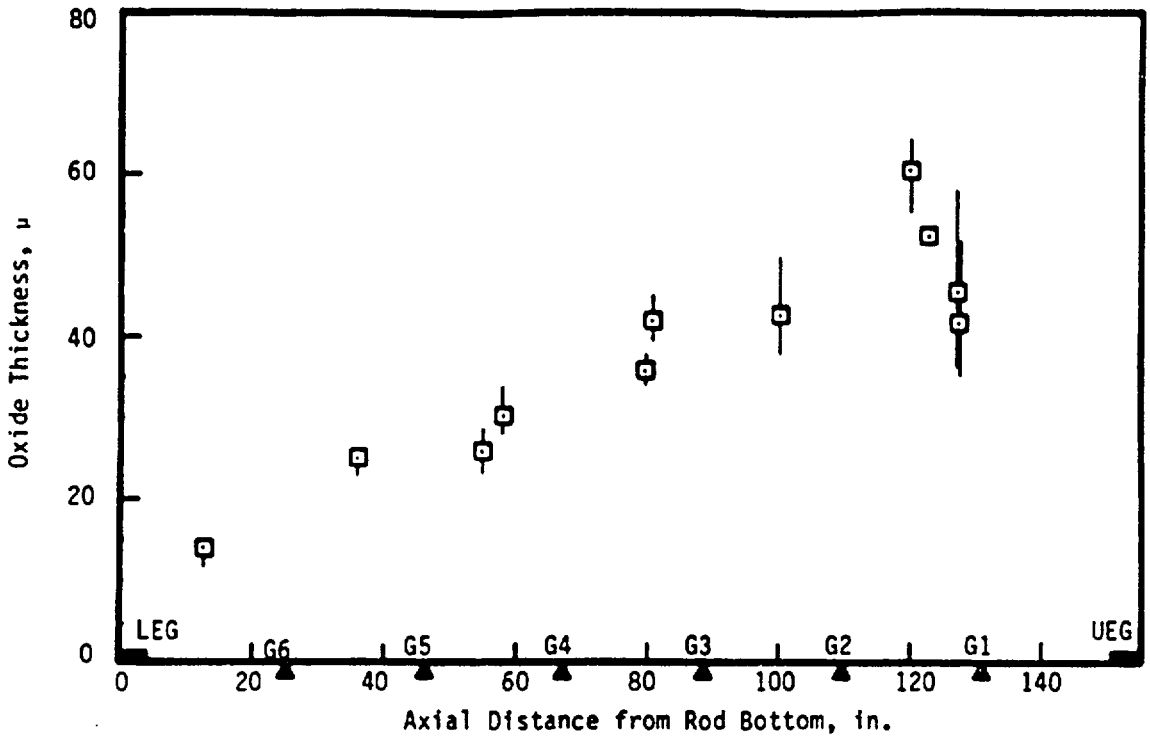

for samples from the thickest region. Examples of the cross-sectional appearance of the oxide layer in the thickest region are shown in Figure 4-27. These micrographs are from sample 15189-5 in the span 2 region.

A comparison of the average oxide thickness of four- and five-cycle samples is shown in Figure 4-28, where the data are plotted versus axial position. The average oxide thickness of 7 four-cycle samples ranged from 5.2 to 24.4μ and was nearly uniform around the circumference. The average oxide thickness of the 11 five-cycle samples ranged from 14.0 to 60.3μ. The curves shown in Figure 4-28 are trend lines through the data and indicate that the rate of oxidation during the fifth cycle was higher in the upper portion of the rods. These data were used to correct the cladding diameter as discussed in section 4.4.

4.11.2. Hydrogen Content

Cladding hydrogen content was measured by hot vacuum extraction in 11 samples that were situated adjacent to cladding metallography samples. Equipment calibration was verified by analyzing traceable standard samples from the National Bureau of Standards (NBS). Reported results are the average of two analyses per sample. Hydrogen levels in the five-cycle samples ranged from 106 to 408 ppm, with the highest levels occurring in the span 2 region. Hydrogen content values for the 11 samples are given in Table 4-18. Hydrogen content of the four-cycle cladding measured previously ranged from 64 to 182 ppm. As shown in Figure 4-29, axial profiles of the four- and five-cycle cladding hydrogen content are similar to the oxide thickness profiles shown in Figure 4-28. Since the solubility limit of hydrogen in Zircaloy at 650F (approximately the mean cladding operating temperature) is about 200 ppm, some zirconium hydrides would have been present in the upper half of the five-cycle rods during operation.

Cladding hydrogen pick-up fractions are listed in Table 4-18 and shown as a function of oxide thickness in Figure 4-30. The pick-up fraction represents the fraction of hydrogen liberated during oxidation that is absorbed by the cladding. The trend of the data shown in this figure is a decrease in pick-up fraction with increasing oxide thickness, at least up to the 40 to 50μ range. Data from samples with thicker oxide suggest that the decreasing trend in pick-up fraction may level off to a value of about 15%.

Figure 4-27. Micrographs of the Oxide Layer on Five-Cycle Fuel Cladding (Sample No. 15189-5A4)

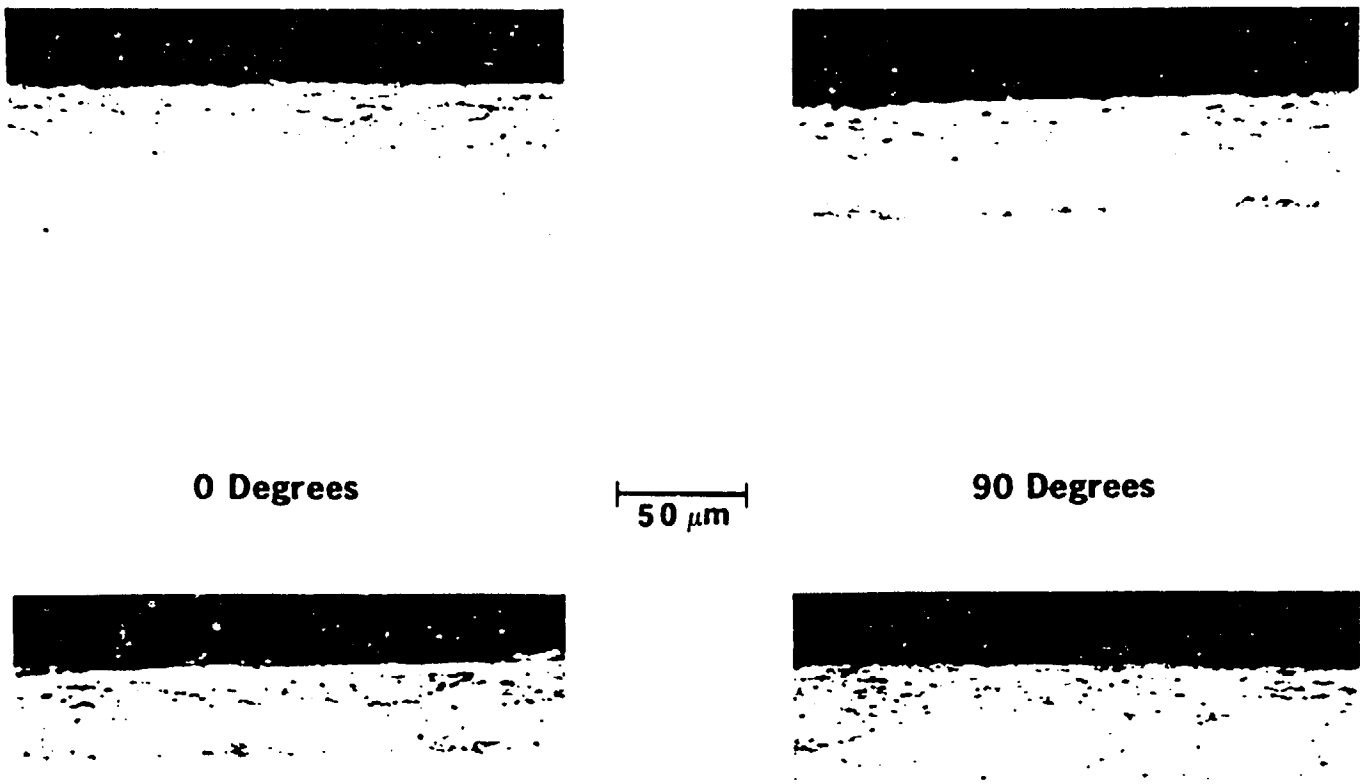

(a) Arbitary reference orientation.

Figure 4-28. Comparison of Four- and Five-Cycle Average Oxide Thickness Vs Axial Position -- Hot Cell Metallography

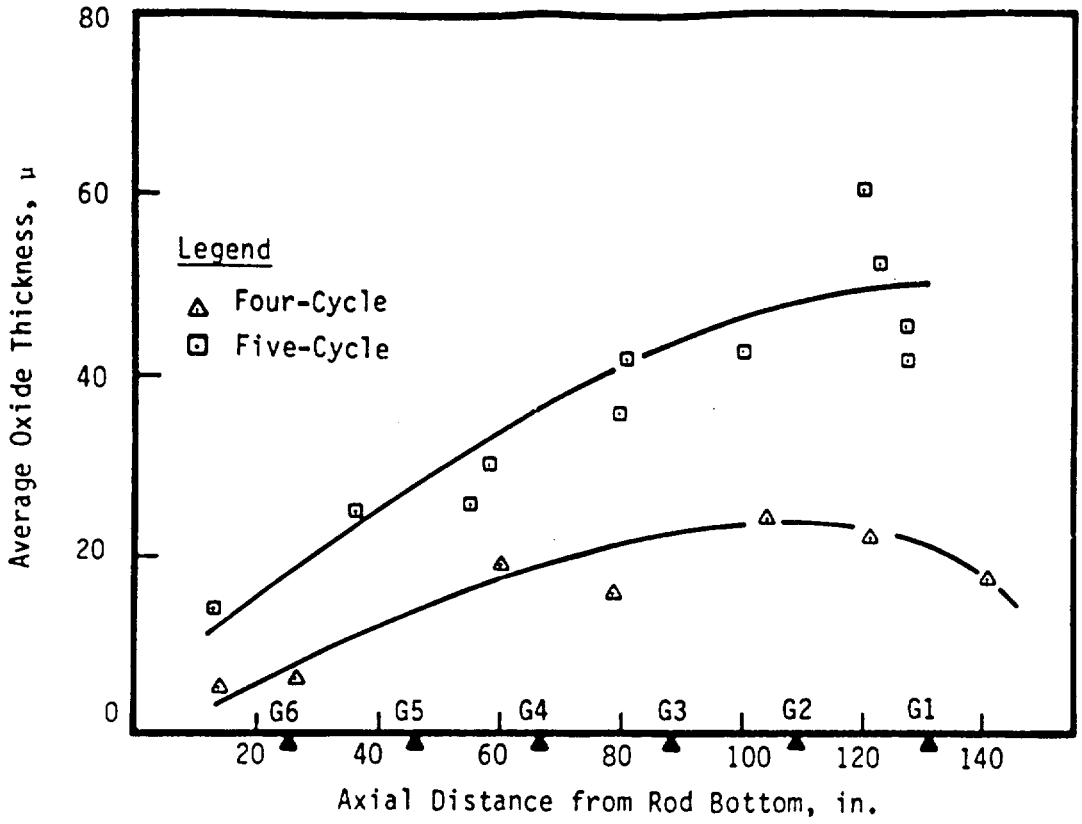

Table 4-18. Five-Cycle Cladding Hydrogen Content and Pick-up Fraction

Sample No.	Location[a]	Hydrogen, ppm	Pick-up Fraction, %
15189-21	12.8	106	17.8
15189-19	36.2	142	13.4
15189-14	57.9	190	14.8
15189-12	79.4	257	16.9
15189-10	99.9	258	14.3
15189-5	127.3	268	13.9
15192-4	122.7	326	14.7
15309-12	80.8	236	13.3
15309-5	119.9	408	15.9
15335-13	54.9	164	14.9
15335-4	127.3	203	11.5

[a]Location in inches from the bottom of the rod.

Note: The first five digits of the sample number correspond to the fuel rod number.

Figure 4-29. Axial Cladding Hydrogen Content Profiles -- Four- and Five-Cycle Samples

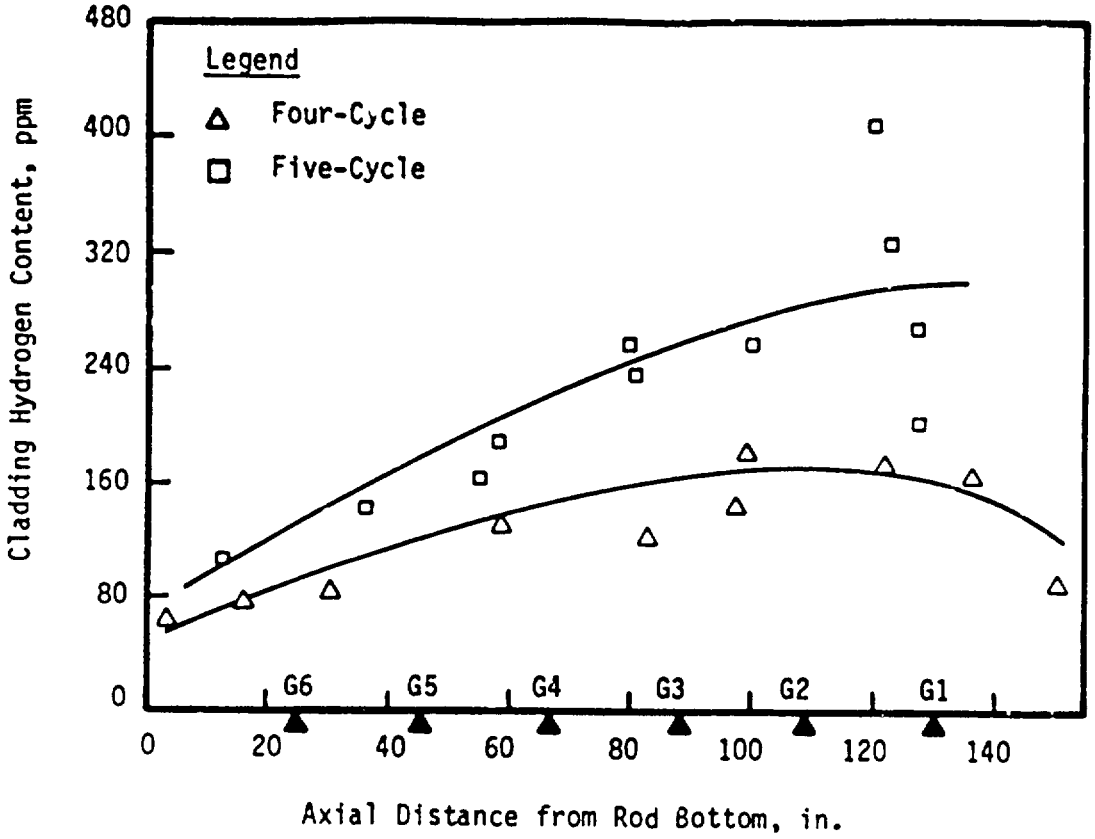

Figure 4-30. Cladding Hydrogen Pick-up Fraction Vs Oxide Thickness of Four- and Five-Cycle Samples

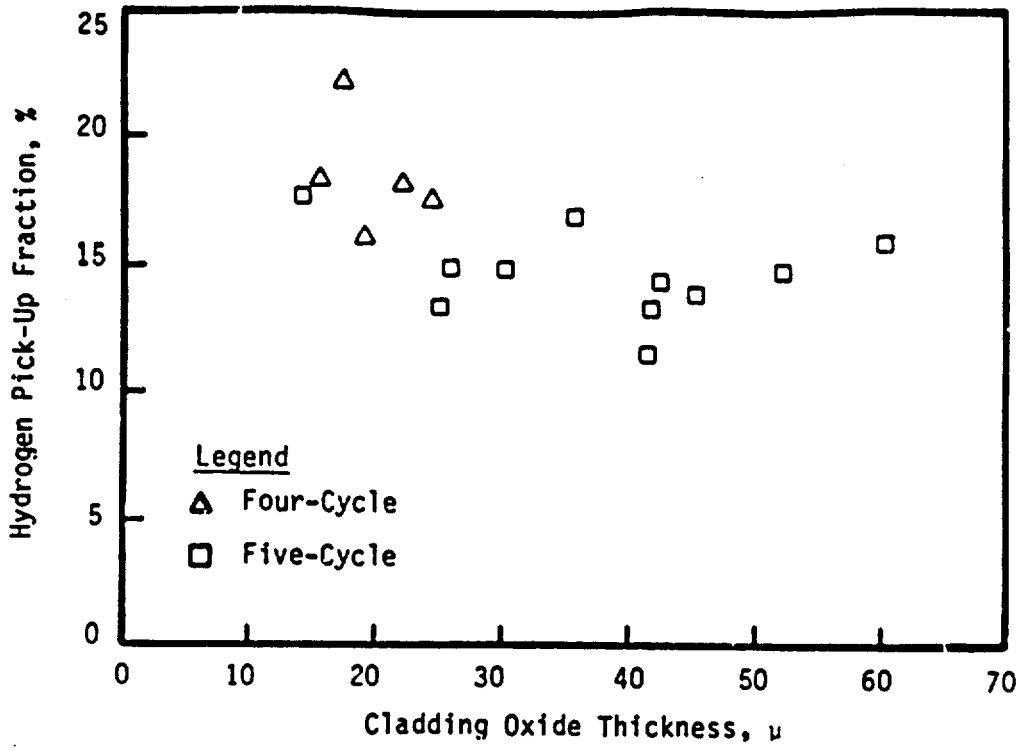

Hydride morphology in the five-cycle cladding was determined by polishing and etching the samples used to measure oxide thickness. In all cases, the hydride platelets were circumferentially oriented, with no significant radial component. Platelet density across the cladding wall was generally higher toward the OD surface. Also, at a given axial location, the hydride platelets appeared more densely distributed beneath the thinner oxide layers, indicating the tendency for the hydrogen to diffuse to the cooler region of the cladding. Typical examples of the appearance of the cladding hydrides in the five-cycle samples are shown in Figure 4-31.

4.11.3. Mechanical Properties

Post-irradiation mechanical properties of the five-cycle cladding were determined from axial and ring tension tests conducted at elevated temperatures. Testing was carried out in the hot cell at 650F and a strain rate of 0.005/min with an Instron test frame equipped with a three-zone split-tube furnace. Both types of tests provide uniaxial property data. The ring tension tests were conducted to provide data in the circumferential direction. Results of the tests are described in the following sections.

4.11.3.1. Axial Tension Tests

Tension tests were conducted on eight samples from high-burnup (approximately 54,000 MWd/mtU) regions on four rods. Two samples from each rod represented regions of equivalent burnup, but with low and high irradiation temperatures. A high-temperature extensometer was used to measure uniform strain in a 2-inch gage length through maximum load at a constant strain rate. Testing was then continued to failure at a constant crosshead rate of 0.1 inch per minute. Stress values were calculated from oxide-corrected cross-sectional areas for each sample.

Results from the axial tension tests are given in Table 4-19, and a comparison of four- and five-cycle average results is shown in Table 4-20. Cladding strength levels of the five-cycle samples were essentially the same as those after four cycles, but a decrease in uniform elongation was observed. The uniform elongation values also did not exhibit the scatter normally observed in this type of test. Axial tensile strengths and elongation data through the five cycles of irradiation are shown as a function of burnup in Figures 4-32 and 4-33. The data shown in these figures

Figure 4-31. Micrographs of Five-Cycle Cladding Hydrides (Sample No. 15189-5A4)

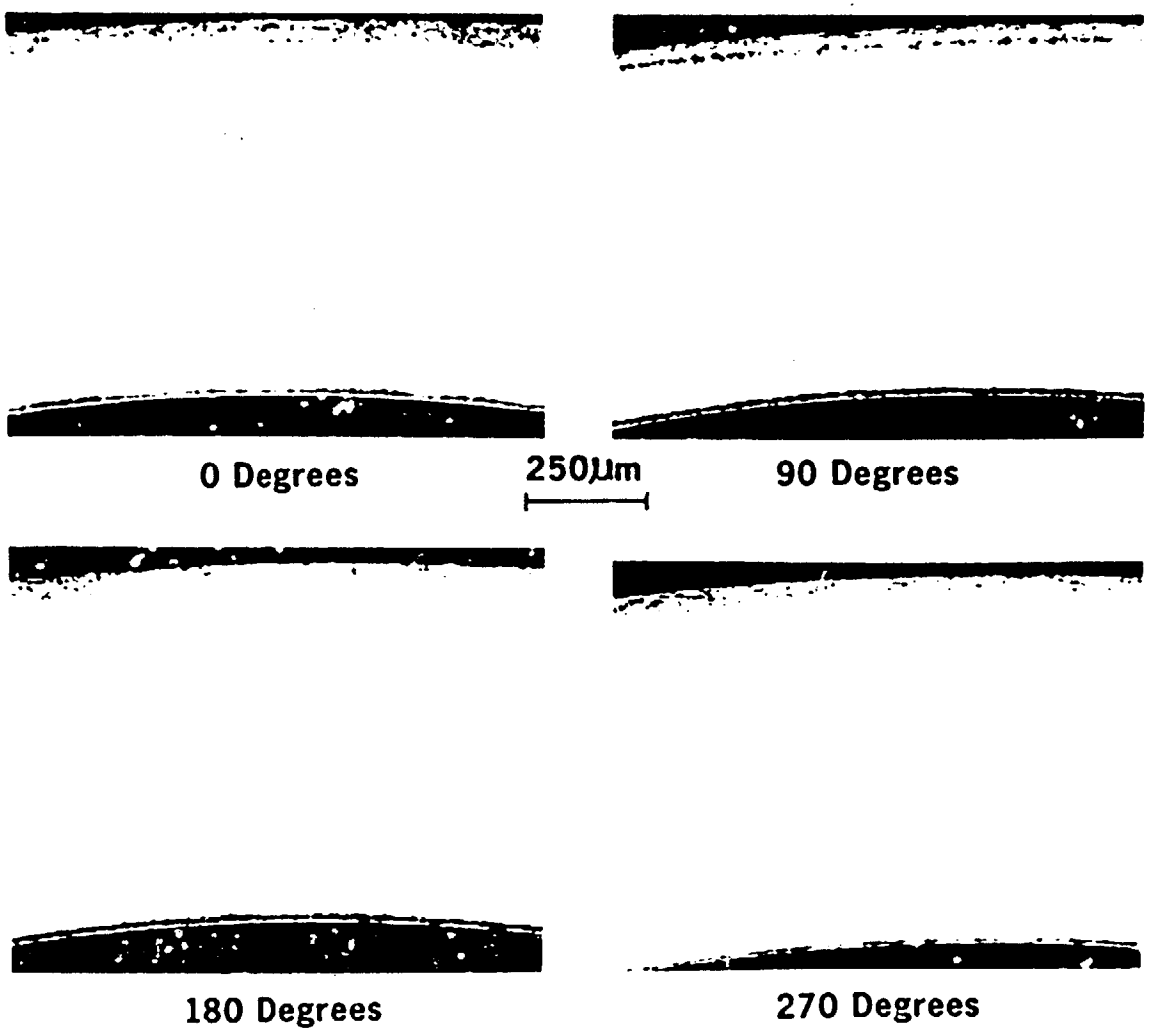

(a) Arbitary reference orientation.

Table 4-19. Five-Cycle Cladding Tensile Properties -- Axial Tension Tests

Sample No.	Location[a]	Strength, ksi		Elongation, %	
		Yield (0.2% offset)	Tensile	Uniform	Total
15189-17	40.8	91.54	103.54	1.30	13.17
15189-8	104.7	89.10	100.47	0.93	8.34
15192-14	35.9	89.51	104.94	1.43	15.31
15192-6	100.2	85.62	102.81	1.39	7.83
15309-16	57.7	90.06	105.59	1.37	13.01
15309-9	99.7	84.12	102.99	1.20	5.68
15335-16	41.0	90.03	101.23	1.38	24.06[b]
15335-7	104.8	82.30	97.52	1.30	14.37

[a] Locations are in inches from the bottom of a rod to the center of each 7-inch sample.

[b] Suspect data.

Note: The first five digits of the sample number correspond to the fuel rod number.

Table 4-20. Comparison of Four- and Five-Cycle Average Cladding Axial Tensile Properties

	Average Results	
	Four-Cycle	Five-Cycle
Yield strength (0.2% offset), ksi	88.1 (1.51)[a]	87.8 (1.50)
Tensile strength, ksi	100.8 (1.39)	102.4 (1.41)
Uniform elongation, %	2.1 (0.66)	1.3 (0.41)
Total elongation, %	15.5 (0.75)	12.7 (0.62)

[a] Irradiated/unirradiated.

Figure 4-32. Cladding Strength at 650F Vs Burnup -- Axial Tension Tests

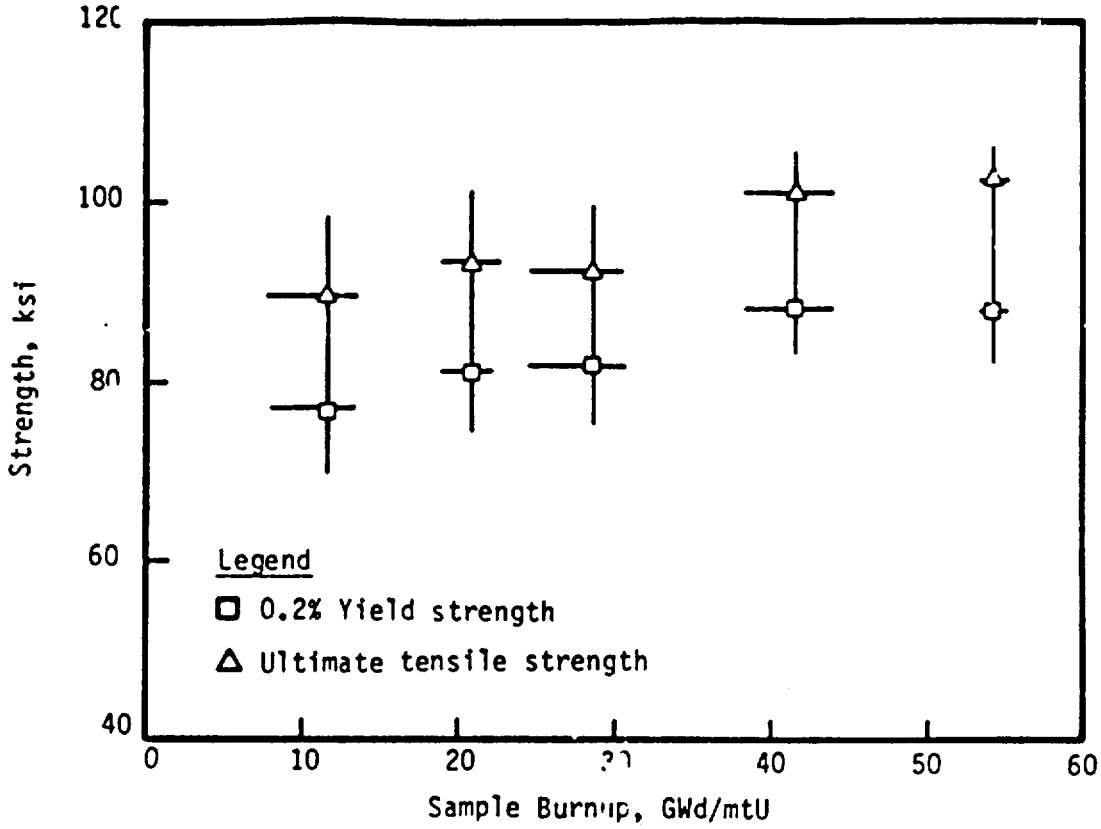

Figure 4-33. Cladding Elongation at 650F Vs Burnup -- Axial Tension Tests

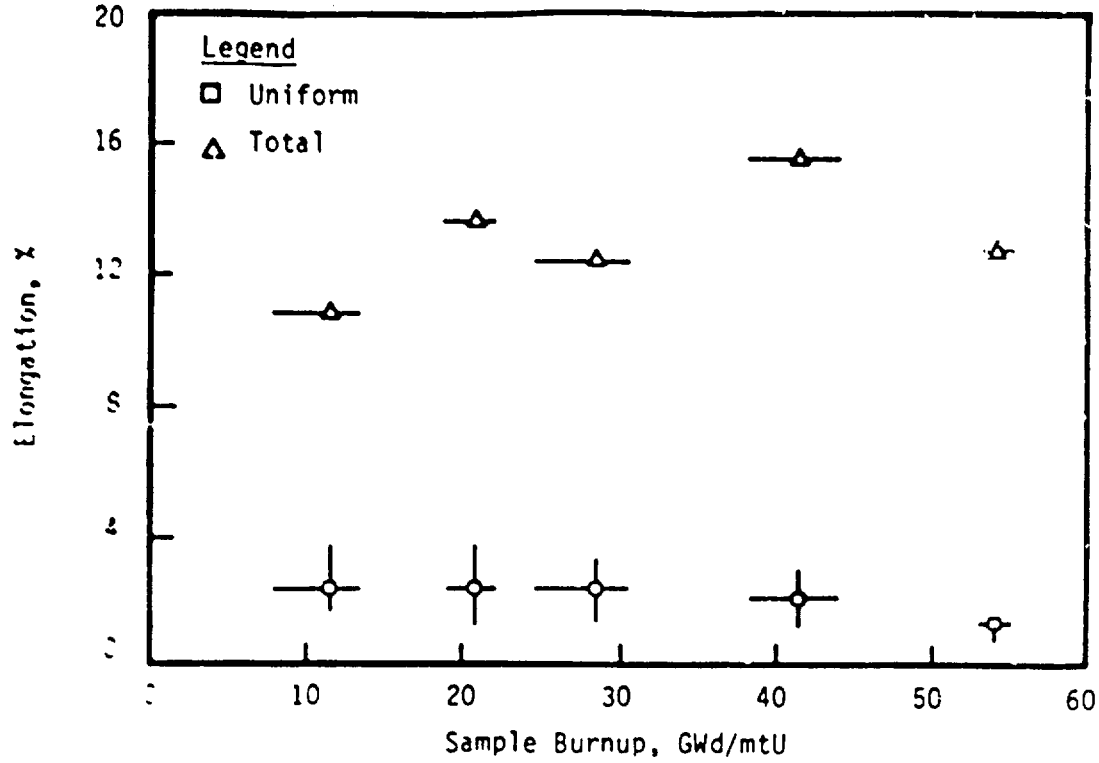

are the average and range of each set of samples tested under the same conditions.

After five cycles, the average yield strength was 87.8 ksi, a 50% increase over the irradiated value. The average ultimate tensile strength of 102.4 ksi represents a 41% increase. The strengthening of Zircaloy-4 with irradiation is well documented, and these values fall within the expected range for high burnup cladding.

Uniform plastic elongation of the five-cycle samples averaged 1.3%, with little scatter in the values. After five cycles, the cladding retained 41% of the original uniform elongation; after four cycles, 66% was retained. This drop in uniform elongation during the fifth cycle cannot be directly attributed to the presence of hydrides in the cladding at elevated temperature. Little difference exists in the uniform elongation data even though the hydrogen content of the samples ranged from 150 to 440 ppm. The samples taken from the lower portion of the rods are expected to contain hydrogen in solution whereas the samples from the upper portions are expected to have retained hydride precipitates during the 650F tests. The observed decrease may be due to a change in the irradiation-induced characteristics of the cladding as compared to the four-cycle condition or to increased levels of interstitials.

Total plastic elongation averaged 12.7% for the 8 five-cycle samples. This average value is 62% of the unirradiated total ductility, but the irradiated data fall into two sets. The total elongation of samples from higher rod positions averaged only 9.1%, while samples from lower rod locations averaged 16.4% total plastic elongation. These averages suggest that the presence of hydride precipitates in the cladding at test temperature may decrease the total elongation. See Appendix B for data on unirradiated cladding axial tension tests where high levels of hydrogen were shown to reduce total elongation at 650F, but not uniform elongation.

4.11.3.2. Ring Tension Tests

Ring tension samples, nominally 0.25 inch in length, were sectioned from the five-cycle rods adjacent to each of the axial tension samples. The defueled rings and four samples of unirradiated cladding were tested in-cell on the Instron load frame using specially built, split-mandrel grips. The nominal

sample length of 0.25 inch was chosen to give a width-to-thickness ratio of 9.4:1. Zircaloy ring samples have been shown to exhibit consistent test results when the width-to-thickness ratio is greater than 9:1.[34] A boron-nitride lubricant was used to minimize friction between the mandrel and ring samples. Samples were pulled with the test frame at a constant crosshead speed of 0.002 in./min through maximum load, then at 0.02 in./min to failure. If the sample gage length is assumed to be equal to the mean diameter, and frictional forces are minimized, the 0.002 in./min crosshead speed corresponds to an initial strain rate of 0.005/min. However, this test is not a standard one, and data derived therefrom are only useful for determining relative change -- not for direct comparison with the axial tension tests.

Strength and ductility results from the eight samples tested are given in Table 4-21. After five cycles, the average yield strength (0.2% offset) was 72.0 ksi and the average tensile strength was 96.7 ksi, which represent increases of 46 and 36%, respectively, over unirradiated values. The ring tensile strength data show about 5% less radiation enhancement than the axial tests. Plots of ring tensile and yield strength data after 1, 2, and 5 cycles of irradiation are shown as a function of sample burnup in Figure 4-34. The plots show the average and range of data for each set of samples.

The effect of irradiation on ductility in the circumferential direction differed from that observed in the axial direction. The average uniform elongation (to maximum load) after five cycles was 2.5% and the average total elongation was 6.3%, which are 78 and 33%, respectively, of the unirradiated values. Elongation data in the circumferential direction are shown as a function of sample burnup in Figure 4-35. The figure shows that uniform elongation in the circumferential direction, unlike uniform elongation in the axial direction, did not decrease further at high burnup. Total elongation had a sharper decrease with irradiation, but the loss of ductility appears to be saturating.

Fractured five-cycle ring samples are shown in Figure 4-36. The photographs show ductile failure of the samples by shear in all cases. The extent of cladding oxidation is also evident from the amount of spallation that occurred in the high-strain portion of the samples.

Table 4-21. Five-Cycle Ring Tension Mechanical Properties

Sample	Location[a]	Strength, ksi		Elongation, %	
		Yield (0.2% offset)	Tensile	Uniform	Total
15189-18	37.1	75.18	97.54	2.0	4.0
15189-9	101.0	67.38	95.68	2.5	7.0
15192-14	32.2	75.23	102.21	2.0	3.8
15192-6	96.6	65.40	98.82	3.0	6.4
15309-17	54.0	68.59	98.93	2.9	6.1
15309-10	96.0	77.95	96.37	2.4	8.4
15335-17	37.3	72.39	93.40	2.4	8.4
15335-8	101.2	73.80	90.34	2.8	6.2
Average	--	72.0	96.7	2.5	6.3

[a]Locations are in inches from the bottom of the rod.

Note: The first five digits of the sample number correspond to the fuel rod number.

Figure 4-34. Cladding Strength Values at 650F Vs Burnup -- Ring Tension Tests

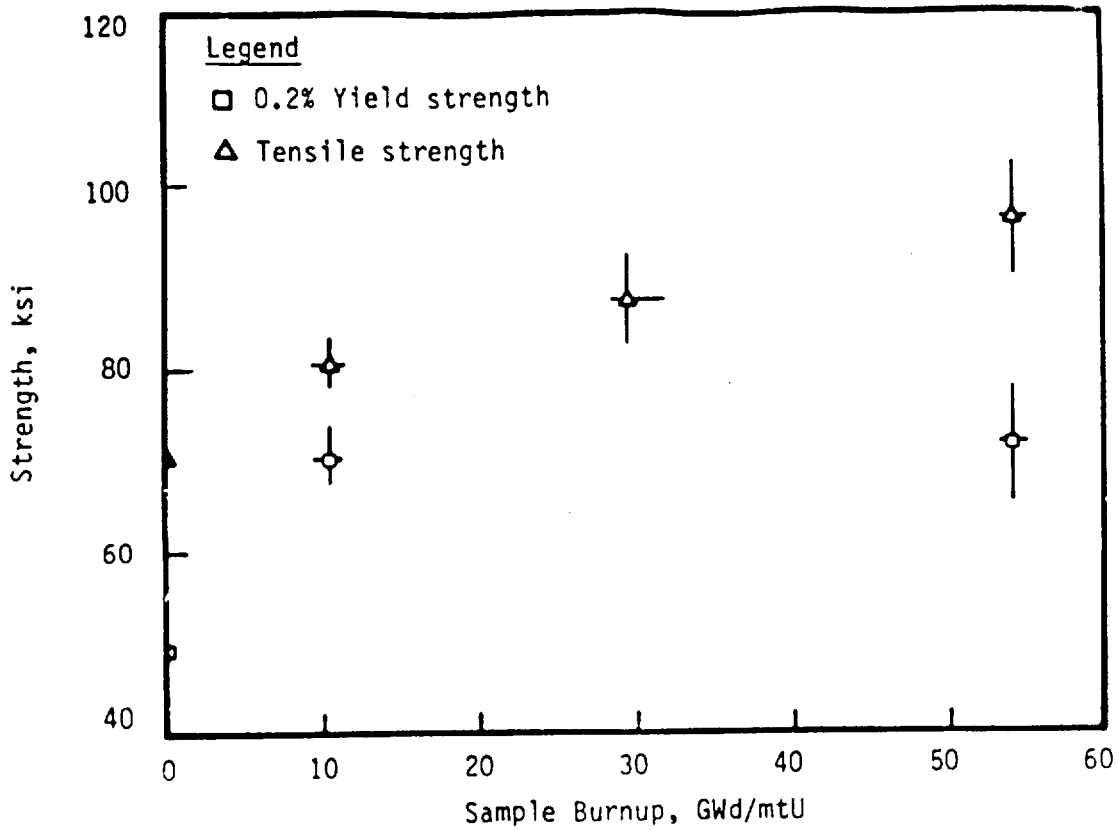

Figure 4-35. Cladding Elongation at 650F Vs Burnup -- Ring Tension Tests

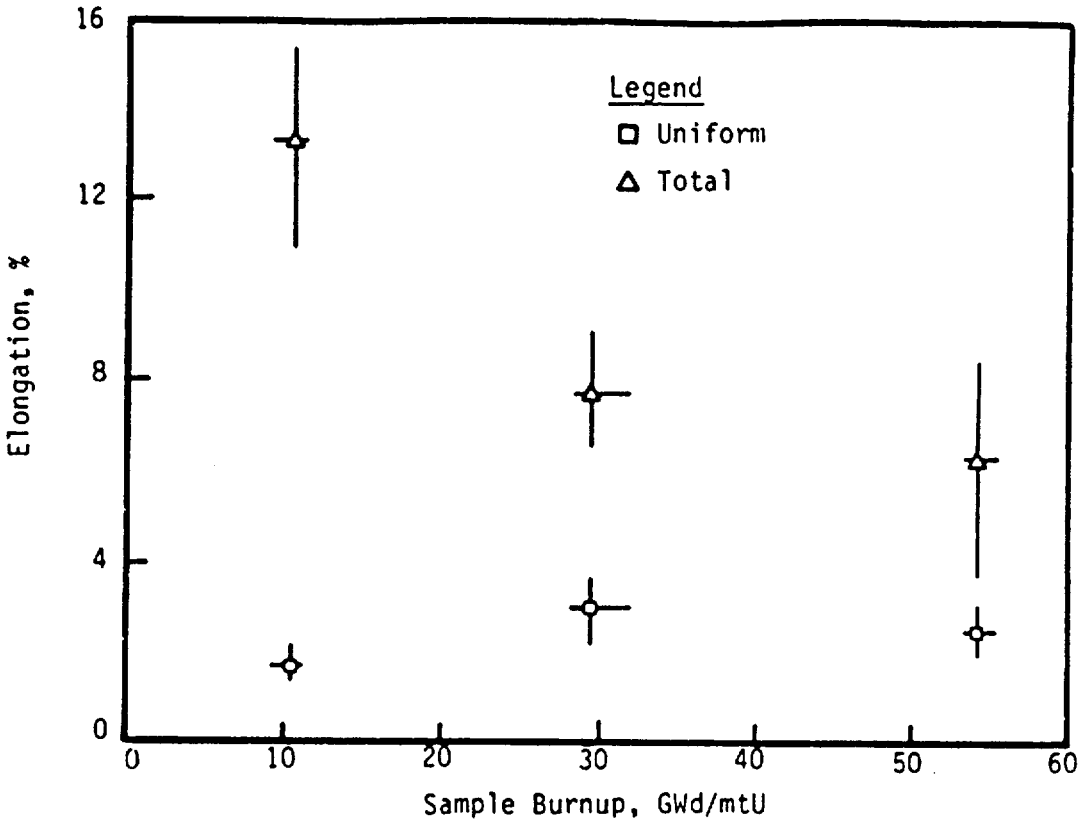

Figure 4-36. Macroviews of Ring Tension Sample Fracture Regions

4.11.4. Metallography of Unusual Surface Features

Poolside visual examinations of the extended burnup assembly revealed fuel rod surface features for which there was no immediate explanation. Dark spots were observed over the upper half of span 2 on the face C rods. The spots were shaped like elongated ovals. Although the spots resembled blisters, no significant surface relief that might indicate degradation of cladding integrity was observed. In another area, two adjacent rods in the span 5 region on face D of the assembly were bowed to near contact. This was first noted during the visual examination after the fourth cycle, which means that the bowed rods may have operated in a condition of reduced localized cooling for up to two cycles.

Diameter profiles of these areas obtained in the hot cell indicated that the spots and the near-contact region of the bowed rods were raised slightly in relief of the OD surface. Eddy-current oxide thickness profiles indicated that the areas had a significantly thicker oxide film. Sections of these features were removed for metallographic examination to better characterize the condition of the cladding wall. Results of the metallography are discussed in the following sections.

4.11.4.1. Span 2, Face C Spots

The visual appearance of the spots seen at poolside on face C of assembly 1D45 is shown in Figure 4-37. Spots were present on nearly all the rods and appeared to be most severe on rods C7 and C8. However, eddy-current oxide thickness measurements indicated that the greatest apparent thickness was on rod C5 (Serial No. 15309). A 9-inch section was cut from rod 15309, sub-sectioned, and longitudinally slit open. Photographs of the OD and inside diameter (ID) surfaces of the cladding are shown in Figure 4-38. The ID surface showed no unusual features or signs of degradation. The location of spots on the OD surface did not correlate with any specific fuel pellet or ID surface features. Thus, the conclusion was reached that the spots were not due to conditions within the rod; rod puncturing had previously verified the integrity of the cladding wall.

A spot corresponding to a high oxide thickness level (as indicated by eddy-current measurements) was sectioned from the cladding and transversely mounted for metallographic examination. The sample was ground flat, lightly

Figure 4-37. Poolside View of Spots on Face C, Span 2 of Assembly 1D45

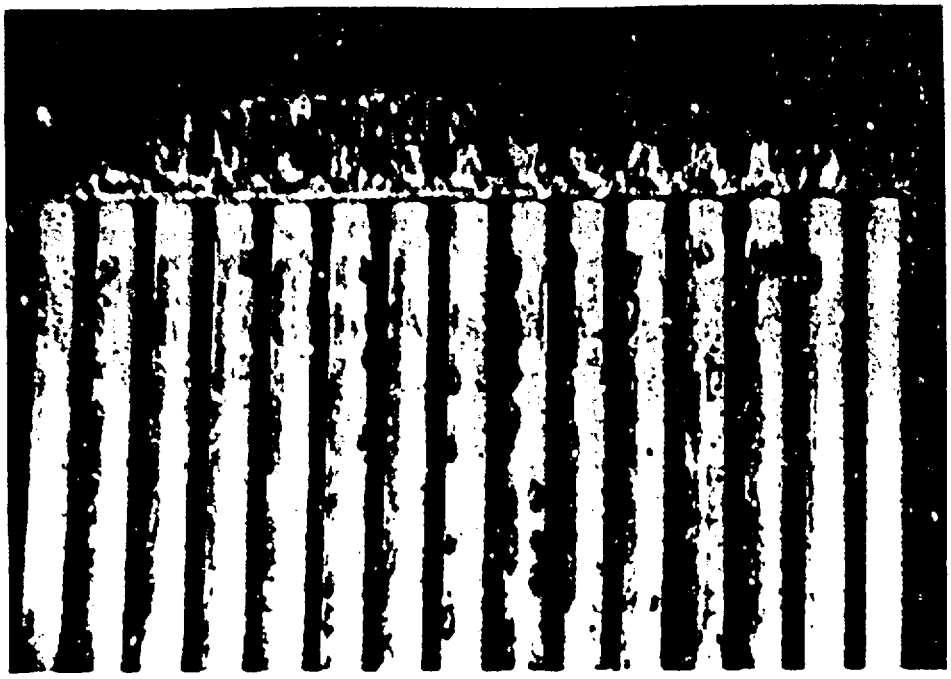

Figure 4-38. Clam-Shelled Rod Segment 15309 in the Region of Spots

polished, and examined in several successive steps. In cross section, the spot was found to be a localized region of increased cladding oxidation, with some evidence of oxide spallation. There was a corresponding loss of cladding wall thickness associated with the thicker oxide. The loss was about 50% greater than can be accounted for by the measured oxide thickness, indicating that some spalling of oxide had occurred. No deep oxide penetrations into the wall or other forms of damage were observed.

Micrographs of the cladding cross section in the region of a typical spot are shown in Figure 4-39. In these photographs, the sample had also been etched to reveal cladding hydrides. The area of cladding under the thicker oxide has less hydriding, indicating that the wall was hotter there and that the hydrogen migrated to cooler regions adjacent to the spot. The two grinding steps shown in the figure are about 0.125 inch apart axially. The oxide layer in the second-grind micrographs shows evidence of spalling and circumferential cracking near the metal/oxide interface. Maximum oxide thickness at this step is about 95μ. Micrographs of the fourth grinding step show limited spallation and no cracking of the oxide. Maximum thickness of the oxide at this step is about 110μ.

Oxide thickness and cladding wall thickness after the second and fourth grinds are shown as a function of circumferential position in Figure 4-40. In this figure, the spot is seen as a region of thicker oxide (up to 50μ greater than the base level of 50 to 60μ), covering about 40 degrees of the cladding circumference. The wall thickness plot shows a shallow, uniform loss in cladding of about 0.5 to 1.0 mil under the spot.

4.11.4 2. Span 5, Face D Bowed Region

Poolside photographs (see Figure 4-41) of face D of assembly 1D45 showed rods D2 and D3 virtually in contact in the span 5 region. Both rods were nondestructively examined in the hot cell and found to have a 4- to 5-inch axial region of higher oxide thickness corresponding to the near-contact region. This region was sectioned from rod D3 (Serial No. 15192) for further examination. The 270-degree view in the figure corresponds to the portion of the rod bowed against rod D2. A discolored region 5 inches long corresponds to the region of higher oxide thickness indicated by eddy-current measurements.

Figure 4-39. Micrographs of Transverse Section Through Spotted Region of Rod 15309

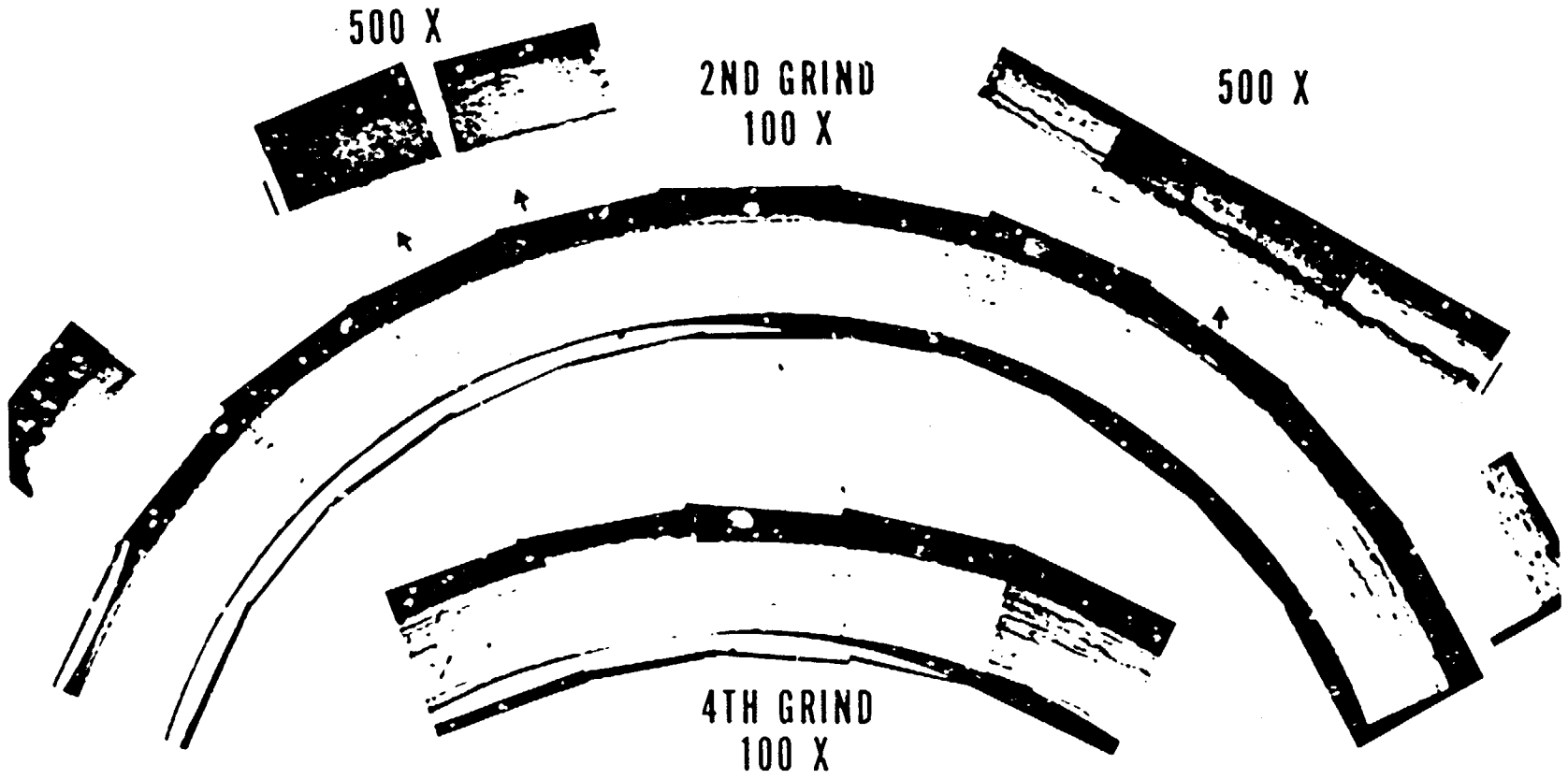

Figure 4-40. Circumferential Profiles of Oxide Thickness and Wall Thickness in the Spotted Region of Rod 15309

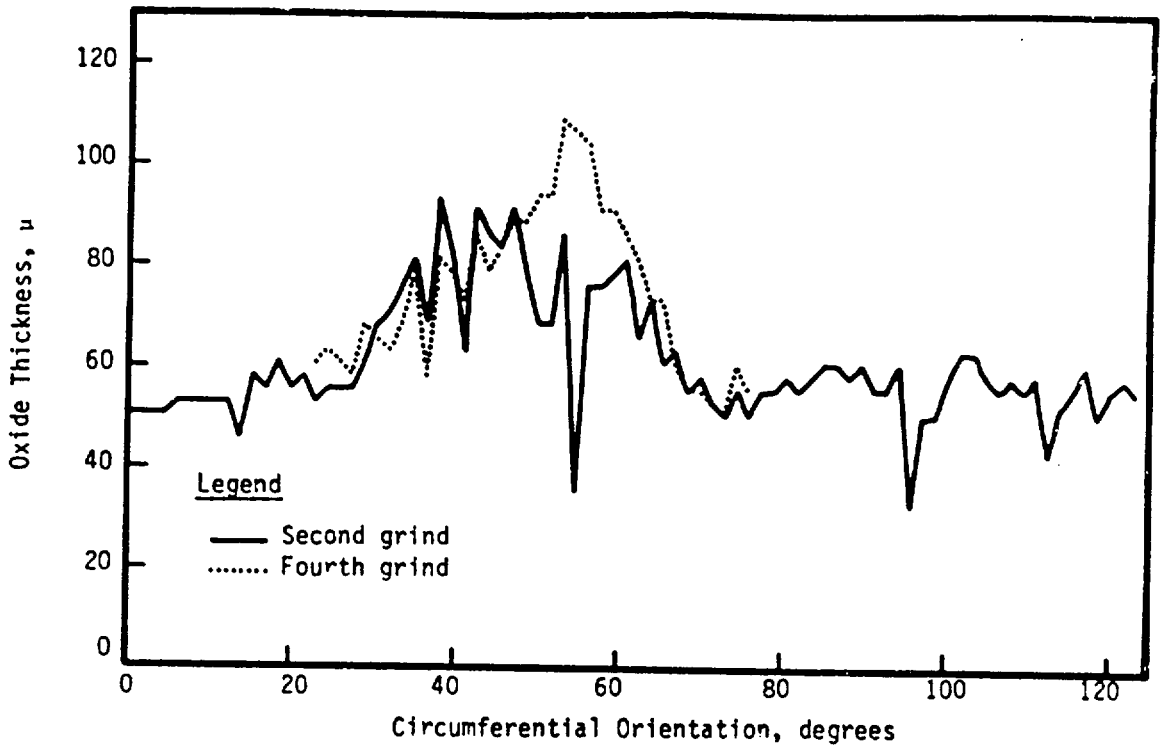

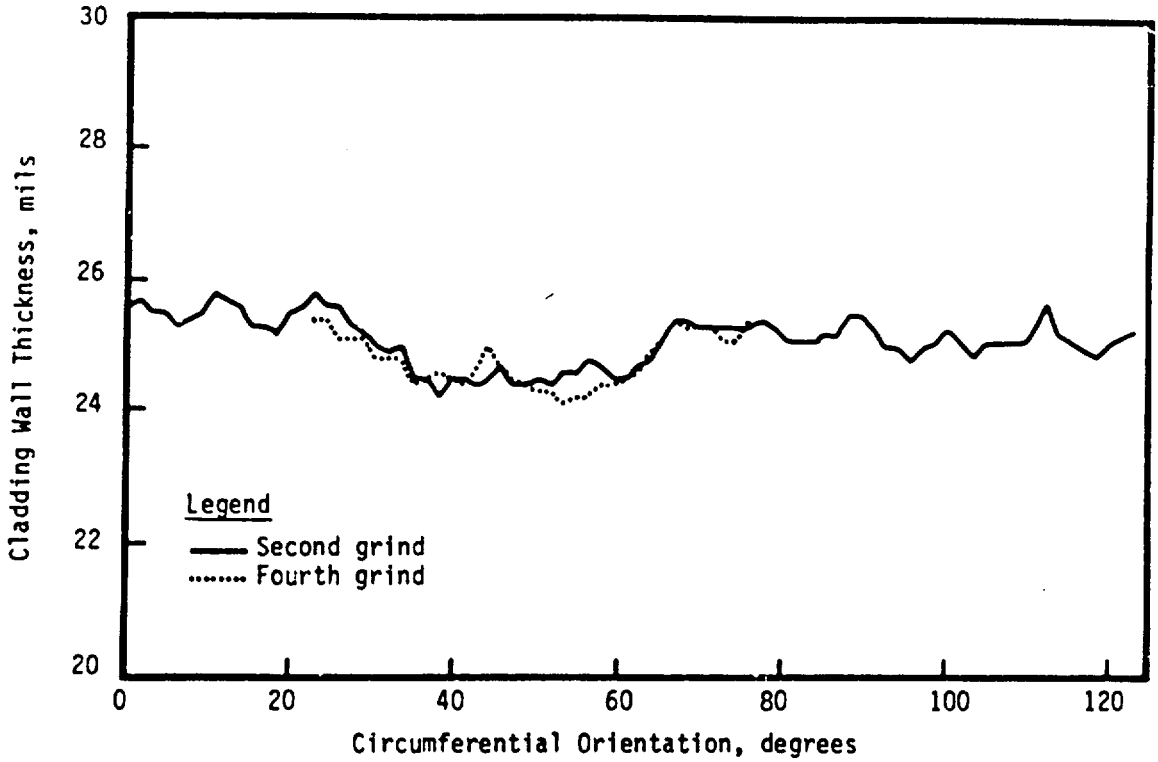

Figure 4-41. Poolside View of Bowed Rods on Face D of Assembly 1D45

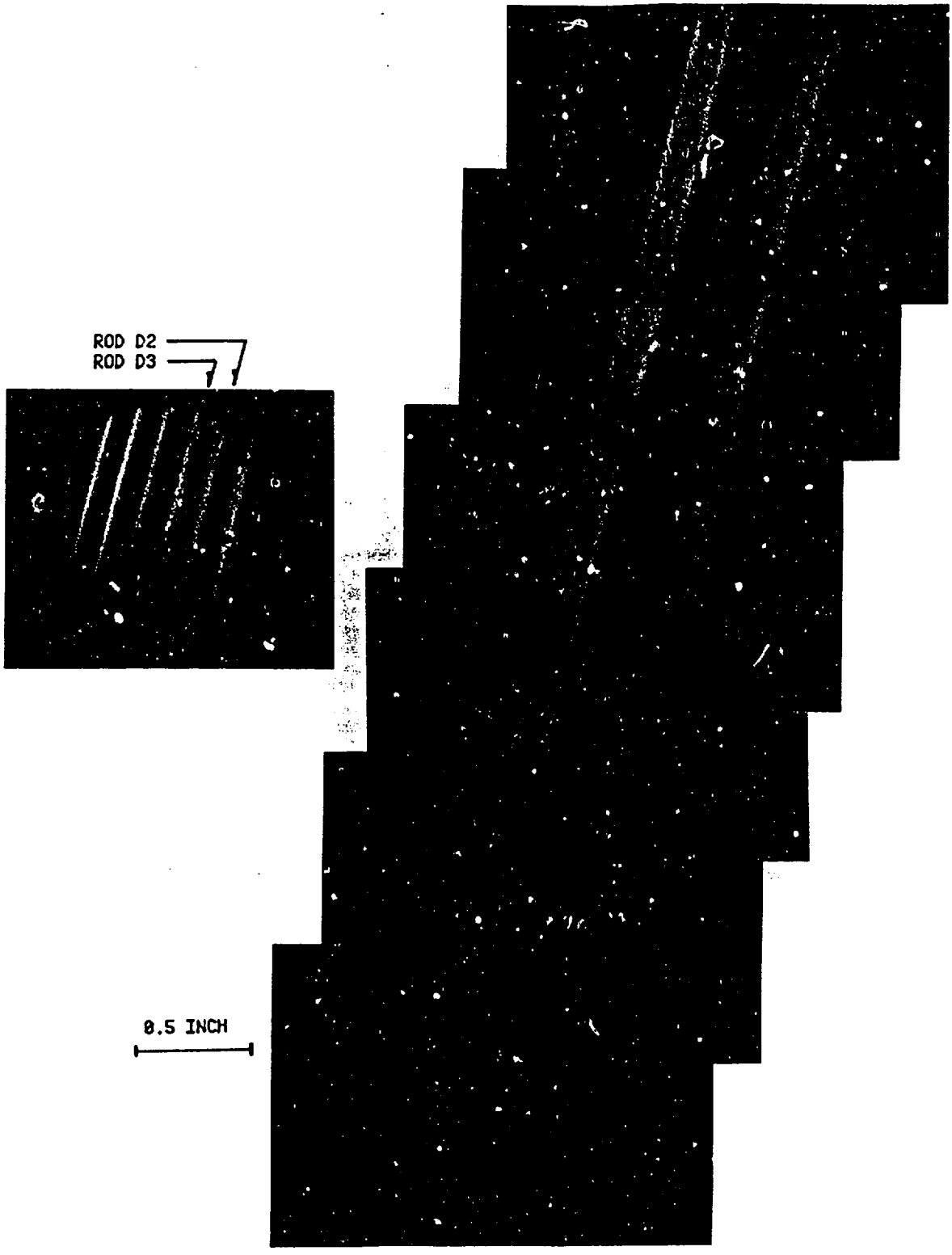

A transverse section of this region was examined metallographically to characterize the condition of the fuel and cladding wall.

Since the rods were operating with reduced coolant flow in this region for up to two reactor cycles, there was concern that additional changes in the fuel microstructure might have occurred. Microscopic examination, however, showed no difference in fuel microstructure in or away from the bowed region of the sample cross section.

Micrographs of the cladding in the bowed region are shown in the polished and etched condition in Figure 4-42. Thicker oxide and uniform loss of wall are clearly seen in the figure. Maximum oxide thickness in the near-contact region was about 125μ, while the base oxide was about 25 to 30μ at that axial elevation. Although cladding hydrides are not as prevalent at this axial position, the area under the thicker oxide had fewer hydride platelets than adjacent regions of the sample cross section. This indicates that local cladding temperatures in the thicker oxide region were higher than in the adjacent regions. Plots of oxide thickness and wall thickness measured from Figure 4-42 are shown as a function of circumferential position in Figure 4-43. The thicker oxide covers approximately 50 degrees of the circumference and is associated with a decrease in cladding wall thickness of up to 2 mils.

4.11.5. SEM Characterization of the Cladding Surface

The waterside corrosion film on three samples was characterized by scanning electron microscopy (SEM) at magnifications up to 20000X. One of the samples was from the area on rod 15192 that was bowed to near contact with an adjacent rod during the last two cycles of irradiation. The other two samples were from the thicker oxide regions (span 2) of rods 15189 and 15309. In addition, the ID surfaces of the samples above from rods 15192 and 15309 were also examined.

The samples consisted of small sections of defueled cladding that were cleaned in an ultrasonic bath to remove loose crud and oxide particles. They were rinsed in deionized water, then alcohol, and dried. Their surfaces were coated with gold to produce high-quality SEM images.

The maximum oxide film thickness at the near-contact region of rod 15192 had been measured (both destructively and nondestructively) to be about 125μ. A

Figure 4-42. Micrographs of Transverse Section Through Bowed Region on Rod 15192

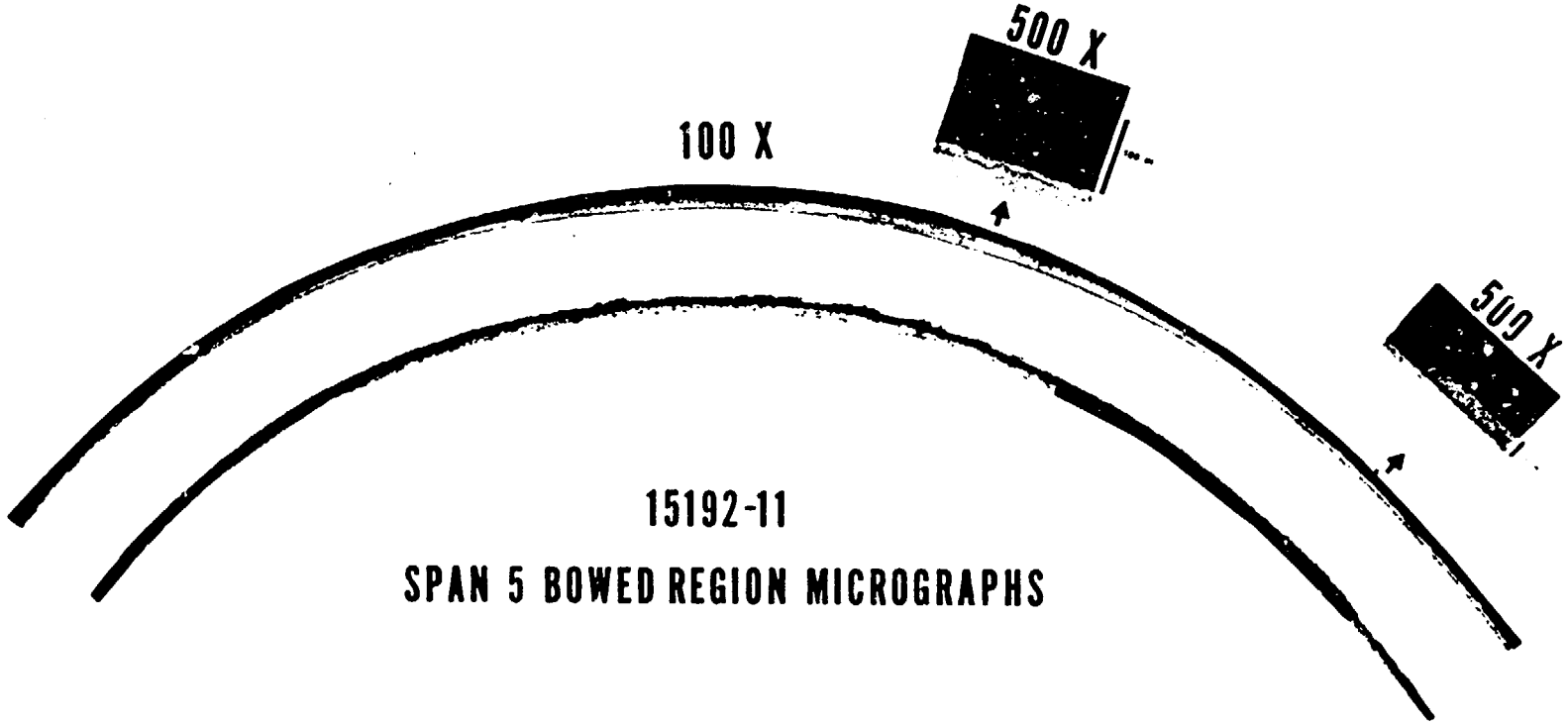

Figure 4-43. Circumferential Profiles of Oxide Thickness and Wall Thickness in the Bowed Region of Rod 15192

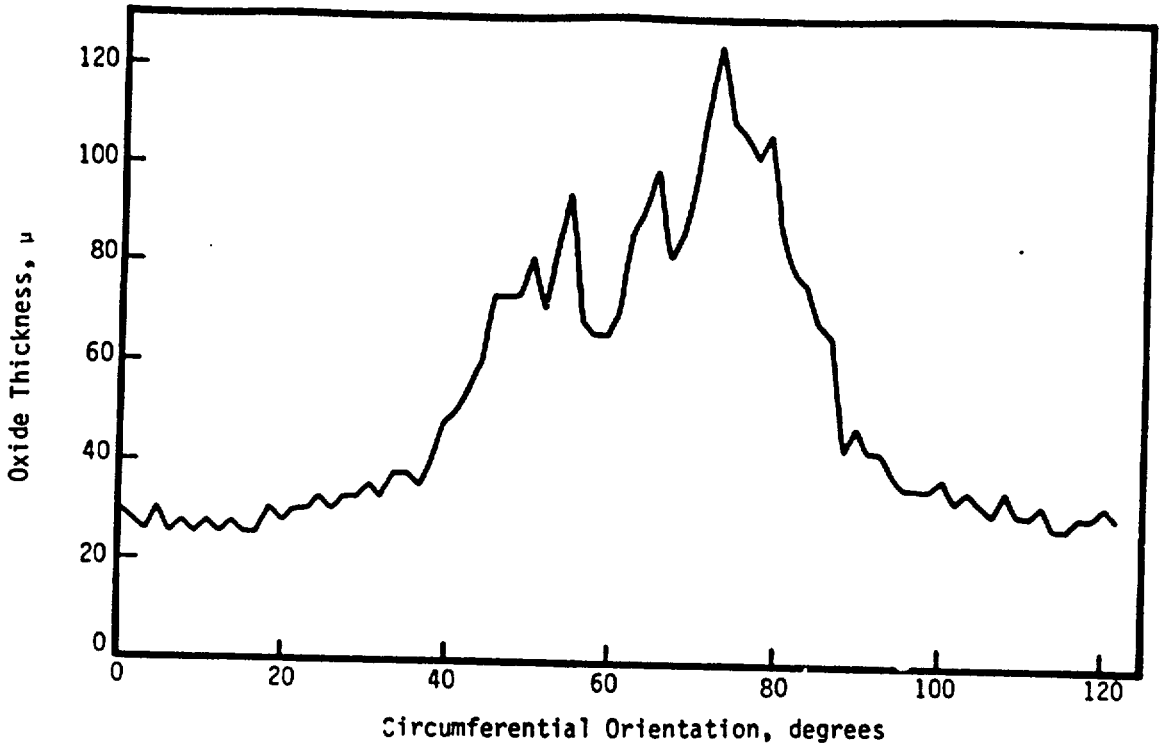

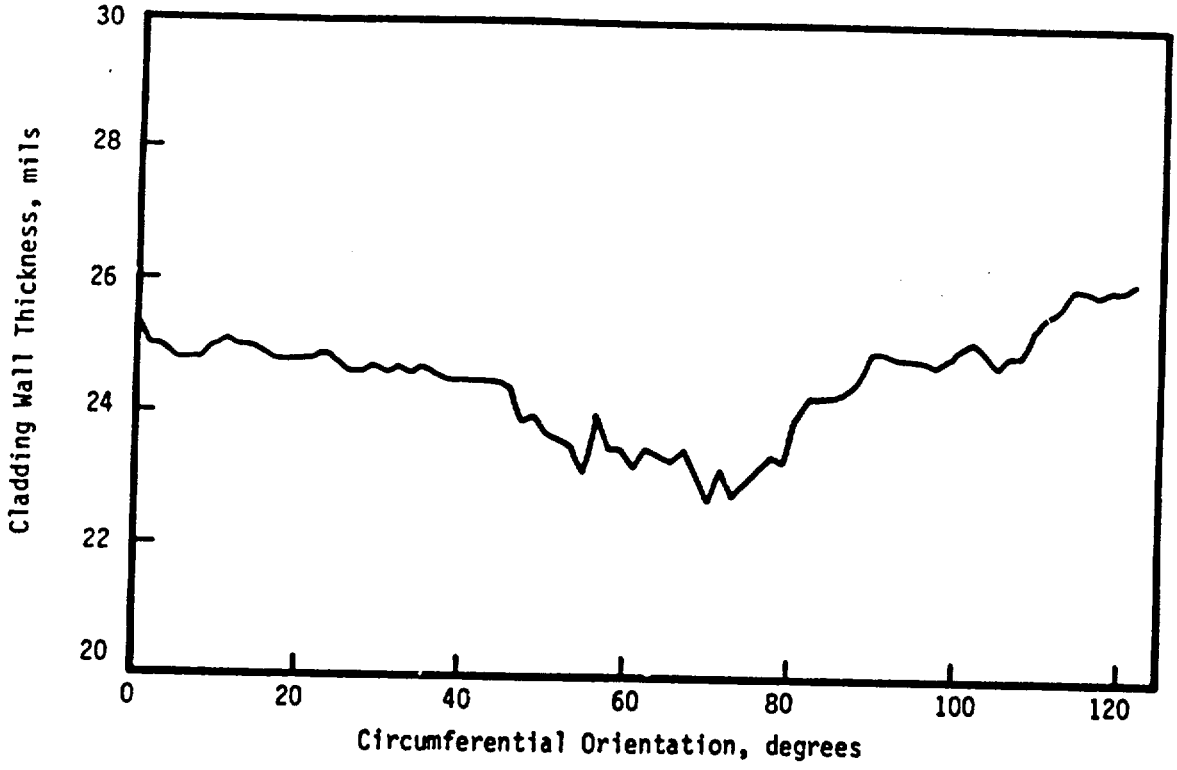

low magnification micrograph of this region (sample 15192-11) is shown in Figure 4-44 and can be seen to contain a longitudinal series of craters of spalled oxide along the line of contact (water channel closure) between the two bowed rods. This line is in the middle of a stained area of thicker oxide resulting from degraded heat transfer due to closure of the water channel. A very thin layer of that oxide appears to have spalled off most of the stained area, although the original grinding scratches from the tube fabrication are still visible.

Note that the first oxide layer to form on the cladding is present at the water-oxide interface, i.e. the OD surface, unless it has spalled off. The layer adjacent to the metal-oxide interface is the most recently formed oxide.

Figure 4-45 shows a prominent spalled crater about 0.1 inch in diameter and 40 to 50μ in depth. Typical fracture surface micrographs of the crater, its wall, and rim areas are shown in Figure 4-45. The crater wall has a clearly layered or laminar structure with many circumferential cracks between the layers of oxide. The OD oxide surface adjacent to the crater region showed a structure consisting of clusters of small granules (about 0.05 to 0.5μ) with a "cauliflower" appearance as shown in Figure 4-46. A transverse section from this region was metallographically polished and examined on the SEM. Electron images of that transverse section are shown at two magnifications in Figure 4-47. The primary feature within the oxide layer is the high concentration of short circumferential fissures or microcracks, occasionally interlinked to form a continuous longer crack. The fissures appear to be fairly uniformly distributed across the thickness of the oxide layer from the oxide-metal interface to the water-oxide surface. These microcracks are believed to form in the oxide to relieve the compressive stresses that develop during oxidation. The stresses form as a result of the volume increase upon conversion of the metal to its oxide.

The span 2 region of rod 15189 (sample 15189-5) exhibited an average oxide thickness of about 45μ. A typical micrograph of the oxide surface is shown in Figure 4-48 with the original circumferential grinding marks from the cladding fabrication process. The axial scratch seen in this figure resulted from post-irradiation handling of the fuel rod. At high magnifications, the

Figure 4-44. Cladding Waterside Surface in the Near-Contact Region

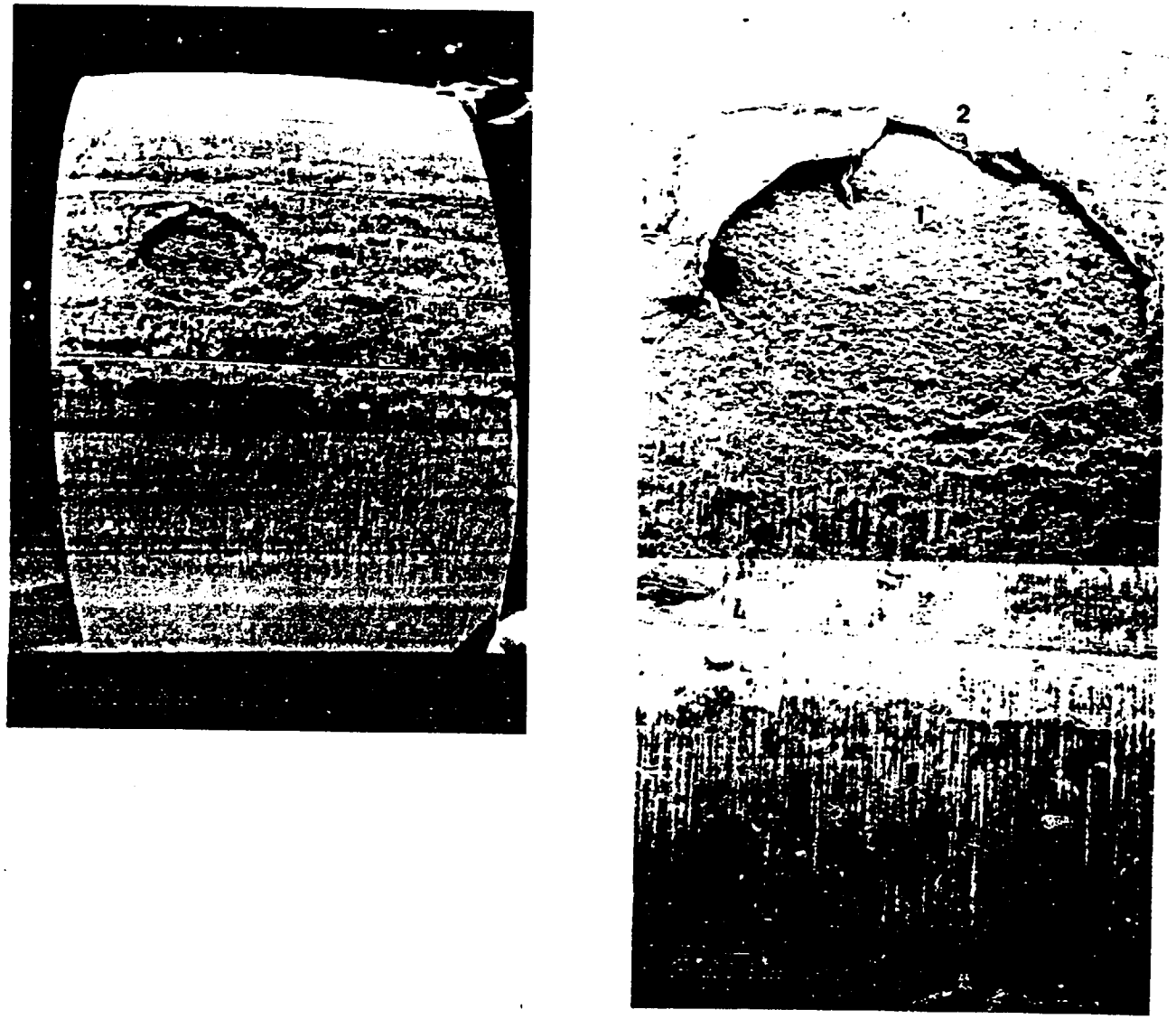

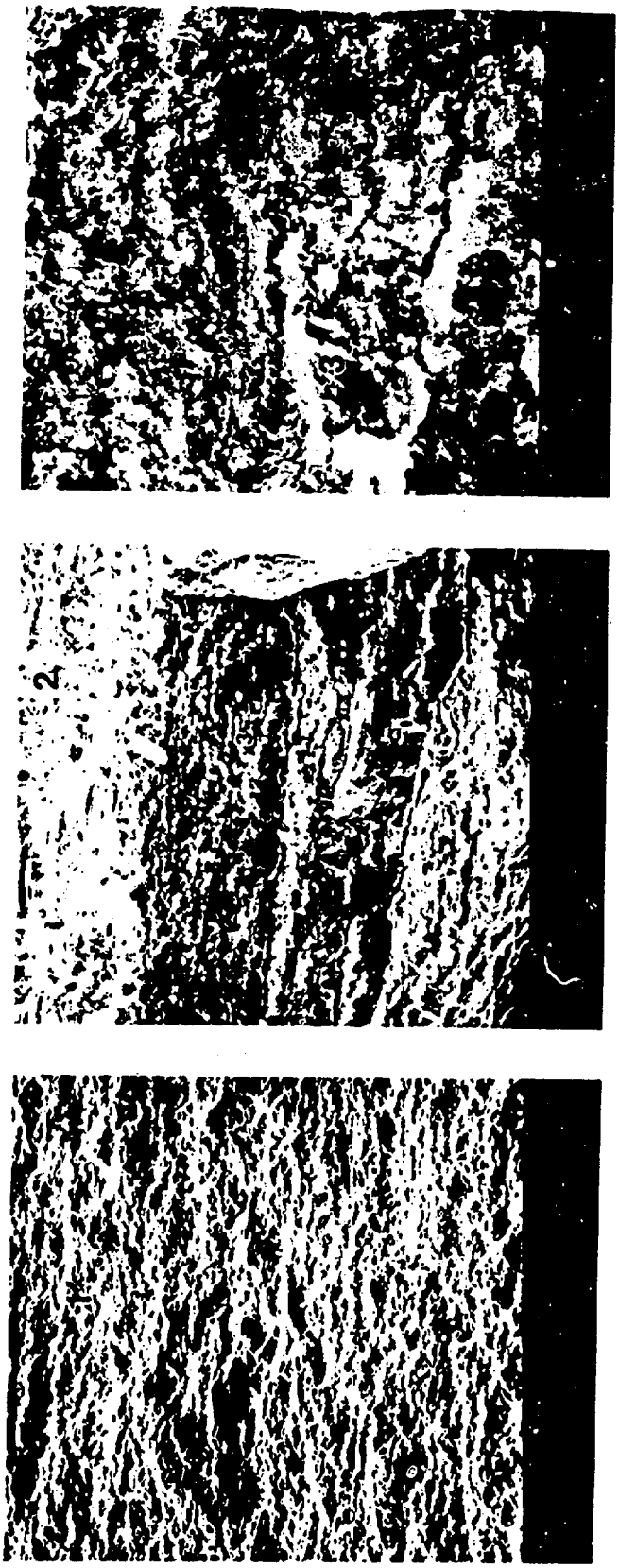

Figure 4-45. Fracture Surface Features of an Oxide Crater

Figure 4-46. Oxide Surface Features Adjacent to an Oxide Crater

Figure 4-47. Transverse Section Showing Circumferential Microcracks

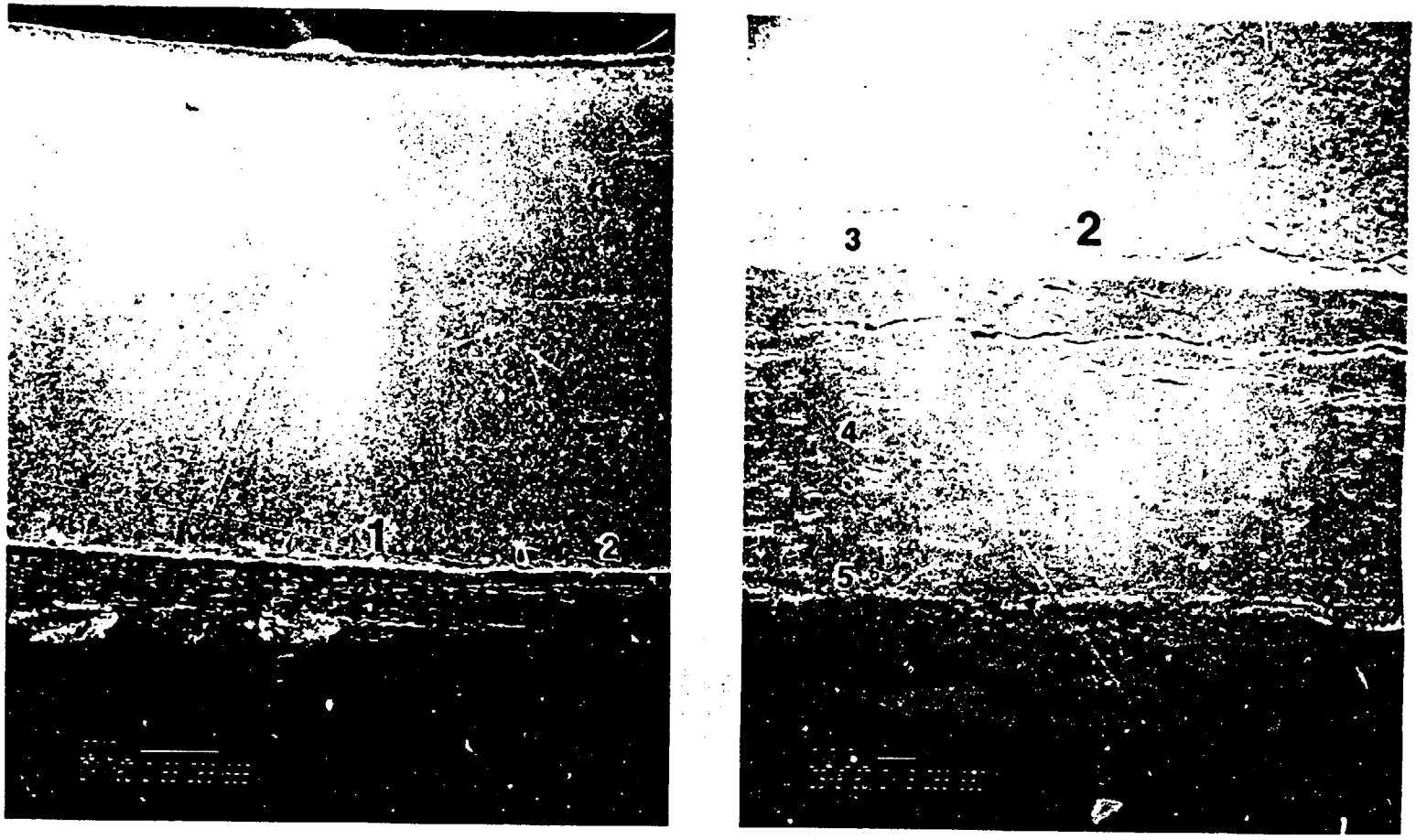

Figure 4-48. A Typical Uniform Oxide Layer

oxide surface morphology of sample 15189-5 can be seen to be different from that of sample 15192-11. The oxide on the latter had the granular cluster or "cauliflower" structure described above. The oxide on sample 15189-5 had a smoother texture with evidence of small platelets of 0.2 to 0.5μ in diameter as shown in Figure 4-49, which shows higher magnification images of an area within the scratch depicted in Figure 4-48.

The span 2 region on rod 15309 had an average oxide thickness of about 40μ. The OD surface of this area (sample 15309-3A) was similar to that of 15189-5 in its retention of the pre-irradiation, circumferential grinding marks. However, minor spallation was also observed in this span 2 region as shown in Figure 4-50. At high magnification, Figure 4-51 shows that the unspalled surface areas of this sample had an oxide morphology with the same platelet structure mentioned earlier. However, in Figure 4-52, a spalled area from the same sample shows the granular, "cauliflower" structure similar to that from sample 15192-11.

On the basis of observations from both span 2 samples, the platelet structure of the oxide appears to be formed near the original cladding surface (the oxide-water interface) during early-life oxidation, possibly corresponding to pre-transition oxidation kinetics. The granular or "cauliflower" structure seems to develop later, during a series of successive stages, under post-transition kinetics. However, the platelet structure was not observed in the near-contact sample 15192-11. The reason could be that a very thin surface layer of the oxide had already spalled off the entire area that was examined. Note that the granular cluster or "cauliflower" structure of the oxide has been reported in References 35 and 36, but the platelet structure of the near-surface oxide observed in this investigation was not expected.

Other explanations for the near-surface platelet structure might include the possibilities that the platelets consist of adherent crud particles, or that they are a result of iron and chromium enrichment near the water-oxide interface. Such enrichment has been reported in References 35 and 36. Note that chromium- and iron-rich second-phase particles are normally present in Zircaloy-4. Such particles were not observed in this investigation and were rarely seen in earlier, more extensive work. Therefore, iron and chromium are expected to be in solution in the bulk of the oxide, although the samples in this examination were not analyzed for these elements.

Figure 4-49. Features of a Typical Uniform Oxide Layer

Figure 4-50. Minor Spallation in a Uniform Oxide Layer

Figure 4-51. Features of a Uniform (Not Spalled) Oxide Layer

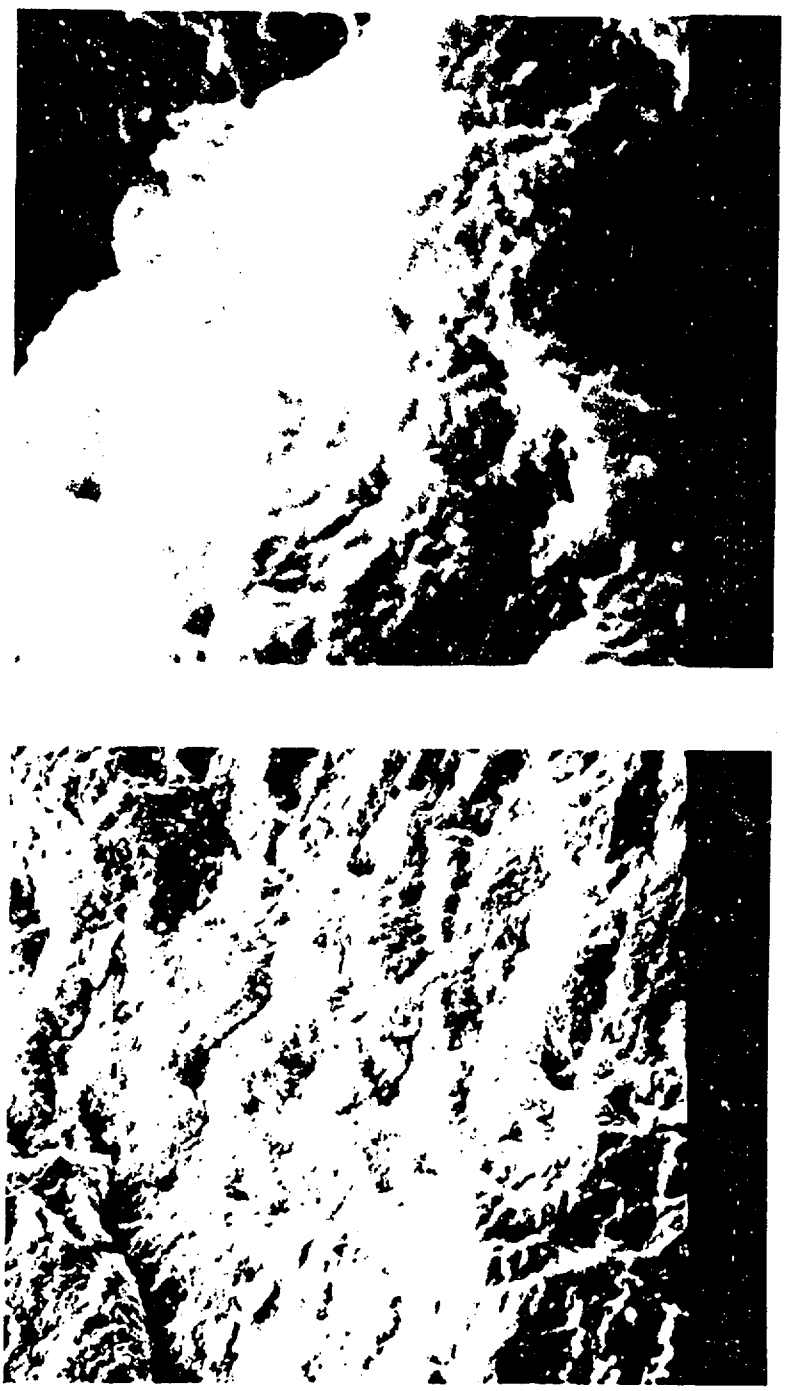

Figure 4-52. Features of a Spalled Oxide Area

The ID surfaces of cladding samples 15192-11 and 15189-5 were also examined by SEM. Neither sample showed evidence of incipient defects or cracks. A thin oxide layer ranging from 10 to 15μ in thickness was observed on the ID surfaces. The oxidized surfaces were generally smooth, but contained numerous islands of fuel-cladding reaction products that were diffusion bonded to the surface. Typical areas are shown in Figures 4-53 through 4-56.

These micrographs show the porous fuel fragments adhering to the surface of the cladding. The fuel fragments correspond to the porous fuel layer on the outer surface of the pellets discussed in section 4.7. The area surrounding a fuel fragment consists of a denser oxide layer that forms a rippled surface on the cladding ID.

A transverse section from sample 15192-11 was cut through an island of bonded fuel-cladding reaction product and was polished metallographically. Figure 4-57 shows the cross section of the fuel fragment and the surrounding denser oxide layer, including a backscatter electron image. Under backscatter imaging conditions, the higher atomic number material appears brighter due to the more efficient interaction of heavier atoms with the electron beam. The material in the porous deposit has the highest average atomic number, Z, and is diffusion bonded to a layer with a lower average Z value. The metallic substrate, Zircaloy-4, appears as an intermediate gray corresponding to an intermediate average Z. Thus, the porous deposit is U-rich, and the underlying layer is primarily an oxide of Zircaloy, as confirmed independently with energy dispersive spectrometry (EDS) dot maps for uranium and Zircaloy. However, traces of Zircaloy were seen in the U-rich porous deposit, and traces of uranium were detected in the underlying Zircaloy oxide layer.

4.12. Fuel Examinations

4.12.1. Microstructure

Ten samples from several axial positions were sectioned from the five-cycle rods for optical microscopic examination. Nine of the samples were transverse sections, the other was a longitudinal cross section that included mid-pellet and pellet-to-pellet interface locations. Four of the transverse samples were also examined with an SEM. Microstructural characterization of the fuel was performed as to determine the following:

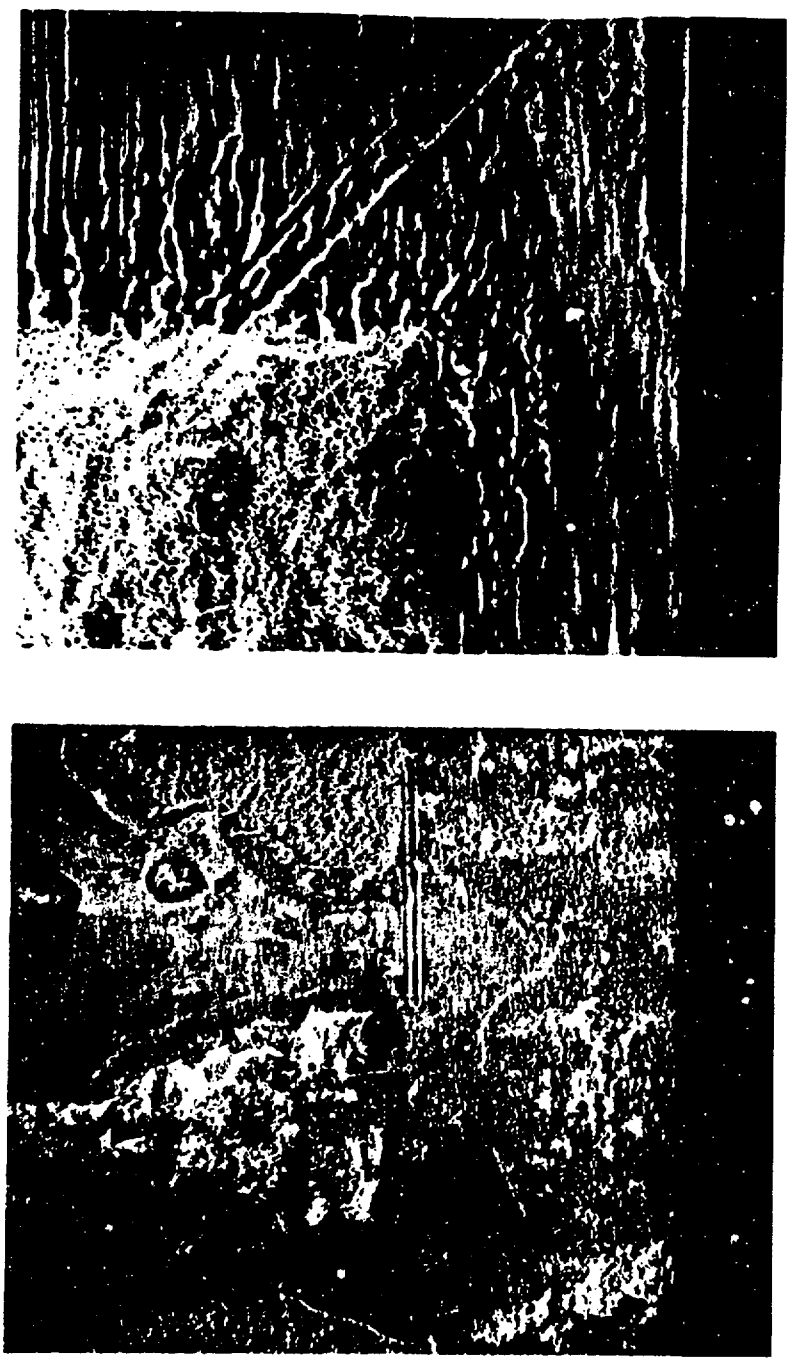

Figure 4-53. Fuel Fragment Bonded to Cladding ID Surface

Figure 4-54. Dense Layer in a Fuel-Cladding Bond Region

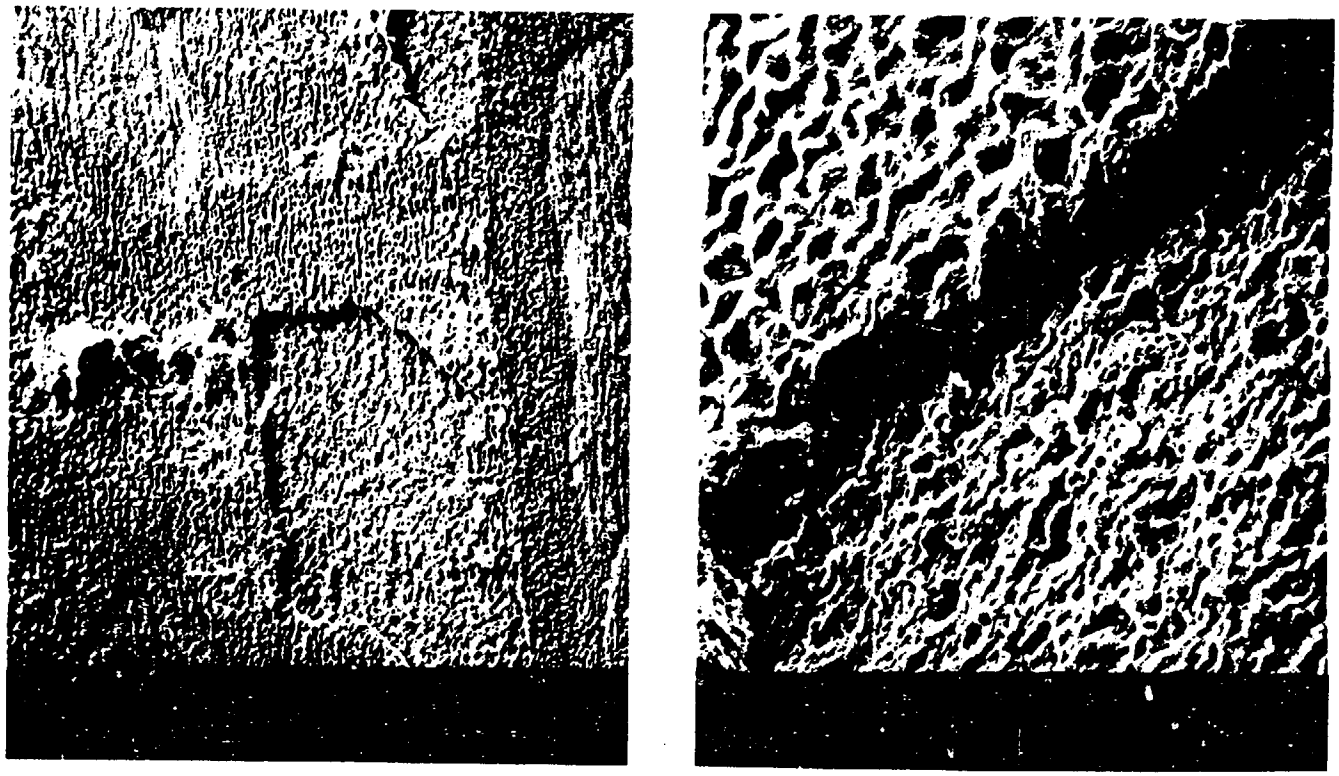

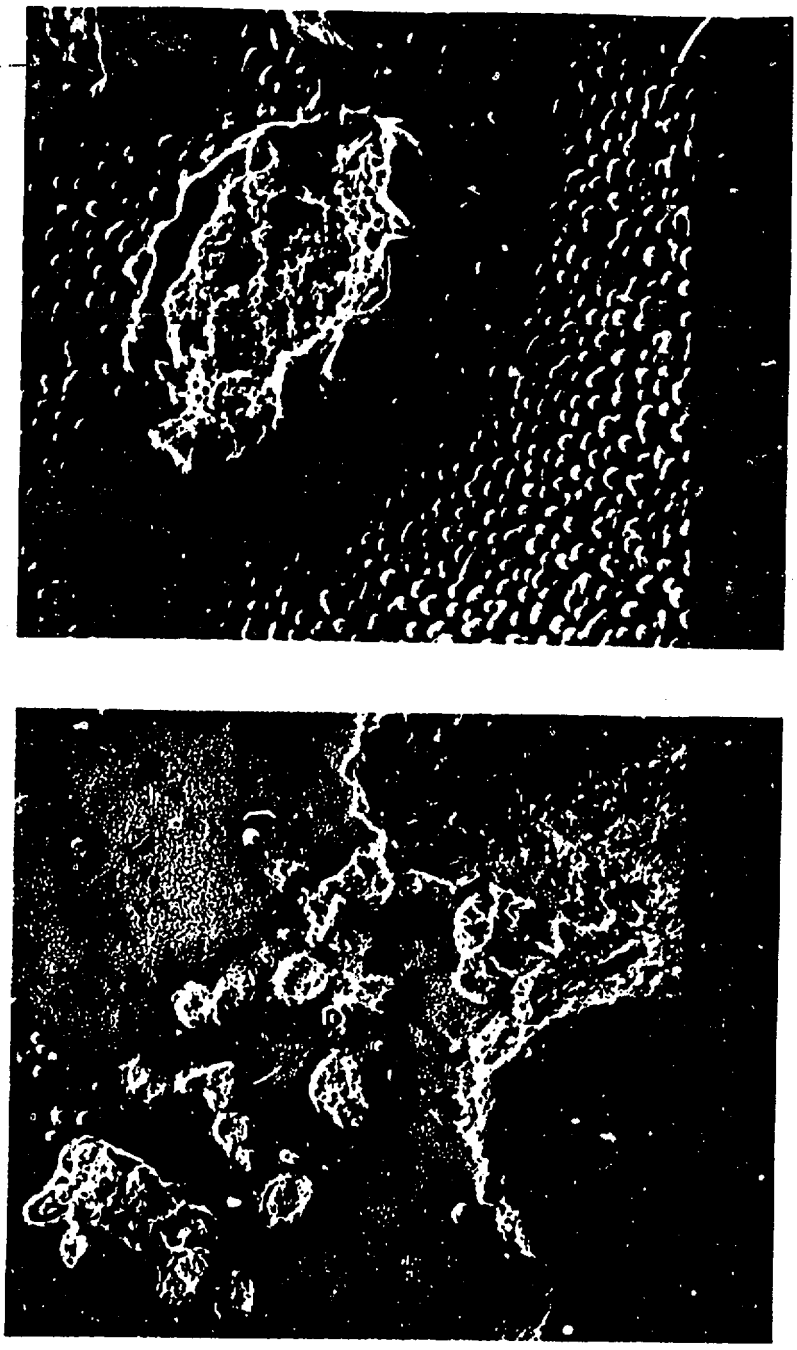

Figure 4-55. Typical Fuel-Cladding Bonding Site

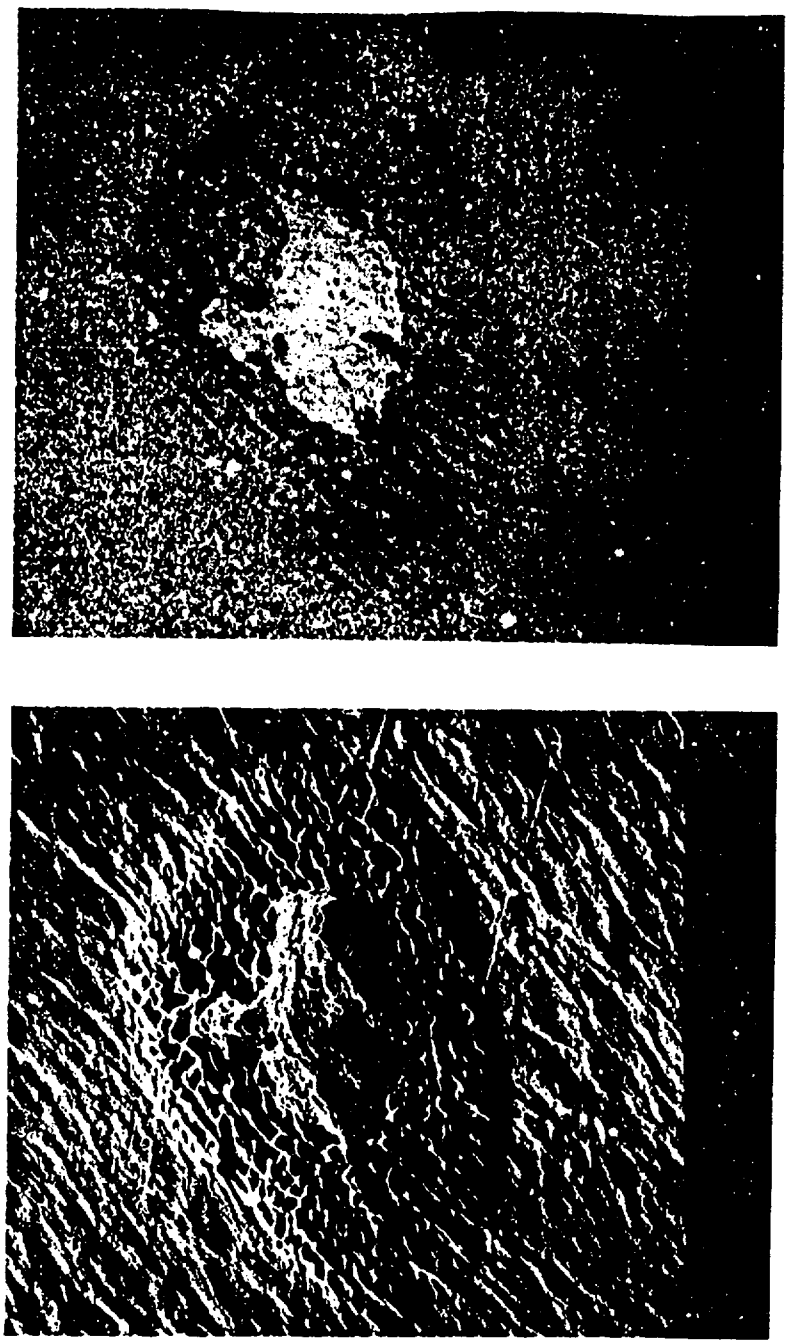

Figure 4-56. Fuel-Cladding Bonding Sites

Figure 4-57. Transversed View of a Fuel Fragment Bonded to a Cladding ID Surface

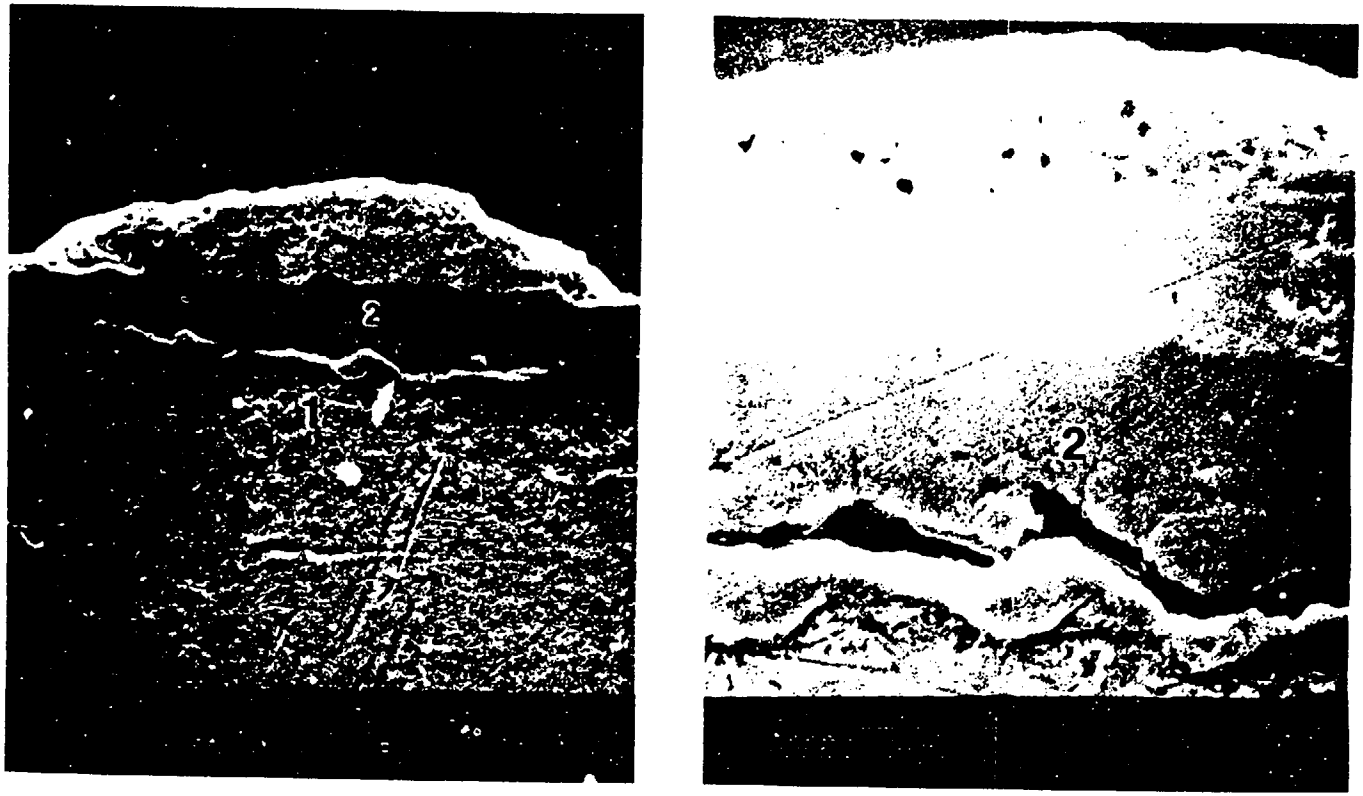

- o Grain size.
- o Porosity.
- o Other phases present.
- o Fuel/cladding reaction layer.

Fuel cross sections were mounted, ground through 6μ on diamond-impregnated grinding wheels, and polished to 1μ with diamond paste. The microstructure was examined at 100 and 500X magnifications in both the as-polished and polished-and-etched conditions. A sulfuric acid-hydrogen peroxide etchant was used to reveal the fuel grain boundaries.

The typical appearance of etched five-cycle fuel samples is shown in Figure 4-58. Two distinct regions are visible in the central portion of the cross sections. These are seen as concentric rings in the transverse section and as bands in the longitudinal section. The inner area corresponds to the region of limited grain growth observed in the microstructure, and the outer area marks the onset of fission gas bubble formation on the grain boundaries.[37]

Typical examples of the center, mid-radius, and edge fuel microstructures are shown in Figure 4-59. The samples shown are from peak burnup regions of the highest and lowest gas release rods sectioned for destructive examination. Measured fuel grain sizes for the 10 five-cycle samples are given in Table 4-22 and a comparison of four- and five-cycle fuel grain sizes is given in Table 4-23. No fuel restructuring was observed in the samples, and only a limited amount of equiaxed grain growth was noted in the central region of the fuel cross sections. The grain size data in Table 4-23 indicate that grain growth occurred in the central region of both four- and five-cycle fuel samples. Since pellet centerline temperatures were low (<750C) during the extended-burnup cycles, this limited growth probably occurred during the first three cycles of normal operation. No strong correlation exists between either average grain growth or grain size and the fission gas release. However, the largest grain growth noted was in a sample from the rod with the highest gas release (rod 15335).

Generally, the center regions of the pellets show a high level of intergranular porosity and a fine dispersion of pores (about 0.5μ) within the grains. As seen in Figure 4-59, a denuded zone exists between the

Figure 4-58. Typical Appearance of Five-Cycle Fuel Cross Sections (Etched Condition)

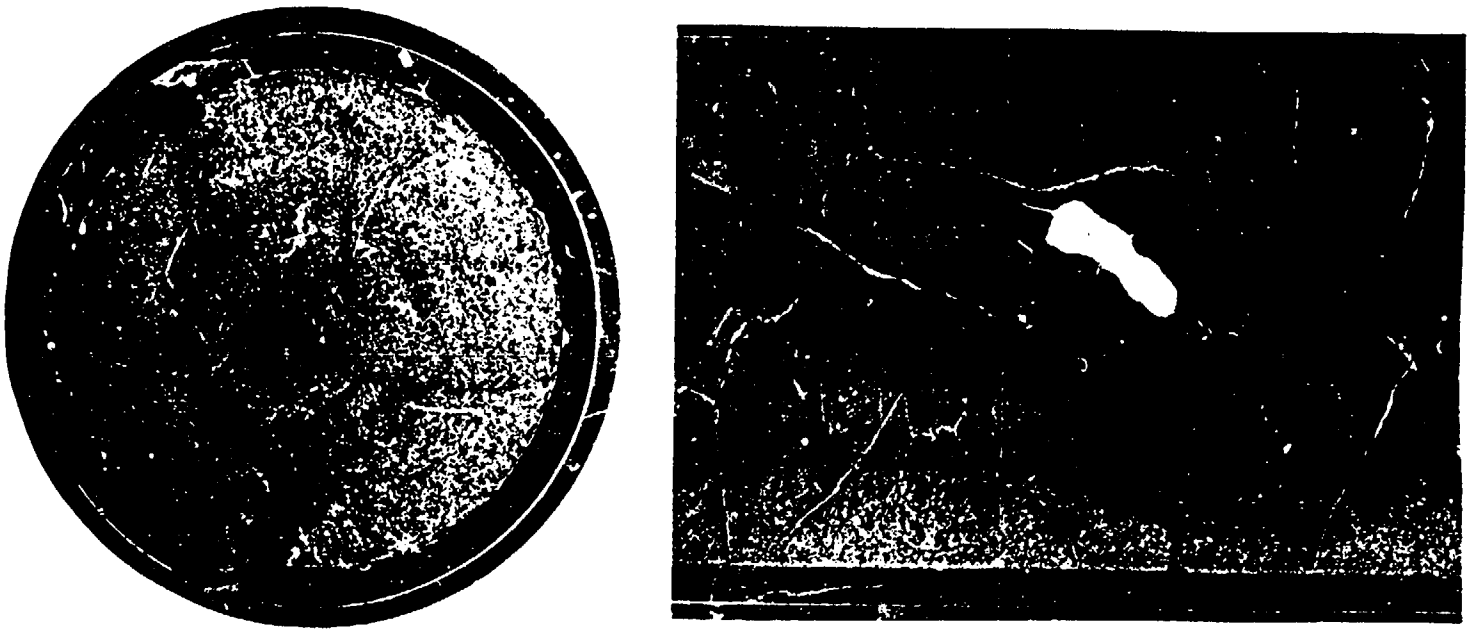

TRANSVERSE

LONGITUDINAL

Figure 4-59. Typical Microstructure of (As-etched) Five-Cycle Fuel Samples

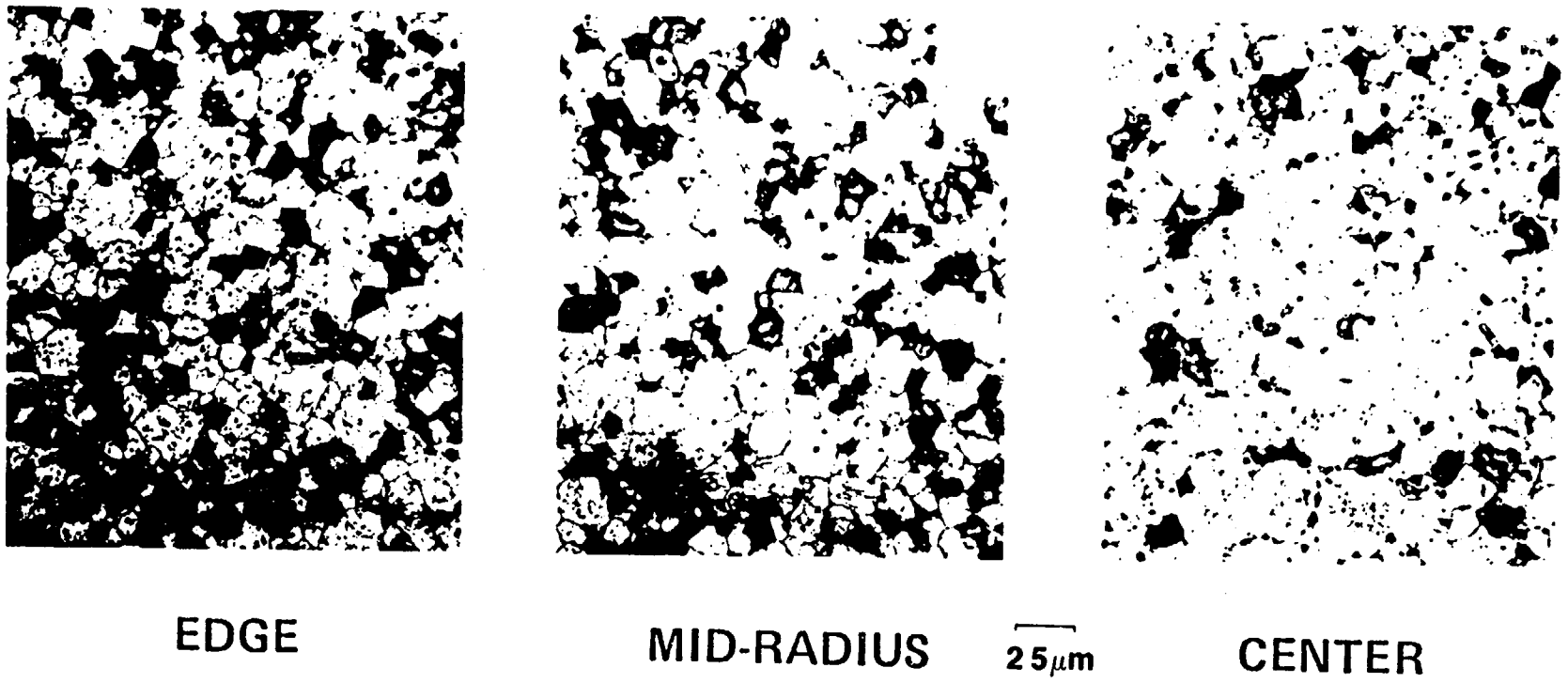

2 OF 2

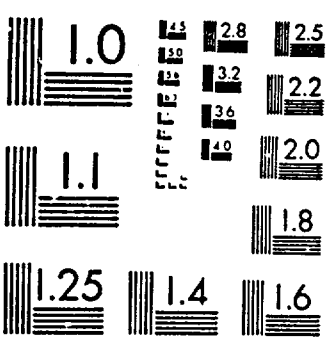

MICROCOPY RESOLUTION TEST CHART
NATIONAL BUREAU OF STANDARDS-1963-A

Table 4-22. Grain Size of Five-Cycle Fuel Samples

Sample No.	Location[a]	Average Grain Size, μ Pellet Cross Section		
		Edge	Mid-radius	Center
15189-15	54.2	10.4	11.2	12.2
15189-6	123.3	11.0	12.5	11.4
15192-11	57.0	11.4	12.7	15.6
15192-4	122.4	10.5	12.8	11.6
15309-21	37.4	9.9	11.4	12.8
15309-14	76.9	9.6	9.8	10.5
15309-7	115.3	11.2	11.0	12.3
15335-13	54.6	12.0	11.1	12.7
15335-5L	123.1 (longitudinal cross section)			
	Pellet-to-pellet interface	10.6	11.2	13.7
	Mid-pellet	10.3	12.3	14.1
15335-5	123.6 (transverse cross section)			
		10.6	12.5	16.7

[a]Location is distance from the bottom of the rod.

Note: The first five digits of the sample number correspond to the fuel rod number.

Table 4-23. Average Grain Size of Four- and Five-Cycle Fuel

	Pellet Cross Section, μ		
	Edge	Mid-Radius	Center
Five-cycle average	10.7	11.8	12.9
Range	9.5-12.0	9.8-12.8	10.5-16 7
Four-cycle average	12.4	12.8	13.9
Range	10.3-14.4	10.7-15.0	12.5-15.2
As-fabricated nominal		10.8	

intragranular porosity and the grain boundaries in the pellet center. Metallic inclusions (0.5 to 2μ in size) were observed only in the pellet center region, and appeared most frequently in the intergranular pores.

The pellet mid-radius region had less inter- and intragranular porosity than the center. Its intragranular pores were coarser, and there were no denuded zones noted within the fuel grains. In the etched condition, small ribbon-like features, <0.1μ in length, were seen in the grains. These may be fission products or coalesced groups of very fine pores; they were not seen in the as-polished micrographs.

The pellet edge region had very little inter- or intragranular porosity, and more of the ribbon-like features were visible in the etched condition. Grain pull-out after etching was most severe at the pellet edges. A reaction zone, shown in Figure 4-60, was frequently observed at the pellet-cladding interface of the samples. This was not seen in samples after three cycles, and was seen only infrequently in four-cycle samples. The zone consisted of two layers: a thin, dense layer next to the cladding, and a porous region at the outer edge of the fuel.

A thin layer of fuel was removed from four of the mounted cross sections and examined in the SEM. Results of the SEM examination were consistent with ceramographic observations, and provided additional information on fuel porosity. Figure 4-61 shows fuel grains from the center of a sample from the higher gas release rod (15335). A fractured grain in the left of the figure clearly shows the fine intragranular porosity and the denuded zone adjacent to the grain boundaries. Grains in the far right of the figure show extensive porosity on the grain faces. The small nodules seen in the grain face pores are the metallic inclusions that were only observed in the center portion of the fuel cross sections. These are most likely insoluble metal fission products such as molybdenum that tend to diffuse up the thermal gradient.

The mid-radius region (Figure 4-62) showed less porosity on the grain faces, and the pore size was smaller than in the center region of the pellets. The mid-radius region also contained scattered areas of linear arrays of pores. Examples of these arrays are shown in Figure 4-63. These linear arrays may represent the first stages of bubble interlinkage, which results in increased

Figure 4-60. Ceramographic Appearance of the Fuel-Cladding Reaction Layer

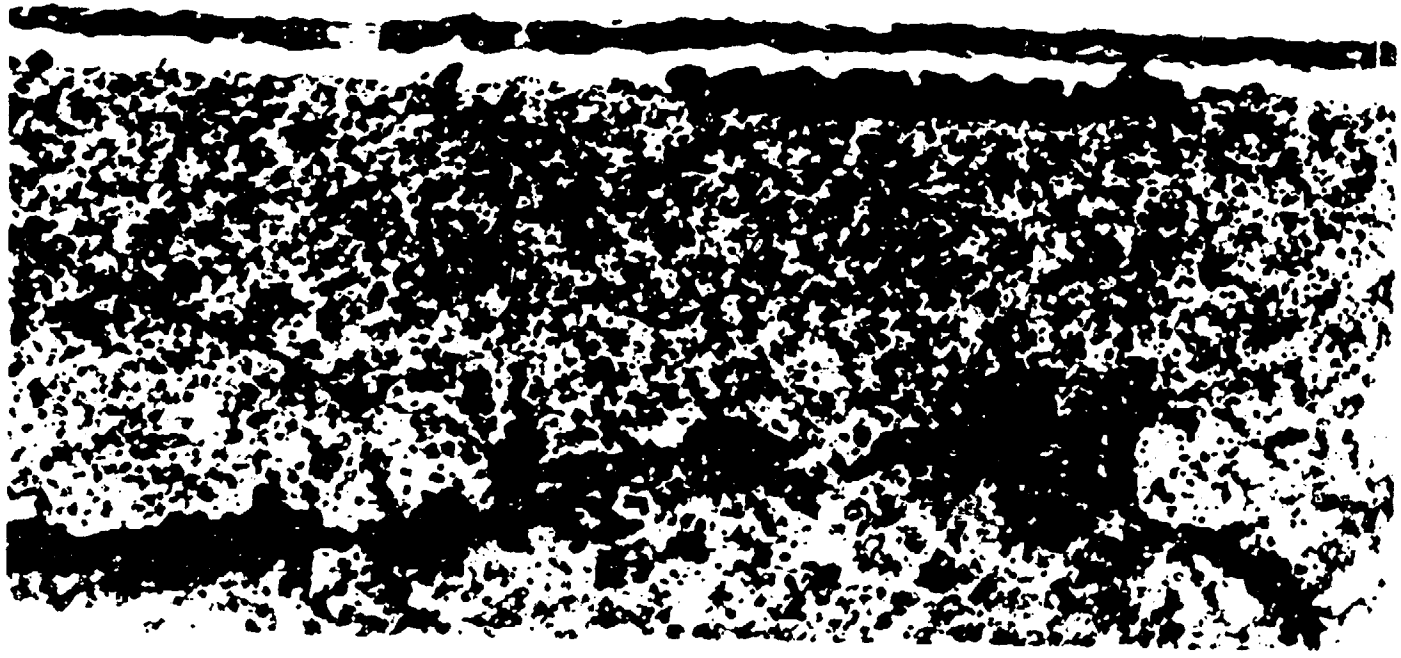

Figure 4-61. Typical SEM Views of the Center Region of Five-Cycle Fuel Cross Sections

Figure 4-62. SEM Photographs of the Mid-Radius Region of Five-Cycle Fuel Cross Sections

Figure 4-63. Linear Arrays of Pores Observed in the Mid-Radius Region of Five-Cycle Fuel

fission gas release. The pellet edge region (Figure 4-64) had pores at triple points, but only a few small pores on the edges or faces of the grains.

Nearly all pellet cross sections had a reaction layer at the pellet-cladding interface. An example of the appearance of this layer in the SEM is shown in Figure 4-65. The thin, dense layer (about 5μ thick) appears as a dark, vertical band at the left of the micrograph. The porous region (about 20μ thick) is clearly a different structure than the fuel seen in the right of the figure. Backscatter images showed that the dense layer was darker than the fuel, indicating that it is composed of elements with lower atomic numbers (Z) than the fuel or has a lower average Z value. The porous region appeared with the same brightness in backscatter as the fuel. X-ray dot maps indicate that the thin, dense region is mostly zirconium, with possibly a very small amount of uranium. The porous region was primarily uranium, but also contained zirconium. Since the dense layer is mainly zirconium, but is darker (lower average Z) than the cladding, the layer is most likely zirconium oxide. The porous layer next to the fuel is probably composed of a urania-zirconium reaction product that is denser than the fuel, but has a greater residual porosity due to shrinkage of the fuel matrix.

4.12.2. Density

Immersion density measurements were obtained on 12 samples of the five-cycle fuel. Samples were taken primarily from high-burnup regions of the four sectioned rods; one sample was taken from near the top of the fuel column. Each sample consisted of a random mixture of pellet pieces from about five pellets. The average weight of each set of pellet pieces ranged from 15 to 30 grams. Dry and suspended weights were measured remotely using a digital electronic balance having an accuracy of 0.1 mg.

Results of the fuel density measurements after five cycles are given in Table 4-24 and shown as a function of axial position in Figure 4-66. On the average, fuel density had decreased about 1.46% from the initial pre-irradiation level of 95.79% of theoretical density. The observed changes in fuel density for samples of fuel in this program are summarized in Table 4-25. After three cycles, fuel swelling had fully compensated for initial densification. After four cycles, net swelling was about 0.8%. The 0.6% increase in volumetric swelling during the fifth cycle corresponds to the

Figure 4-64. Typical SEM Photographs of the Edge Region of Five-Cycle Fuel Cross Sections

Figure 4-65. Typical SEM Views of the Pellet-Cladding Reaction Layer Observed in Five-Cycle Fuel Samples

Table 4-24. Immersion Density of Five-Cycle Fuel Samples

Sample No.	Location[b]	Average Density[a] grams/cc	% TD[c]
15189-14	56.1	10.305	94.03
15189-12	77.6	10.268	93.69
15189-5	125.2	10.339	94.33
15189-2	144.5	10.430	95.17
15192-12	52.1	10.346	94.39
15192-4	120.5	10.339	94.33
15309-20	39.4	10.338	94.33
15309-13	78.8	10.361	94.53
15309-6	117.3	10.339	94.34
15335-14	52.7	10.351	94.44
15335-11	77.8	10.312	94.09
15335-4	125.4	10.439	95.25
Average		10.347	94.41

(a) Assumes 0.5 volume % open porosity.

(b) Inches from the bottom of the rod.

(c) 100% theoretical density (TD) = 10.96 g/cc.

Note: The first five digits of the sample number correspond to the fuel rod number.

Figure 4-66. Five-Cycle Fuel Density Vs Axial Position

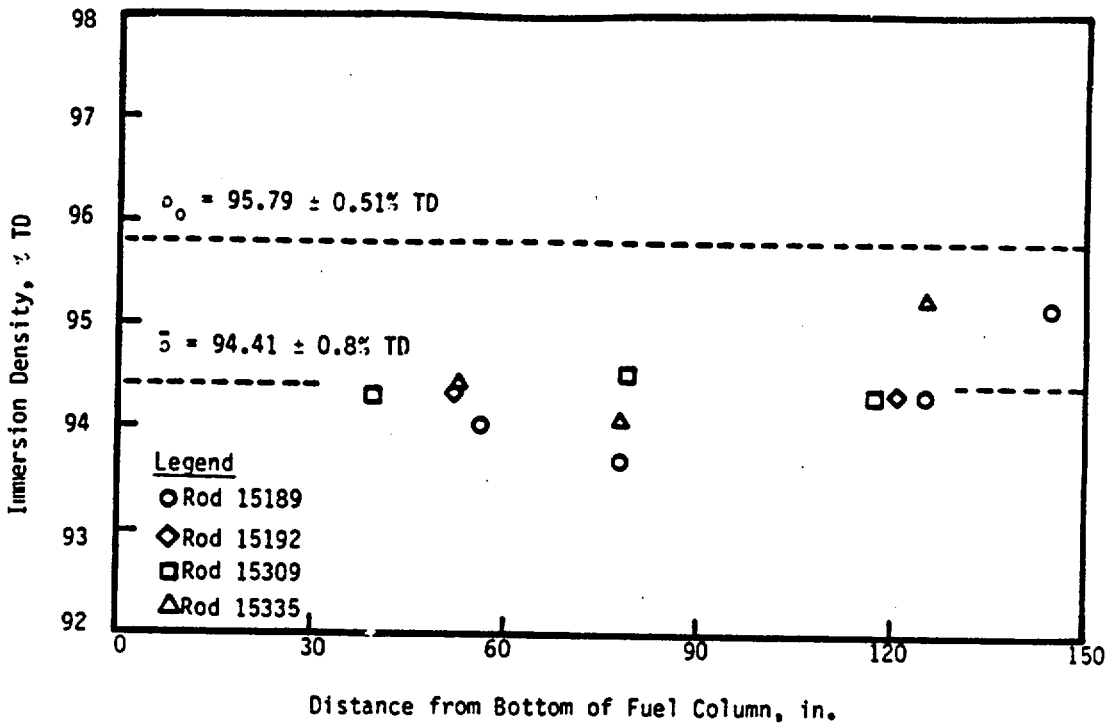

Table 4-25. Density Changes in Oconee 1 Batch 4B Fuel After Three, Four, and Five Cycles of Operation

	Average density, % TD[a]	Pre-irradiation density, % TD[b]	Change, %[c]
Average 5-cycle	94.4	95.8	1.5
4-cycle	94.4	95.2	0.85
3-cycle	96.0	96.0	0

[a] Immersion density

[b] Geometric density

[c] Absolute change in density (not % TD).

0.6% increase in fuel stack length observed during the fifth cycle. This result implies that fuel swelling during the last cycle was primarily in the axial direction. This is in contrast to fuel density and fuel column growth data from previous cycles that indicated that fuel swelling was nearly isotropic. Hard pellet-cladding contact during the fifth cycle may have constrained fuel swelling to the axial direction.

4.12.3. Radial Fission Product Distribution

The radial distributions of gamma-emitting fission products in five-cycle fuel were determined by gamma spectroscopy. Small samples of fuel at six radial positions from each of three mounted pellet cross sections were removed using a carbide drill with a 1-mm bit. Two of the pellet cross sections were from rod axial locations with high burnup and high cladding temperatures. The other was from a region of high burnup but lower cladding temperature. Sample sizes ranged from 2 to 12 mg due to the variability of drilling depth. The microdrill pattern of two pellet cross sections is shown in Figure 4-67. The 18 individual samples of fuel were weighed and gamma counted, and the isotopic activities were determined with peak-search software.

No significant difference was seen in the shape of the radial activity profiles for the three pellet cross sections. The general trend was an essentially constant activity with a slight increase toward the outer pellet edge. This trend is consistent with the irradiation history of the fuel, where burnup was primarily due to plutonium fission during the last two cycles and occurred near the outer edge of the fuel. Two of the samples also had gamma activity peaks at about 0.3 to 0.4 fractional radius, but this is thought to be due to the counting method and not a real peak in the activity profile. Six fission product isotopes accounted for nearly 90% of the total gamma activity of the fuel samples. These were Zr-95, Nb-95, Ru-106, Cs-134, Cs-137, and Ce-144. Also detected in the samples were Sb-125, Eu-154, and the activation product Co-57.

Radial migration of mobile fission products cannot be seen clearly in plots of isotopic activity versus radial position since most of the fuel burnup was occurring near the edge of the pellet during the last two irradiation cycles. Migration can be deduced by plotting the ratio of isotope activity to that of

Figure 4-67. Microdrill Pattern on Five-Cycle Fuel Cross Sections

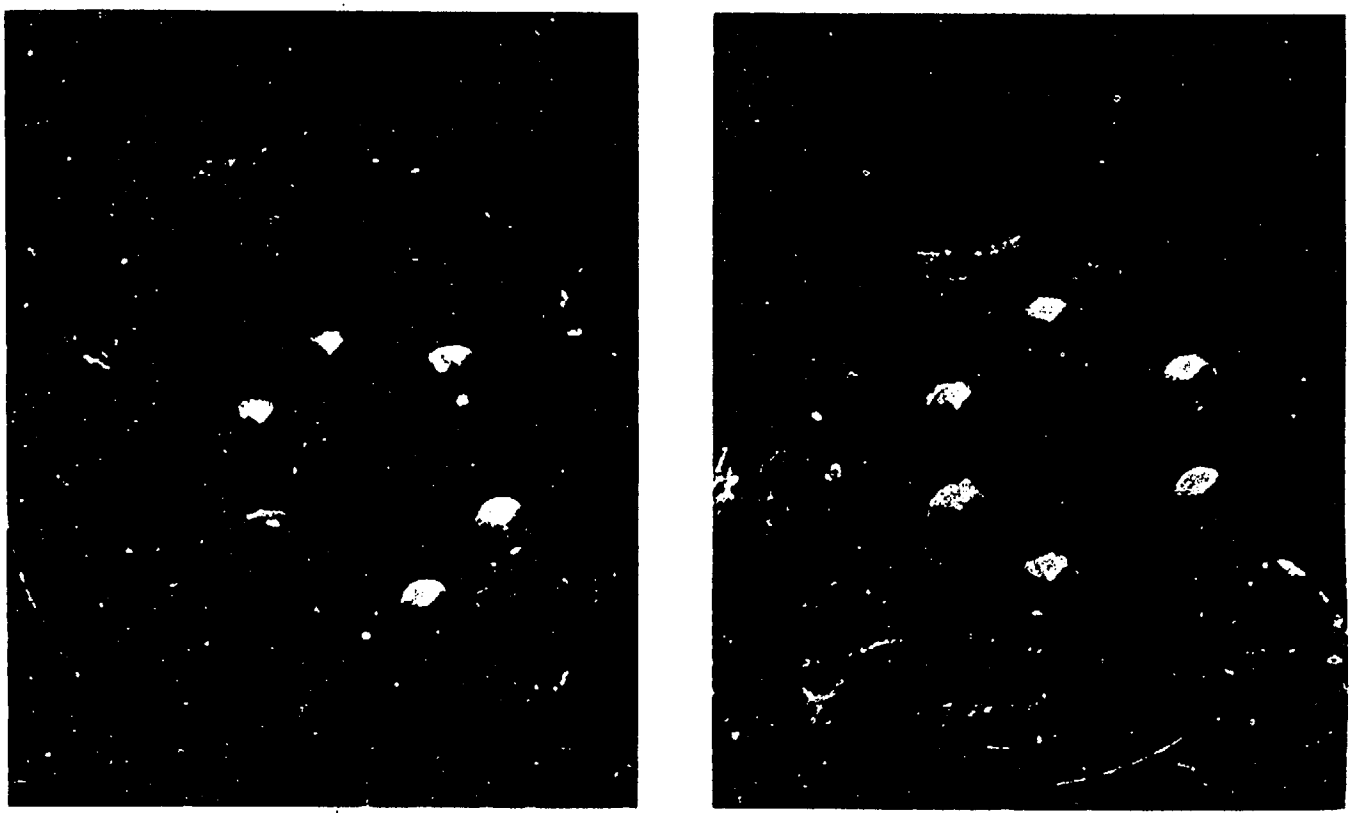

a relatively immobile fission product isotope (such as Ce-144) against radial position. An increase or decrease in the activity ratio of an isotope to that of Ce-144 then corresponds to an enrichment or depletion of that isotope due to migration.

Plots of the activity ratios of Zr-95, Ru-106, and Cs-137 to Ce-144 are shown as a function of radial pellet location in Figure 4-68. Plots for Ru-106 and Cs-137 show a small increase toward the pellet edge, indicating that some migration of these isotopes has occurred. (Although in the case of Ru-106, much of this increased activity near the pellet surface could be attributed to increased fissions of Pu at this burnup level.) A similar increase in activity ratio toward the pellet edge was also observed for Cs-134. Plots of Zr-95 and Sb-125 were essentially constant with radial position, indicating that these isotopes are immobile at the operating conditions experienced by the fuel samples.

4.12.4. Chemical Burnup Analysis

Five fuel samples were chemically analyzed to determine their chemical burnup. Two samples from high-burnup locations were sectioned from three of the five-cycle fuel rods. Each sample was a transverse pellet cross section 0.1 inch thick. The fuel samples were dissolved, and two aliquots of each sample were taken for analysis. One aliquot of each sample was spiked with a known amount of U-233, Pu-244, and Nd-150. The aliquots were separated into fractions containing U, Pu, and Nd, and each fraction was analyzed for isotopic content by mass spectrometry.

Fuel burnup was determined using two methods. The heavy element (HE) method yields fissions per initial atom of uranium from changes in the uranium and plutonium content; the fission product (FP) method is based on the fuel fission product inventory. These methods encompass American Society for Testing and Materials (ASTM) methods E-244, E-267, and E-321. The total heavy element atom percentage of fission was converted to burnup (expressed as GWd/mtU) by using the recommended conversion factor of 9.6 ± 0.3. The estimated uncertainty in measured burnup is about 6%.

Results of the heavy element and fission product burnup measurements of five-cycle fuel samples are given in Table 4-26. Also listed in the table are calculated and predicted burnups for the rods at the sample locations.

Figure 4-68. Radial Migration Profiles of Gamma-Emitting Fission Products in Five-Cycle Fuel

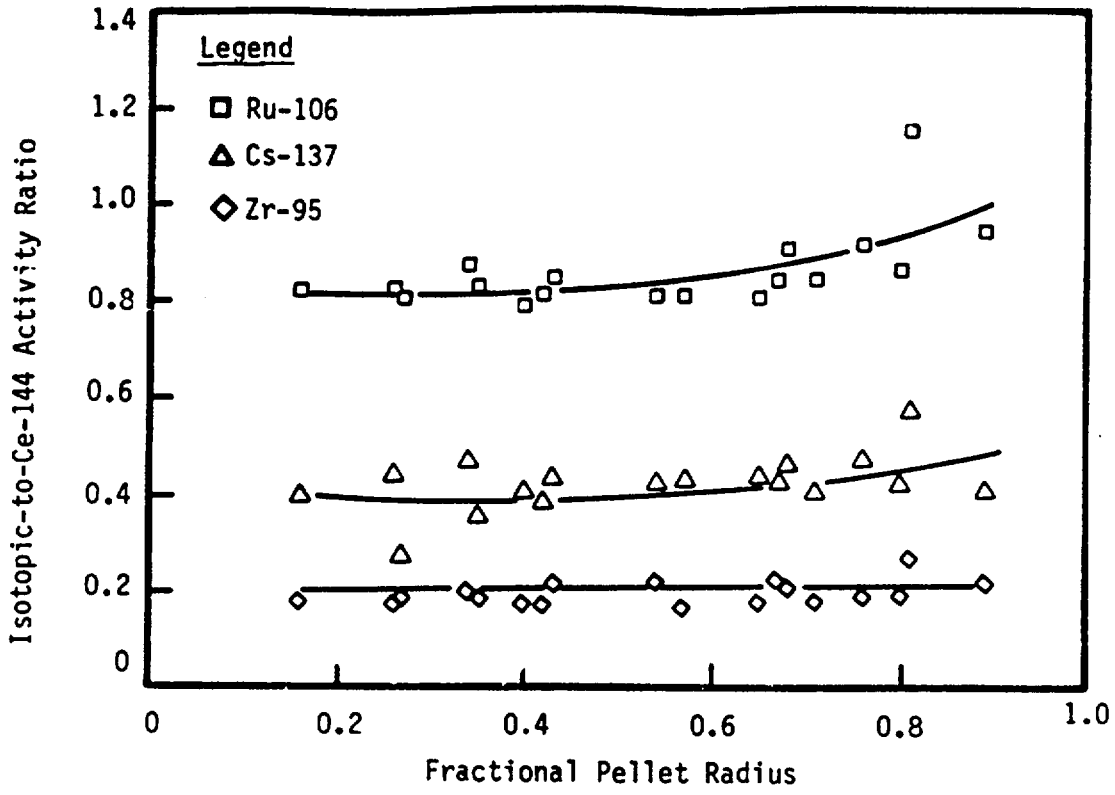

Table 4-26. Chemical Burnup Analysis of Five-Cycle Fuel

Sample No.	Location[a]	Fissions/100 Initial U Atoms		Burnup, GWd/mtU		Predicted[b]	Calculated[c]
		HE	FP	HE	FP		
15189-19	26.1	5.14	5.27	49.4	50.6	52.3	53.2
15189-12	76.6	5.01	5.32	48.1	51.0	53.6	53.6
15309-4	120.2	4.66	5.03	44.8	48.3	51.1	54.7
15335-18	36.4	5.04	4.84	48.4	46.5	50.6	53.2
15335-11	79.6	5.23	5.71	50.2	54.8	54.5	53.8

(a) The sample location is in inches from the bottom of the rod.

(b) Predictions were based on PDQ07 rod-average burnup and the shape of the Cs-137 activity profile of each rod.

(c) Calculations were based on the FLAME3 axial power profile and the PDQ07 average burnup.

Note: The first five digits of the sample number correspond to the fuel rod number.

Calculated values are based on PDQ07 rod-average burnup values and FLAME axial power profiles. The predicted burnups are based on the PDQ07-calculated rod-average burnup and the measured shape of the Cs-137 activity profile for each rod.

Chemically determined burnup values for the five-cycle fuel samples are compared with calculated and predicted burnup values in Figure 4-69. The chemical burnup results are generally lower than calculated or predicted values. Results using the fission product method show closer agreement than those using the heavy element method. The reason for the difference between measured and predicted burnup is not known. Revised chemical burnup data for four-cycle fuel samples (Table 4-27) were over 6% higher than previously reported.[27] The four-cycle data were revised by using normalized capture-to-fission ratios for the uranium and plutonium isotopes. Agreement between the revised four-cycle burnup data and calculated values is within 3%.

4.13. Summary

Sixteen Mark B fuel rods were removed from assembly 1D45 after five cycles of irradiation and underwent hot cell examinations at the B&W Lynchburg Research Center The 16 fuel rods were nondestructively examined, and four were destructively examined. Nondestructive operations included visual examinations, rod length measurements, rod diameter profilometry, fuel column gamma scans, eddy-current oxide thickness measurements, eddy-current (defect) inspection, plenum Kr-85 gamma scans, and fission gas release. The more significant findings from these operations were an acceleration in fuel rod growth and a very low fission gas release. The rod length measurements showed an increased growth rate compared with that of previous cycles. This acceleration in growth is attributed to axial stresses resulting from swelling of the fuel (elongation of the fuel stack) with bonding between the fuel pellets and cladding. This finding is supported by the fuel column gamma scans and the destructive test results. Also, fission gas release was quite low with little increase from the four-cycle results, thus not supporting the NRC-proposed burnup enhancement factor.

The four rods destructively examined were the highest fission gas release rod, two rods with anomalous surface features, and an average (typical of the

Figure 4-69. Comparison of Calculated and Predicted Five-Cycle Axial Burnup Profiles with Chemical Burnup Analysis Results

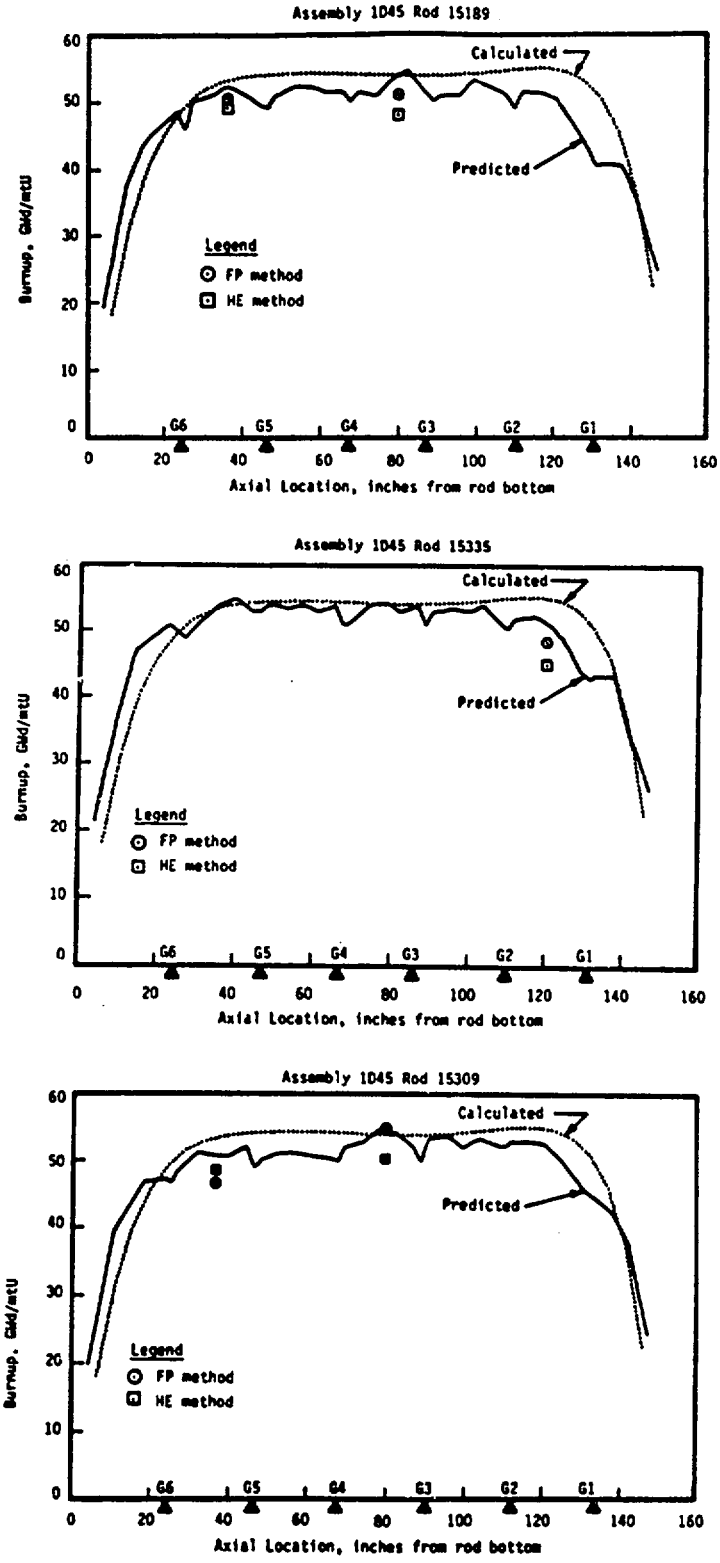

Table 4-27. Revised Chemical Burnup Analysis of Four-Cycle Fuel

Sample No.	Location[a]	Fissions/100 Initial U Atoms		Burnup, GWd/mtu			
		HE	FP	HE	FP	Predicted[b]	Calculated[c]
08639-17	34.1	4.02	4.18	38.6	40.1	42.2	44.2
08639-11	78.2	3.94	4.17	37.8	40.0	42.2	42.9
08672-33	7.2	2.23	2.00	21.4	19.2	26.0	19.6
08672-31	13.8	3.32	3.24	31.9	31.1	35.2	34.3
08672-28	26.2	3.83	4.02	36.8	38.6	39.2	43.1
08672-16	78.5	4.12	4.28	39.6	41.1	42.2	42.6
08672-11	99.6	4.18	4.38	40.1	42.0	43.4	42.8
08672-4	140.8	2.56	2.60	24.6	25.0	25.8	20.4
08747-16	35.4	4.22	4.55	40.5	43.7	42.7	44.6
08747-9	76.4	3.83	4.23	36.8	40.6	43.9	43.3
09603-18	35.8	4.12	4.29	39.6	41.2	41.5	43.8
09603-9	93.4	4.22	4.50	40.5	43.2	42.6	42.9

(a) The sample location is in inches from the bottom of the rod.

(b) Predictions were based on PDQ07 rod-average burnup and the shape of the Cs-137 activity profile of each rod.

(c) Calculations were based on the PDQ07 rod-average burnup and the FLAME3 axial power profile.

rest) rod. Destructive operations were divided into (a) cladding and (b) fuel examinations. The cladding examinations included measurements of oxide thickness, hydrogen pickup, and mechanical properties, and an evaluation of the unusual surface features. Oxide thickness and hydrogen pickup increased substantially over four-cycle results, while cladding ductility decreased. These phenomena are interrelated, and further evaluation at this and higher burnups is recommended. The unusual surface features were localized, increased oxide buildup. The fuel examinations included microstructure, density, radial fission product migration, and chemical burnup measurements/ evaluations. The significant finding was a reaction layer/bond between the fuel and cladding surface. The attributes of this layer were not determined in this study.

5. HIGH-BURNUP EFFECTS

5.1. Introduction

Mark B fuel assemblies operate routinely to burnups near 40 GWd/mtU. These fuel assemblies have operated in a reliable manner with an overall fuel integrity of 99.97%. Near-term projected operation is to a fuel assembly burnup of 55 GWd/mtU. In preparation to reach this projected burnup, data were gathered from standard assemblies after exposures of from one to five cycles in-reactor and to a maximum burnup of 50.2 GWd/mtU. Data were obtained through poolside nondestructive examinations and hot cell nondestructive and destructive examinations. Based on the results of these examinations, a number of observations have been made.

During irradiation, material property and dimensional changes in the fuel rod affect its performance. These irradiation-induced changes are in the following areas:

1. Yield and ultimate tensile strength of the cladding.
2. Cladding ductility.
3. Diametral creep of the cladding.
4. Fission gas release from the fuel pellet.
5. Fuel swelling.
6. Growth in fuel rod length.

Additionally, the longer exposure to high-temperature coolant results in the following changes to the cladding:

7. Increase in thickness of the waterside oxide layer.
8. Increase in hydrogen content of the cladding.

Item 8 results from the hydrogen being a byproduct of cladding corrosion. The groups of changes above are discussed in sections 5.2 and 5.3. Section 5.4 provides a summary of the section and denotes areas where research and development are needed.

5.2. Irradiation-Induced Changes

During in-reactor operation, exposure to fast neutron flux increases the yield and ultimate tensile strengths of the Zircaloy-4 cladding. The increase is rapid during the first cycle, then progresses at a slower rate during further exposure. At fast neutron fluences (E>1 MeV) of 9.2×10^{21} n/cm^2, the average yield and ultimate tensile strengths were 50 and 41%, respectively, greater than their pre-irradiated values. The average yield strength was 87.8 ksi, and the average ultimate tensile strength was 102.4 ksi. The fuel rod is designed for a minimum unirradiated yield strength of 45 ksi. Thus, the higher fluence results in increasing margins for stress; although associated cladding property changes can affect other areas of performance.

Over the five cycles of irradiation, cladding axial ductility (uniform elongation) decreased an average of 59%, with about 25% occurring during the first cycle and about 30% occurring during the fifth cycle. The cause of the reduction in cladding ductility at high burnups is not clear at this time. The sharp reduction at high burnup is a concern because of the decreased ability of the cladding to respond to pellet-induced strains. These strains will be more severe, for a given power increase, at higher burnups due to the harder pellet-cladding interaction that occurs. Yet, the higher burnup fuel is less likely to experience power increases of significant magnitude. Therefore, for a single event, the reduction in the cladding minimum uniform elongation is not a concern. The low ductility may represent a problem during repeated power changes when the available ductility may be exhausted through a ratcheting effect of the fuel pellets on the cladding. Currently, difficulty exists in determining quantitatively how much the decrease in cladding ductility will affect fuel rod reliability at high burnups.

Diametral creep is a time-dependent radiation and temperature-induced strain of the cladding material. The material deforms in the directions as dictated by the stress state within the cladding. During normal operation of Mark B fuel rod cladding, the hoop stress is always compressive. Thus, the diameter will decrease, and the cladding ovality will increase until the cladding is supported by the fuel pellet. If a large axial gap develops in the fuel column, the cladding can ovalize until it collapses. The time and burnup at

which collapse is predicted is defined as the creep collapse life of the fuel rod.

Creep collapse life must be greater than the in-reactor exposure of the fuel rod. In modern design fuel (95% theoretical density), creep collapse is no longer a concern because of small irradiation-induced density changes and lack of appreciable (> 0.5 inch) pellet-to-pellet gaps. Consequently, the high fill-gas pressures used in the past to prevent creep collapse can be safely lowered to provide additional margin for fission gas release.

The swelling of fuel pellets and the decrease in cladding diameter will bring the fuel pellet and the cladding into contact. The pellet-cladding contact will result in the cladding being strained by changes in the fuel pellet diameter. This phenomenon is known as pellet-cladding mechanical interaction (PCMI). During the fifth cycle of irradiation, no change in the cladding diameter occurred, which indicates that hard mechanical contact occurs at about 30 to 40 GWd/mtU. Lower initial fill-gas pressures will result in hard contact occurring at a lower burnup.

Further effects due to pellet-cladding contact were identified in the five-cycle fuel examination. The hard contact of the fuel pellet and cladding allowed the cladding to become bonded to the fuel. The microstructure of the fuel near the bond interface was very porous. A diffusion couple between the fuel and the cladding ID was clearly evident. The bonding between the pellet and the cladding came after hard pellet-cladding contact was established. This bond seems to be responsible for the accelerated fuel rod growth. The effect of this reaction zone on fuel and cladding performance is not well understood, and current calculational models do not simulate its existence.

Due to fission gas release, the internal pressure of a fuel rod will increase at high burnups. Some fuel rod design criteria require that rod pressure be held to less than system pressure. The initial fill-gas pressure in the fuel rod contributes most of the rod pressure. The lower the initial pressure, the longer the time for rod pressure to reach system pressure. Analysis of plenum gases after 50 GWd/mtU burnups showed a fractional fission gas release of 3.8% (1.6% average, based on 16 rods). At these low levels of fission gas release, rod pressure would not present a problem for burnups up to 60

GWd/mtU. The licensing analysis for rod pressure assumes continuous high-power operation, and a fission gas release enhancement factor that is exponentially dependent upon burnup. Thus, this method predicts a conservatively large fractional fission gas release. The burnup limit based on current bounding methods of analysis is 51 GWd/mtU.

During irradiation, the fuel pellet density changes, increasing early in life and then decreasing throughout the remainder of the incore exposure. The overall effect of the swelling behavior is to speed up pellet-cladding contact. Fuel swelling in the diametral direction appeared to be re-trained during the fifth cycle because the diameter of the fuel rod (corrected for oxide thickness) remained essentially constant over the fifth cycle. Based on the creep characteristics of the cladding, no change in diameter implies either that the cladding is still in a compressive state or that the tensile hoop stress is minimal. Additionally, the cladding undergoes an irradiation-induced, stress-free growth in length during irradiation. Mark B fuel rod growth data have been consistent with predictions of burnups to 40 GWd/mtU. During the fifth cycle of exposure (40 to 50 GWd/mtU), the rate of cladding axial growth increased, correlating well with the rate of fuel stack axial growth. If fuel rod growth were to continue at this accelerated rate, the fuel rods would come in hard contact with the upper and lower end fittings at a burnup of less than 55 GWd/mtU. Further growth and thermal strains would than cause the fuel rods to bow, affecting the coolant flow channels through the fuel assembly.

5.3. High-Temperature Coolant-Induced Changes

The oxidation of the cladding during exposure to high-temperature coolant has several effects. As the oxide layer builds, the thickness of the remaining cladding is reduced. The ratio of oxide thickness gained to Zircaloy thickness lost is about 1.6:1. For analytical purposes, the oxide layer is assumed to be unable to carry a load. The reduced thickness of the cladding as the oxide layer grows results in higher stresses in the cladding and faster creep deformation. The oxide buildup follows the temperature profile of the base metal, with the thickest oxide layer being at the hottest cladding location. Oxide thickness data through 50 GWd/mtU show accelerated growth of oxide film thickness past 40 GWd/mtU. The maximum oxide thickness measured after five cycles (1553 EFPDs) of exposure is about 3 mils. A

reduction in cladding thickness of 2.6 mils (10% of the cladding wall) is acceptable. This wall thickness reduction is equivalent to an oxide layer buildup of about 4 mils. Based on extrapolations of oxide layer growth rates, burnups through 60 GWd/mtU are achievable, assuming that the trend observed from 40 to 50 GWd/mtU extends to 60 GWd/mtU.

As the cladding is oxidized, a certain percentage of the hydrogen released is absorbed by the base metal. When the hydrogen concentration exceeds the solubility limit for the cladding (~200 ppm at 650F), the hydrogen precipitates in the form of zirconium-hydride platelets. The maximum hydrogen concentration measured after four cycles was 182 ppm; after five cycles, the maximum was 408 ppm. The effect, if any, of zirconium-hydride on cladding ductility and cladding fatigue behavior needs further study. An increase in the number density of zirconium-hydride precipitates with increasing burnup may contribute to a decrease in cladding ductility.

5.4. Summary and Conclusions

Data from hot cell examinations indicate that the performance margin of high-burnup fuel is reduced, and that the margin remaining cannot be easily quantified. Current indications are that the margins are adequate with existing fuel designs up to burnups of 50 GWd/mtU (batch-average). Minor design changes can extend fuel operation to 55 GWd/mtU, e.g., changing the end fitting to accommodate accelerated fuel rod growth. However, a major concern is the bonding of the pellet and cladding at high burnup. With this intimate pellet-to-cladding contact, power changes at high burnup will repeatedly strain the cladding to a greater extent than has been the case at lower burnups. This cyclic strain, in combination with the reduction in cladding ductility, could reduce the reliability of the fuel. More high-burnup data and benchmarked models are required to confidently operate full batches of fuel beyond 55 GWd/mtU.

To accurately model fuel rods at high burnups, the following data are required on high-burnup cladding material properties:

1. Ductility in both the hoop and axial directions at high burnup. The associated tests need to be performed on cladding with a range of oxide layer thicknesses, known texture, hydrogen content, and characterized zirconium-hydride morphology.

2. Creep characteristics of cladding from high-burnup fuel rods. The tests should be conducted in a manner similar to tests on unirradiated cladding to allow for comparison.

3. Susceptibility to stress corrosion cracking (SCC). Tests are needed to determine if the as-irradiated cladding is more susceptible to SCC than unirradiated cladding. Additional samples of high-burnup cladding should have a thickness of several mils removed from the inside diameter, and then subjected to the same SCC test conditions. This would be useful in assessing the effect of fuel-cladding reaction zones and in determining if barrier-type claddings, such as zirconium-lined cladding, would be effective.

4. Fatigue properties of cladding (well characterized, as in 1 above) with thick oxide layers.

The following models are also required:

5. A cladding and pellet model that will allow for accurate simulation of PCMI under high-burnup conditions is needed. This may require developing a three-dimensional, finite-element model. A cracked-pellet model is needed to account for pellet fragment relocation. This would be used to analyze the equilibrium conditions observed between the cladding and the fuel pellets. When benchmarked to high-burnup data, these models would permit an analysis of the effects of operations such as load-following.

Some of the high-burnup phenomena discussed herein are interrelated. Changes in design that extend the limit for one criterion may reduce the limit for others. To separate and categorize effects is difficult, considering the limited data base in the high-burnup regime. By expanding the high-burnup data base and improving modeling methods, the reliable operation of fuel assemblies through burnups of 60 GWd/mtU may be achieved.

6. REFERENCES

[1] T. A. Coleman, et al., Qualification of the B&W Mark B Fuel Assembly for High Burnup, First Semi-Annual Progress Report: July -- December 1978, BAW-1546-1, Babcock & Wilcox, Lynchburg, Virginia, August 1979.

[2] T. A. Coleman, et al., Qualification of the B&W Mark B Fuel Assembly for High Burnup, Second Semi-Annual Progress Report: January -- June 1979, BAW-1546-2, Babcock & Wilcox, Lynchburg, Virginia, December 1979.

[3] T. A. Coleman, et al., Qualification of the B&W Mark B Fuel Assembly for High Burnup, Third Semi-Annual Progress Report: July -- December 1979, BAW-1546-3, Babcock & Wilcox, Lynchburg, Virginia, March 1980.

[4] T. A. Coleman, et al., Qualification of the B&W Mark B Fuel Assembly for High Burnup, Fourth Semi-Annual Progress Report: January -- June 1980, BAW-1546-4, Babcock & Wilcox, Lynchburg, Virginia, September 1980.

[5] T. A. Coleman, et al., Qualification of the B&W Mark B Fuel Assembly for High Burnup, Fifth Semi-Annual Progress Report: July -- December 1980, BAW-1546-5, Babcock & Wilcox, Lynchburg, Virginia, April 1981.

[6] T. A. Coleman, et al., Qualification of the B&W Mark B Fuel Assembly for High Burnup, Sixth Semi-Annual Progress Report: January -- June 1981, BAW-1546-6, Babcock & Wilcox, Lynchburg, Virginia, October 1981.

[7] T. A. Coleman, et al., Qualification of the B&W Mark B Fuel Assembly for High Burnup, Seventh Semi-Annual Progress Report: July -- December 1981, BAW-1546-7, Babcock & Wilcox, Lynchburg, Virginia, May 1982.

[8] T. A. Coleman, et al., Qualification of the B&W Mark B Fuel Assembly for High Burnup, Eighth Semi-Annual Progress Report: January -- June 1982, BAW-1546-8, Babcock & Wilcox, Lynchburg, Virginia, September 1982.

[9] T. A. Coleman, et al., Qualification of the B&W Mark B Fuel Assembly for High Burnup, Ninth Semi-Annual Progress Report: July -- December 1982, BAW-1546-9, Babcock & Wilcox, Lynchburg, Virginia, July 1983.

[10]T. A. Coleman, et al., Development of an Extended-Burnup Mark B Design, First Semi-Annual Progress Report: July -- December 1978, BAW-1532-1, Babcock & Wilcox, Lynchburg, Virginia, November 1979.

[11]T. A. Coleman, et al., Development of an Extended-Burnup Mark B Design, Second Semi-Annual Progress Report: January -- June 1978, BAW-1532-2, Babcock & Wilcox, Lynchburg, Virginia, November 1979.

[12]T. A. Coleman, et al., Development of an Extended-Burnup Mark B Design, Third Semi-Annual Progress Report: July -- December 1979, BAW-1532-3, Babcock & Wilcox, Lynchburg, Virginia, March 1980.

[13]T. A. Coleman, et al., Development of an Extended-Burnup Mark B Design, Fourth and Fifth Semi-Annual Progress Report: January -- December 1980, BAW-1532-4, -5, Babcock & Wilcox, Lynchburg, Virginia, April 1981.

[14]T. A. Coleman, et al., Development of an Extended-Burnup Mark B Design, Sixth Semi-Annual Progress Report: January -- June 1981, BAW-1532-6, Babcock & Wilcox, Lynchburg, Virginia, October 1981.

[15]T. A. Coleman, et al., Development of an Extended-Burnup Mark B Design, Seventh Progress Report: July 1981 -- June 1982, BAW-1532-7, Babcock & Wilcox, Lynchburg, Virginia, September 1982.

[16]T. A. Coleman, et al., Development of an Extended-Burnup Mark B Design, Eighth Progress Report: July 1982 -- June 1983, BAW-1532-8, Babcock & Wilcox, Lynchburg, Virginia, March 1984.

[17]T. A. Coleman, et al., Development of an Extended-Burnup Mark B Design, Ninth Progress Report: July 1983 -- June 1984, BAW-1532-9, Babcock & Wilcox, Lynchburg, Virginia, February 1985.

[18]L. W. Newman, et al., Development and Demonstration of an Advanced Extended-Burnup Fuel Assembly Design Incorporating Urania-Gadolinia, First Semi-Annual Progress Report: March -- September 1981, BAW-1681-1, Babcock & Wilcox, Lynchburg, Virginia, February 1982.

[19]L. W. Newman, et al., Development and Demonstration of an Advanced Extended-Burnup Fuel Assembly Design Incorporating Urania-Gadolinia, Second Semi-Annual Progress Report: October 1981 -- March 1982, BAW-1681-2, Babcock & Wilcox, Lynchburg, Virginia, August 1982.

[20] L. W. Newman, et al., Development and Demonstration of an Advanced Extended-Burnup Fuel Assembly Design Incorporating Urania-Gadolinia, Third Semi-Annual Progress Report: March -- September 1982, BAW-1681-3, Babcock & Wilcox, Lynchburg, Virginia, September 1982.

[21] L. W. Newman, et al., Development of an Advanced Extended-Burnup Fuel Assembly Design Incorporating Urania-Gadolinia, Fourth Semi-Annual Progress Report: October 1982 -- March 1983, BAW-1681-4, Babcock & Wilcox, Lynchburg, Virginia, February 1984.

[22] L. W. Newman, et al., Development of an Advanced Extended-Burnup Fuel Assembly Design Incorporating Urania-Gadolinia, Fifth Semi-Annual Progress Report: April -- September 1983, BAW-1681-5, Babcock & Wilcox, Lynchburg, Virginia, October 1984.

[23] L. W. Newman, et al., Development of an Advanced Extended-Burnup Fuel Assembly Design Incorporating Urania-Gadolinia, Sixth Semi-Annual Progress Report: October 1983 -- March 1984, BAW-1681-6, Babcock & Wilcox, Lynchburg, Virginia, February 1985.

[24] L. W. Newman, et al., Development of an Advanced Extended-Burnup Fuel Assembly Design Incorporating Urania-Gadolinia, Seventh Semi-Annual Progress Report: April -- September 1984, BAW-1681-7, Babcock & Wilcox, Lynchburg, Virginia, October 1985.

[25] L. W. Newman, et al., Development of an Advanced Extended-Burnup Fuel Assembly Design Incorporating Urania-Gadolinia, Eighth Semi-Annual Progress Report: October 1984 -- March 1985, BAW-1681-8, Babcock & Wilcox, Lynchburg, Virginia, June 1986.

[26] L. W. Newman, et al., The Nondestructive Examination of an Oconee 1 Fuel Assembly After Five Cycles of Irradiation, BAW-1818, Babcock & Wilcox, Lynchburg, Virginia, July 1985.

[27] C. G. Dideon and G. M. Bain, Fuel Performance Under Extended-Burnup Operation: B&W 15x15 Design, BAW-1716, Babcock & Wilcox, Lynchburg, Virginia, September 1983.

[28] T. D. Pyecha, et al., Nondestructive Examination of Oconee 1 Fuel Assemblies After Three Cycles of Irradiation, BAW-1553, Babcock & Wilcox, Lynchburg, Virginia, September 1979.

[29]T. D. Pyecha, et al., Nondestructive Examination of Oconee 1 Fuel Assemblies After Four Cycles of Irradiation, BAW-1650, Babcock & Wilcox, Lynchburg, Virginia, April 1981.

[30]H. A. Hassan, et al., Babcock & Wilcox's Version of PDQ07 -- Users Manual, BAW-10117A, Babcock & Wilcox, Lynchburg, Virginia, February 1977.

[31]FLAME3 -- A Three-Dimensional Nodal Code for Calculating Core Reactivity and Power Distributions, BAW-10124, Babcock & Wilcox, Lynchburg, Virginia, November 1975.

[32]F. Garzarolli, et al., "Waterside Corrosion of Zircaloy-Clad Fuel Rods," C-E/KWU/EPRI Project RP1250-1, Task A: Review of PWR Fuel Rod Waterside Corrosion Behavior, NPSD-79, Electric Power Research Institute, Palo Alto, California, June 1979.

[33]B. F. Rider, "Compilation of Fission Product Yields," NEDO-12154-3, General Electric, Vallecitos Nuclear Center, Pleasanton, California, September 1980.

[34]C. C. Sanderson, "The Effect of Specimen Geometry on the Tensile Properties of Some Zirconium Alloys," AECL-2207, Atomic Energy of Canada, Ltd., Chalk River, Ontario, March 1965.

[35]F. Garzarolli, et al., "Characterization of Zirconium Oxide Corrosion Films on Irradiated Zircaloy-Clad PWR Fuel Rods," NPSD-192, Combustion Engineering, Windsor, Connecticut, May 1982.

[36]F. Garzarolli, et al., "Waterside Corrosion of Zircaloy Fuel Rods," Project 1250-1, Final Report, NP-2789, Electric Power Research Institute, Palo Alto, California, December 1982.

[37]R. Manzel, et al., "Fission Gas Release of PWR Fuel Under Steady and Transient Conditions Up to High Burnup," Proceedings of the American Nuclear Society Topical Meeting on Light Water Reactor Performance, American Nuclear Society, La Grange Park, Illinois, April 1985.

APPENDIX A

Physics Data on Assembly 1D45

Table A-1. Oconee 1 High-Burnup Assembly Fuel Cycle Parameters

Cycle	BOC	EOC	Cycle length, EFPD	Core exposure at CR interchange, EFPD	Core exposure at CR withdrawal, EFPD	Approximate CR positions[a] during steady-state oper, % wd		
						Group 6	Group 7	Group 8[b]
2	02/11/75	02/07/76	292.2	53	237	84	6	5
3	03/31/76	08/05/77	308.3	100	238	95	20	22
4	10/14/77	09/02/78	245.9	N/A	N/A	100	85	31
5	10/25/78	11/22/79	303.6	N/A	N/A	100	90	25
7	12/28/81	06/01/83	403.3	N/A	N/A	100	95	30

[a]Before control rod (CR) withdrawal.
[b]APSRs.

Table A-2. Calculated Power Peaking Factors -- Oconee 1, Cycle 2

Exposure, EFPD	Core burnup, MWd/mtU	Ass'y burnup, MWd/mtU	Reactor power, % RP	Ass'y rel power[a]	Max node rel power[b]	Max node axial location[c]	Peak rods rel power[d]
Assembly 1D45 in Core Location L-14							
22.5	6,268	963	98.0	1.293	1.793	25	1.108
65.0	7,598	2,700	99.5	1.381	1.810	56	1.103
103.5	8,785	4,352	98.8	1.339	1.711	52	1.101
131.0	9,639	5,496	98.6	1.295	1.671	47	1.099
156.0	10,416	6,502	98.7	1.276	1.602	47	1.098
184.0	11,286	7,613	99.9	1.257	1.560	34	1.097
217.0	12,312	8,902	99.1	1.216	1.575	25	1.096
235.0	12,871	9,582	99.8	1.226	1.465	110	1.135
252.9	13,427	10,264	99.8	1.222	1.354	34	1.134
273.5	14,068	11,047	99.8	1.218	1.457	25	1.127
290.9[e]	14,609	11,706					

[a] Assembly relative power = assembly power x 177/core power (FLAME-calculated).

[b] Maximum node relative power = maximum nodal power x 177 x 32/core power (FLAME-calculated).

[c] Inches from bottom of fuel column to center of node of maximum relative power.

[d] Peak rod relative power = maximum rod power x 208/assembly power (two-dimensional PDQ07-calculated).

[e] The total exposure for this cycle was 292.2 EFPDs.

Table A-3. Calculated Power Peaking Factors -- Oconee 1, Cycle 3

Exposure, EFPD	Core burnup, MWd/mtU	Ass'y burnup, MWd/mtU	Reactor power, % RP	Ass'y rel power[a]	Max node rel power[b]	Max node axial location[c]	Peak rods rel power[d]
Assembly 1D45 in Core Location K-11							
32.0	9,174	13,076	100.0	1.362	1.615	119	1.065
59.0	10,023	14,225	100.0	1.327	1.538	119	1.065
97.5	11,229	15,811	99.9	1.291	1.472	20	1.065
121.9	11,992	16,758	99.9	1.231	1.467	25	1.077
165.2	13,346	18,412	99.3	1.210	1.446	25	1.071
189.3	14,099	19,324	99.9	1.211	1.436	25	1.069
203.3	14,539	19,857	98.9	1.198	1.[illegible]92	25	1.068
245.8	15,868	21,448	100.2	1.177	1.257	79	1.093
273.0	16,721	22,454	100.1	1.172	1.307	97	1.087
308.3	17,841	23,773					

[a] Assembly relative power = assembly power x 177/core power (FLAME-calculated).

[b] Maximum node relative power = maximum nodal power x 177 x 32/core power (FLAME-calculated).

[c] Inches from bottom of fuel column to center of node of maximum relative power.

[d] Peak rod relative power = maximum rod power x 208/assembly power (two-dimensional PDQ07-calculated).

Table A-4. Calculated Power Peaking Factors -- Oconee 1, Cycle 4

Exposure, EFPD	Core burnup, MWd/mtU	Ass'y burnup, MWd/mtU	Reactor power, % RP	Ass'y rel power[a]	Max node rel power[b]	Max node axial location[c]	Peak rods rel power[d]
Assembly 1D45 in Core Location E-3							
23.4	10,717	24,462	100.0	0.946	1.134	106	1.076
46.2	11,430	25,136	99.6	0.954	1.092	43	1.072
76.5	12,380	26,044	99.0	0.959	1.127	101	1.068
103.4	13,220	26,849	99.9	0.963	1.101	101	1.063
125.2	13,902	27,505	99.5	0.969	1.114	92	1.058
150.7	14,702	28,279	99.0	0.965	1.079	101	1.053
174.8	15,457	29,009	98.8	0.962	1.085	34	1.049
208.6	16,514	30,030	99.7	0.965	1.060	110	1.044
234.7	17,331	30,819	99.6	0.966	1.070	29	1.041
245.9	17,679	31,155					

[a] Assembly relative power = assembly power x 177/core power (FLAME-calculated).

[b] Maximum node relative power = maximum nodal power x 177 x 32/core power (FLAME-calculated).

[c] Inches from bottom of fuel column to center of node of maximum relative power.

[d] Peak rod relative power = maximum rod power x 208/assembly power (two-dimensional PDQ07-calculated).

Table A-5. Calculated Power Peaking Factors -- Oconee 1, Cycle 5

Exposure, EFPD	Core burnup, MWd/mtU	Ass'y burnup, MWd/mtU	Reactor power, % RP	Ass'y rel power[a]	Max node rel power[b]	Max node axial location[c]	Peak rods rel power[d]
Assembly 1D45 in Core Location H-11							
24.5	9,682	31,857	97.0	0.916	1.090	83	1.104
44.4	10,305	32,429	97.0	0.918	1.050	83	1.101
90.4	11,744	33,746	99.5	0.915	1.023	83	1.092
118.1	12,611	34,534	99.0	0.909	1.017	79	1.085
145.4	13,465	35,310	99.5	0.904	1.030	79	1.078
175.3	14,401	36,161	98.8	0.910	1.029	74	1.072
207.5	15,409	37,076	99.1	0.909	0.990	25	1.067
239.7	16,417	37,993	98.2	0.911	1.034	74	1.064
263.6	17,165	38,675	98.5	0.914	1.015	74	1.062
288.1	17,931	39,377	93.8	0.917	1.012	74	1.060
303.6	18,416	39,822					

(a) Assembly relative power = assembly power x 177/core power (FLAME-calculated).

(b) Maximum node relative power = maximum nodal power x 177 x 32/core power (FLAME-calculated).

(c) Inches from bottom of fuel column to center of node of maximum relative power.

(d) Peak rod relative power = maximum rod power x 208/assembly power (two-dimensional PDQ07-calculated).

Table A-6. Calculated Power Peaking Factors -- Oconee 1, Cycle 7

Exposure, EFPD	Core burnup, MWd/mtU	Ass'y burnup, MWd/mtU	Reactor power, % RP	Ass'y rel power[a]	Max node rel power[b]	Max node axial location[c]	Peak rods rel power[d]
Assembly 1D45 in Core Location H-8							
7.5	9,613	40,008	99.4	0.806	0.911	101	1.078
45.2	10,793	40,702	99.7	0.809	0.909	105	1.066
102.3	12,580	42,144	100.2	0.818	0.897	101	1.055
123.4	13,240	42,681	99.9	0.823	0.899	101	1.051
162.8	14,473	43,691	99.9	0.834	0.909	117	1.044
208.4	15,890	45,454	100.1	0.849	0.920	54	1.039
243.4	16,995	45,810	100.0	0.863	0.932	54	1.032
288.6	18,410	47,027	100.3	0.878	0.959	47	1.030
326.7	19,602	48,070	100.1	0.888	0.953	119	1.028
361.5	20,691	49,033	100.2	0.897	0.960	54	1.028
401.8	21,952	50,119	71.6	0.915	1.028	74	1.028
403.3	21,999	50,160					

[a] Assembly relative power = assembly power x 177/core power (FLAME-calculated).

[b] Maximum node relative power = maximum nodal power x 177 x 32/core power (FLAME-calculated).

[c] Inches from bottom of fuel column to center of node of maximum relative power.

[d] Peak rod relative power = maximum rod power x 208/assembly power (two-dimensional PDQ07-calculated).

Table A-7. Assembly 1D45 Calculated Fuel Rod Burnups After Five Cycles of Irradiation

	0	1	2	3	4	5	6	7
0	0	50562	50120	50120	50120	50120	49621	49494-ℓ
1	50562	50562	50120	50120	50120	50120	49621	49494
2	50288	50288	0	50957	50957	0	49746	49480
3	50288	50288	50957	50957	50957	50957	49746	49480
4	50288	50288	50957	50957	0	50957	49746	49480
5	50288	50288	0	50957	50957	50957	49746	49480
6	50075	50078	50031	50031	50031	50031	49115	49493
7	50103 ℓ	50103	49922	49922	49922	49922	49493	49493

Note: Assembly 1D45 was in the center core location for its fifth cycle. The burnups are shown for a quarter of the assembly and symmetry is assumed.

Figure A-1. High-Burnup Assembly and Control Rod Group Locations

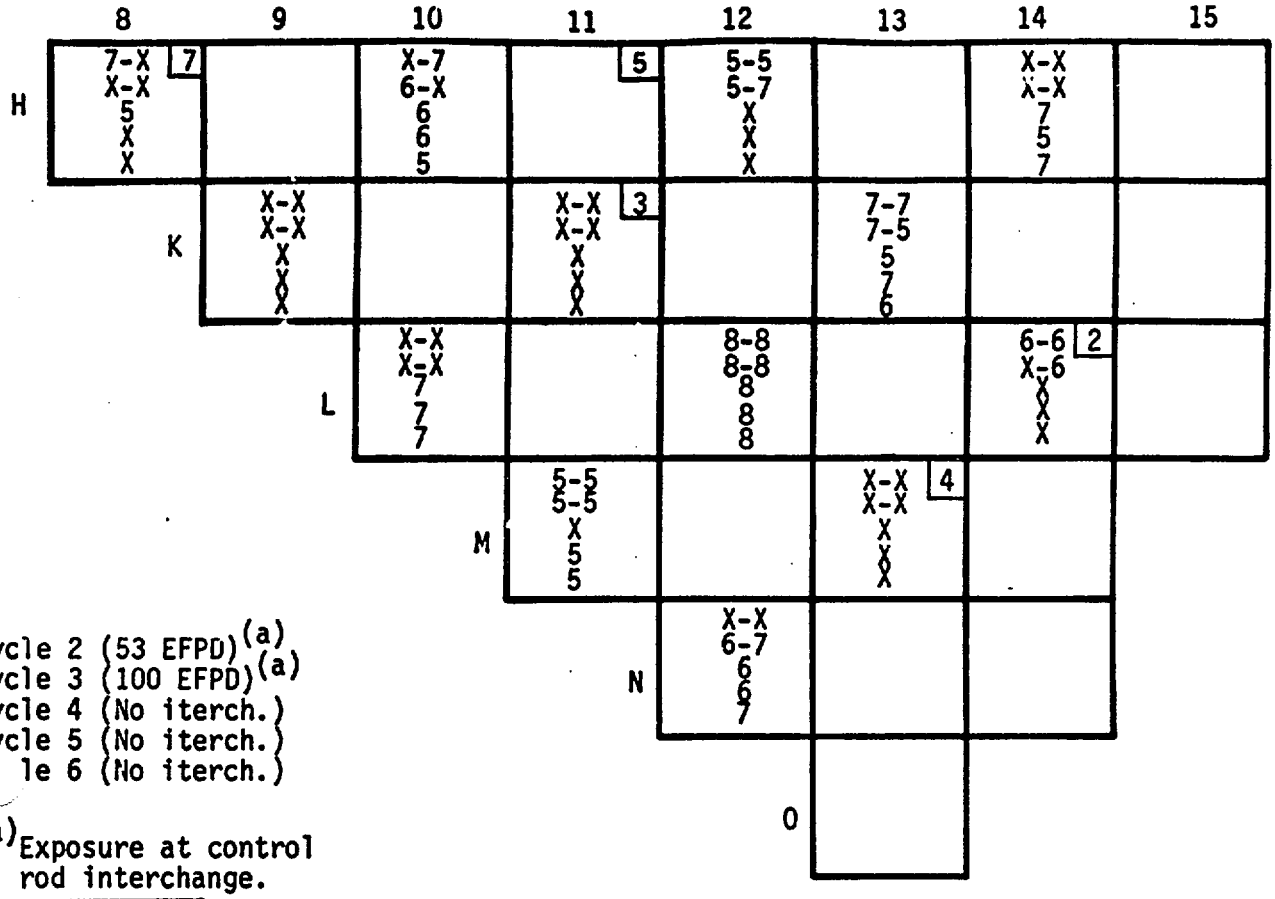

Cycle 2 (53 EFPD)(a)
Cycle 3 (100 EFPD)(a)
Cycle 4 (No iterch.)
Cycle 5 (No iterch.)
Cycle 6 (No iterch.)

(a) Exposure at control rod interchange.

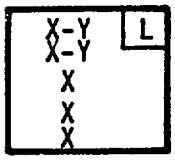

Legend

[i] Location of assembly 1D45 during cycle i.

x-y CR group designation before-after rod group interchange.

X Shutdown group (groups 1 through 4)

5 Doppler group (normally 100% wd)

6,7 Transient groups

8 APSR group

Figure A-2. Power History -- Oconee 1, Cycle 2

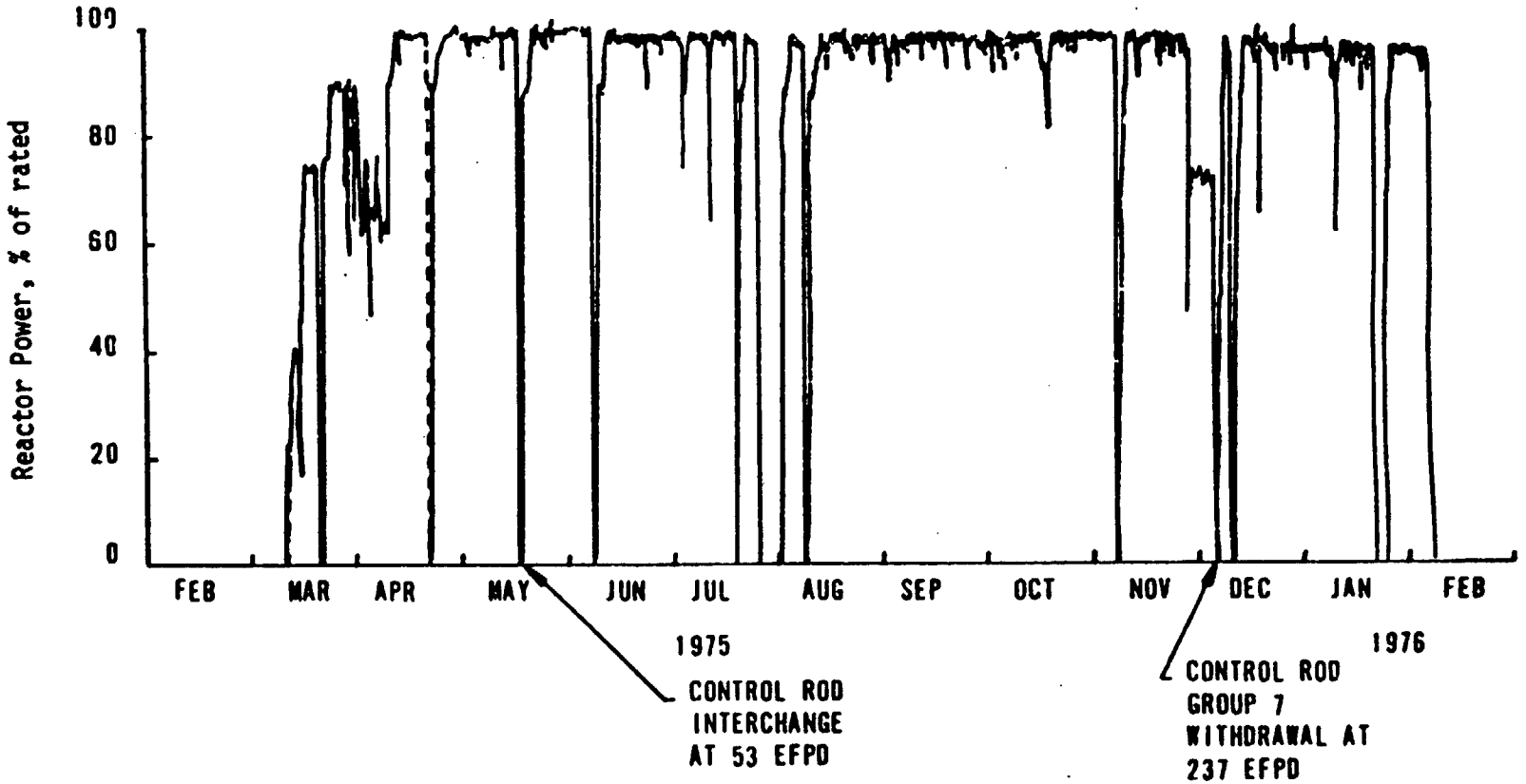

Figure A-3. Power History -- Oconee 1, Cycle 3

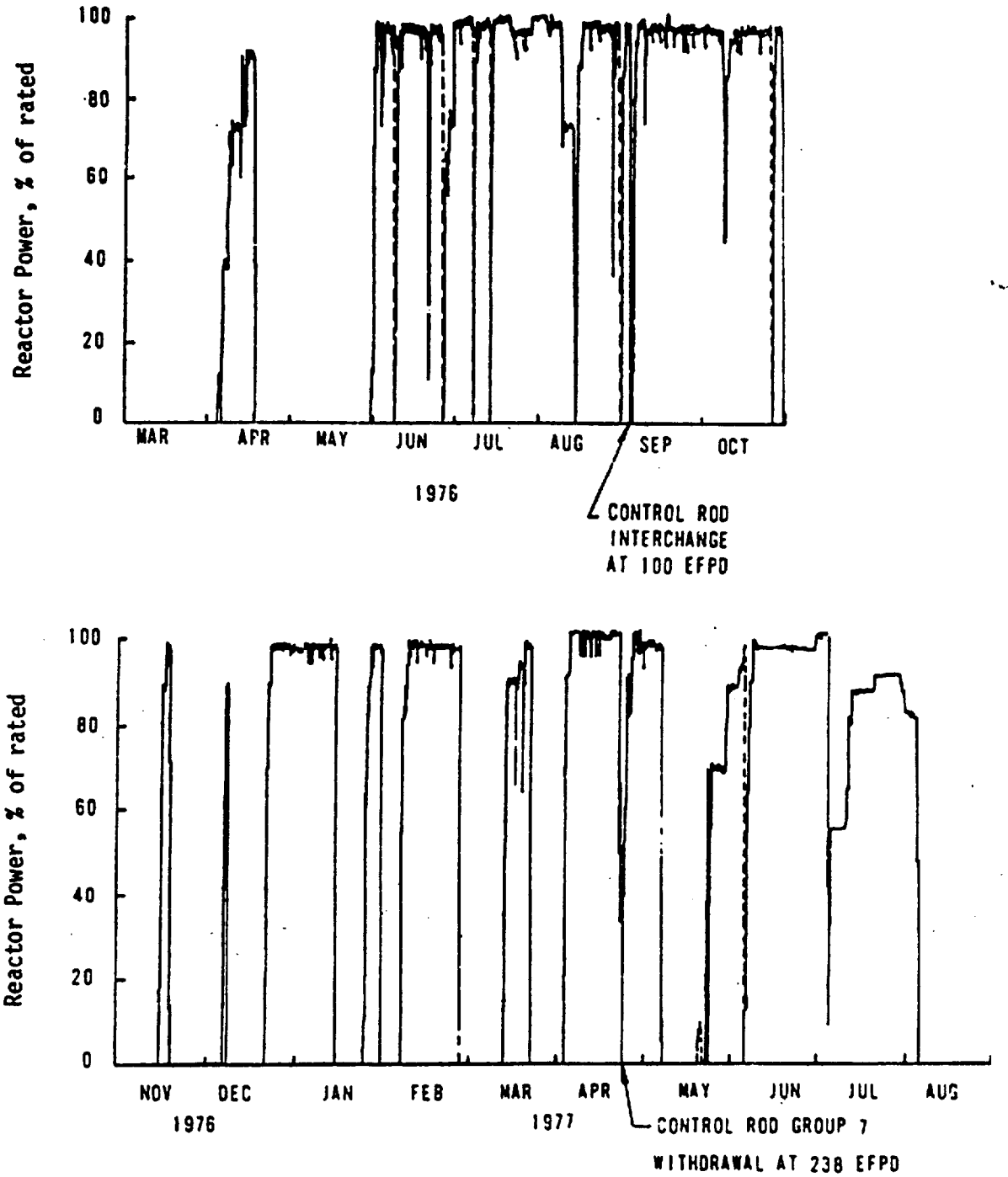

Figure A-4. Power History -- Oconee 1, Cycle 4

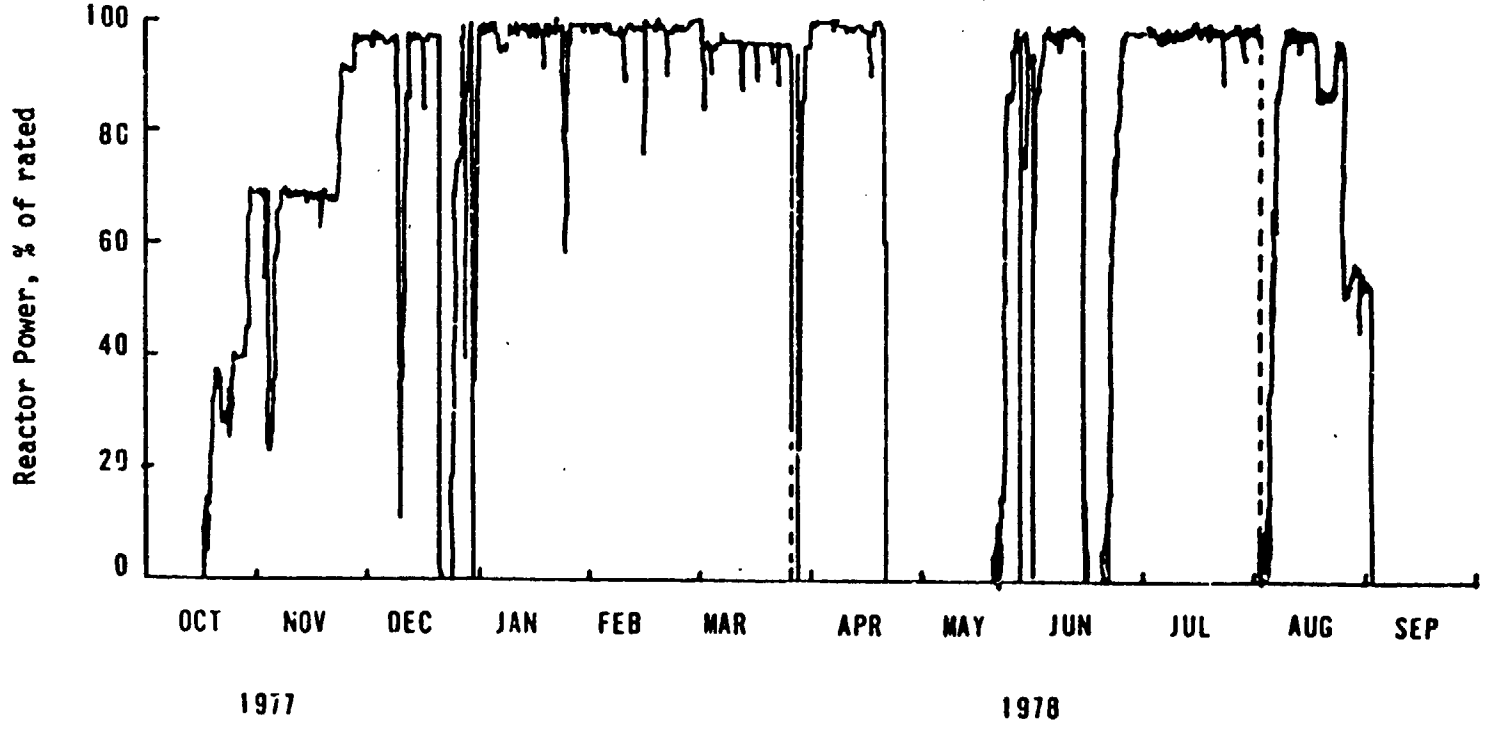

Figure A-5. Power History -- Oconee 1, Cycle 5

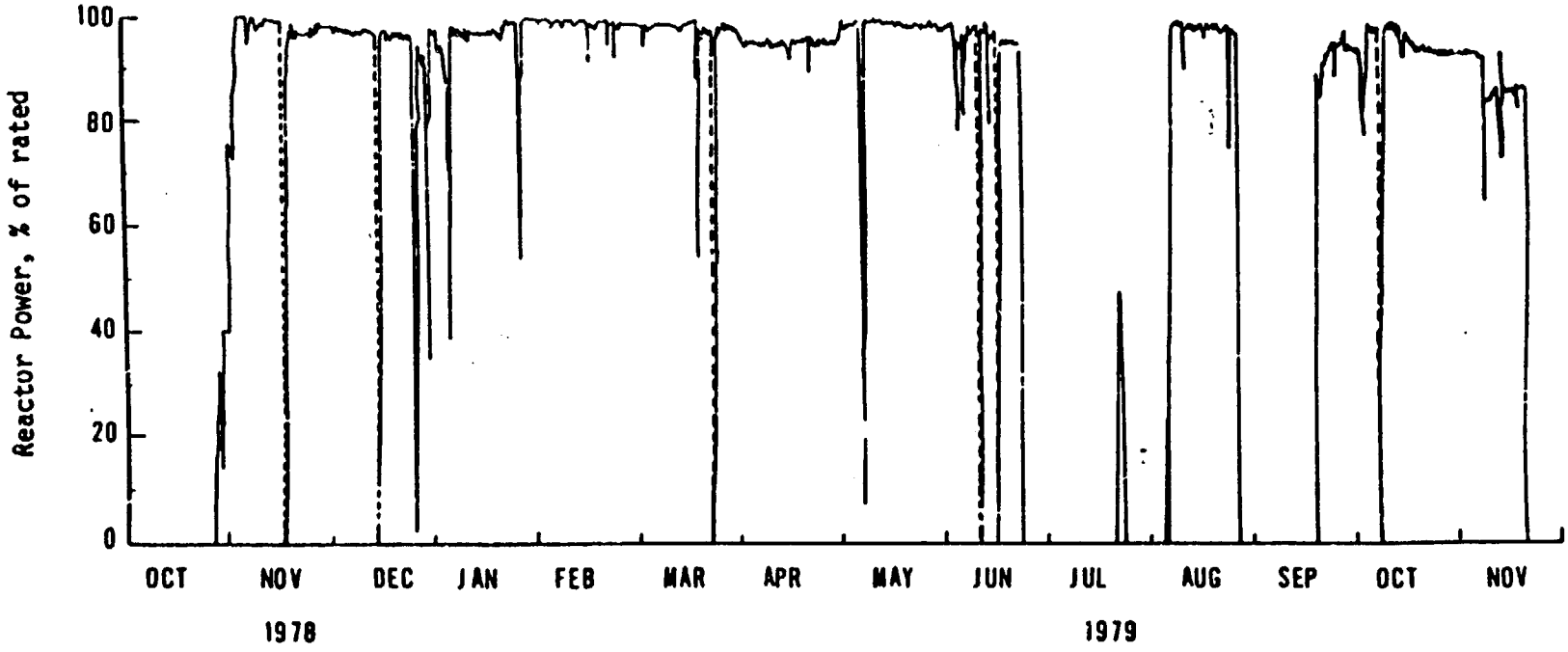

Figure A-6. Power History -- Oconee 1, Cycle 7

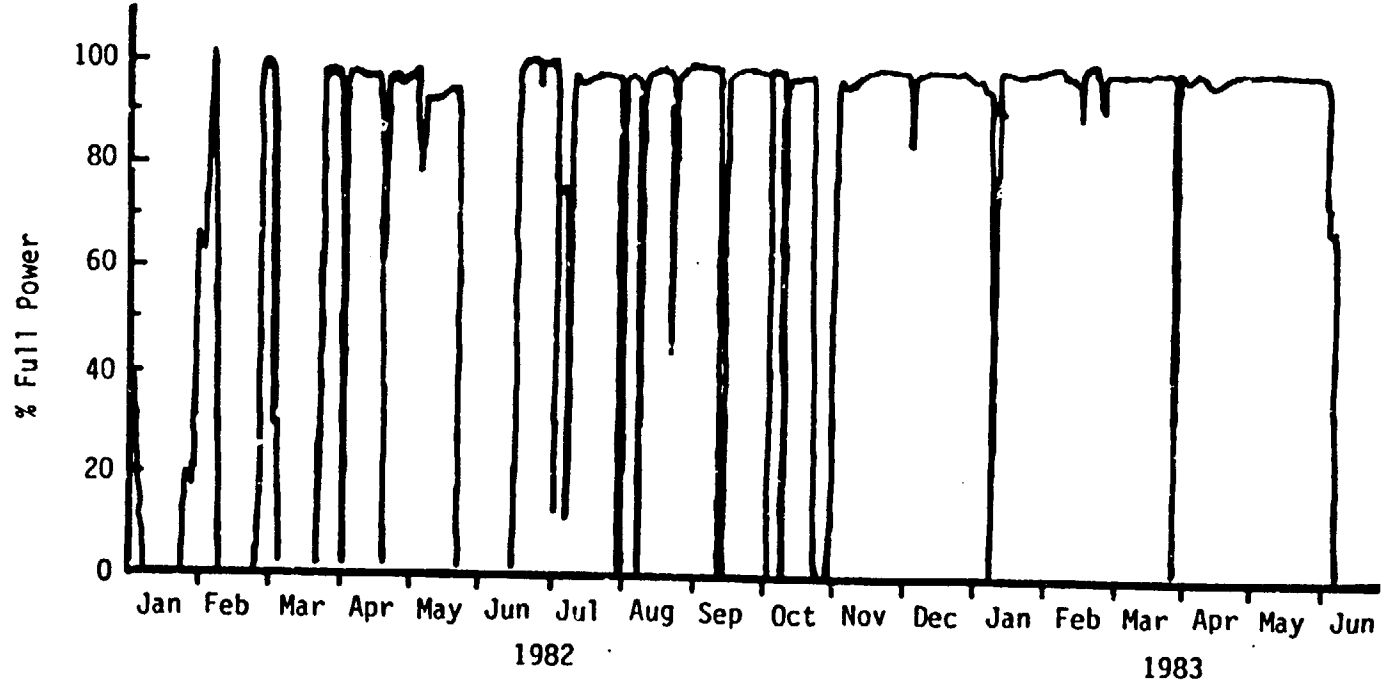

Figure A-7. Average Power History for Assembly 1D45

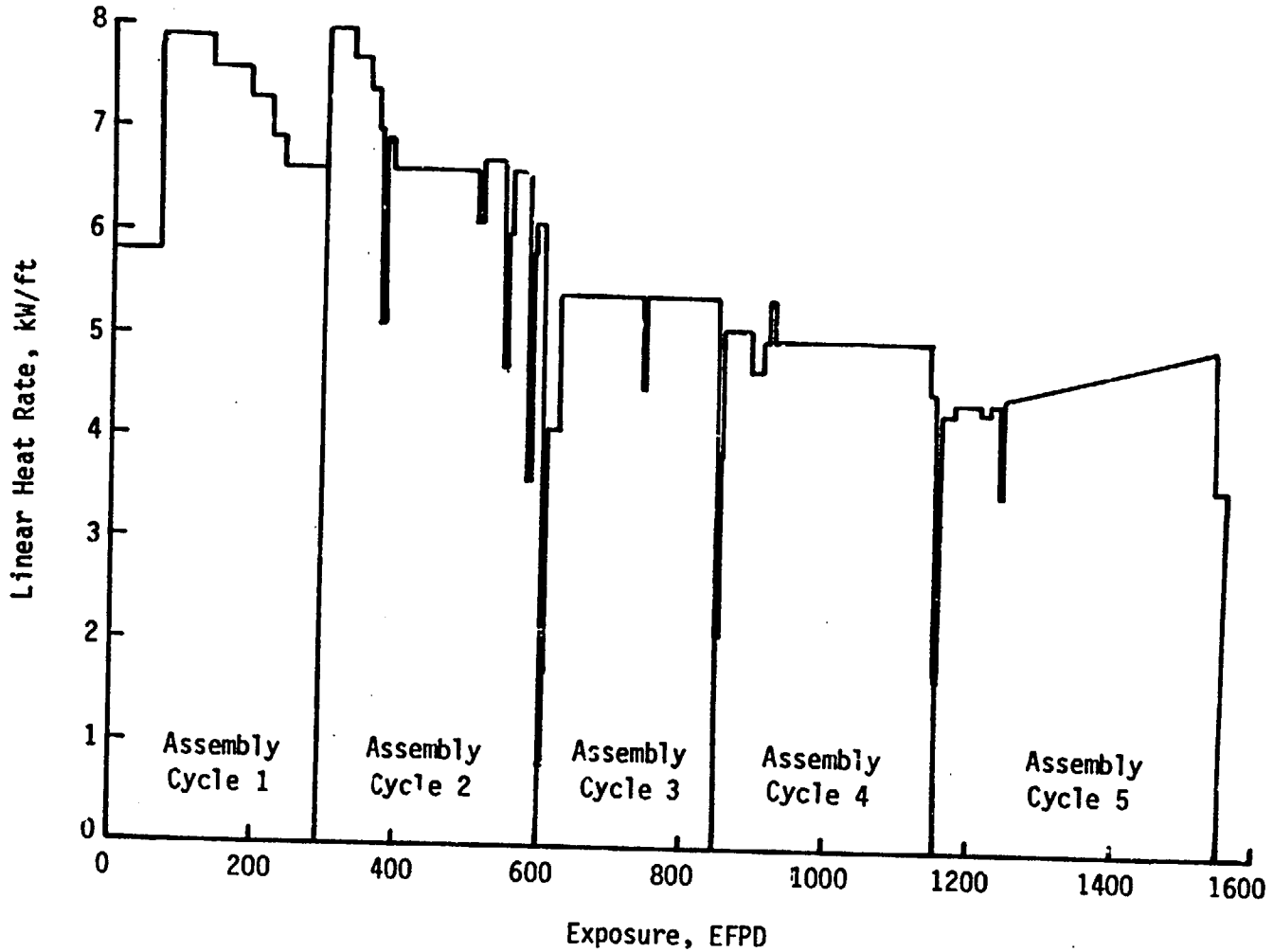

Figure A-8. Axial Power Profile -- Assembly 1D45, Oconee 1 Cycle 2

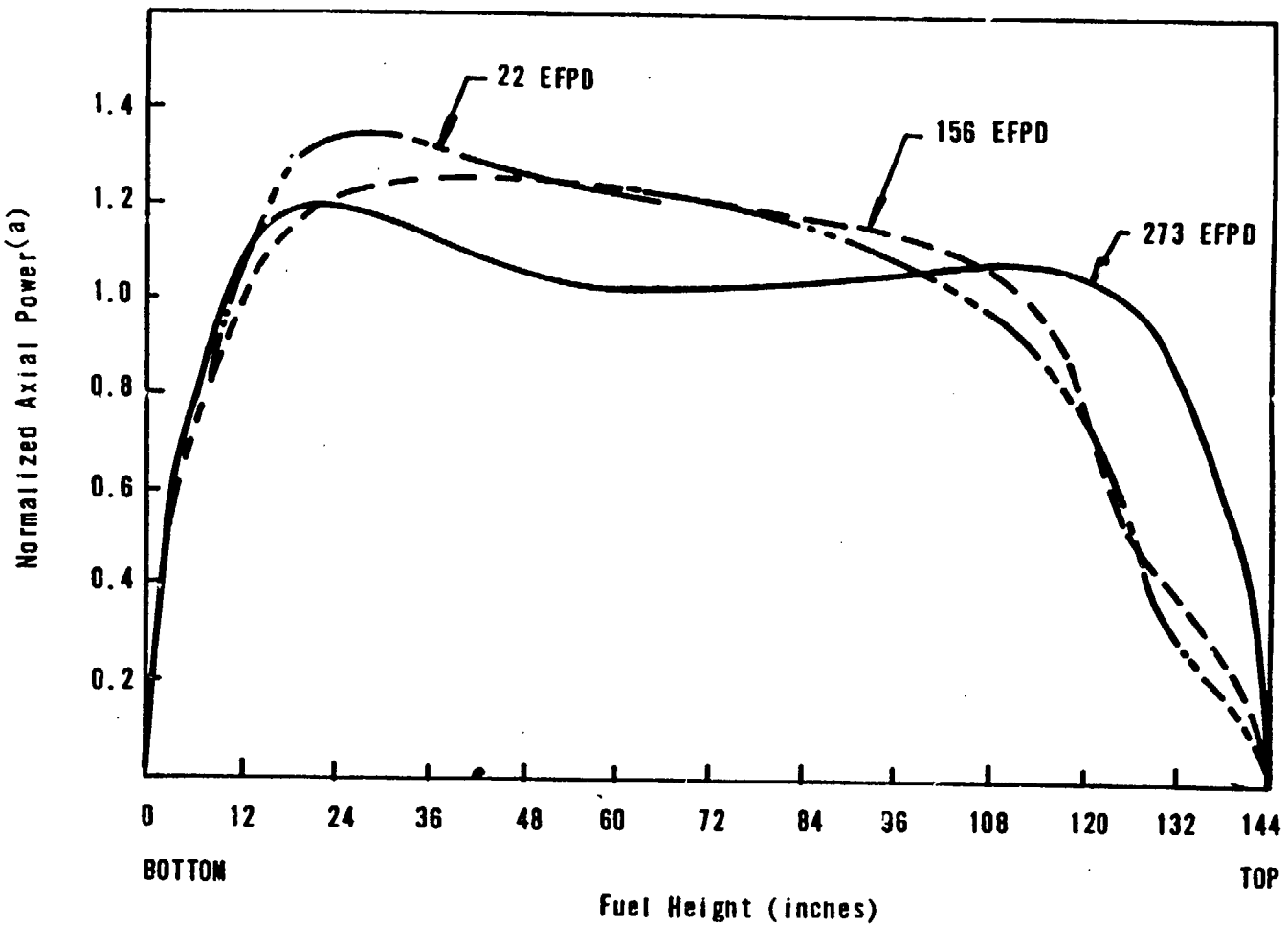

(a)NORMALIZED TO AN AVERAGE VALUE OF 1.0

Figure A-9. Axial Power Profile -- Assembly 1D45, Oconee 1 Cycle 3

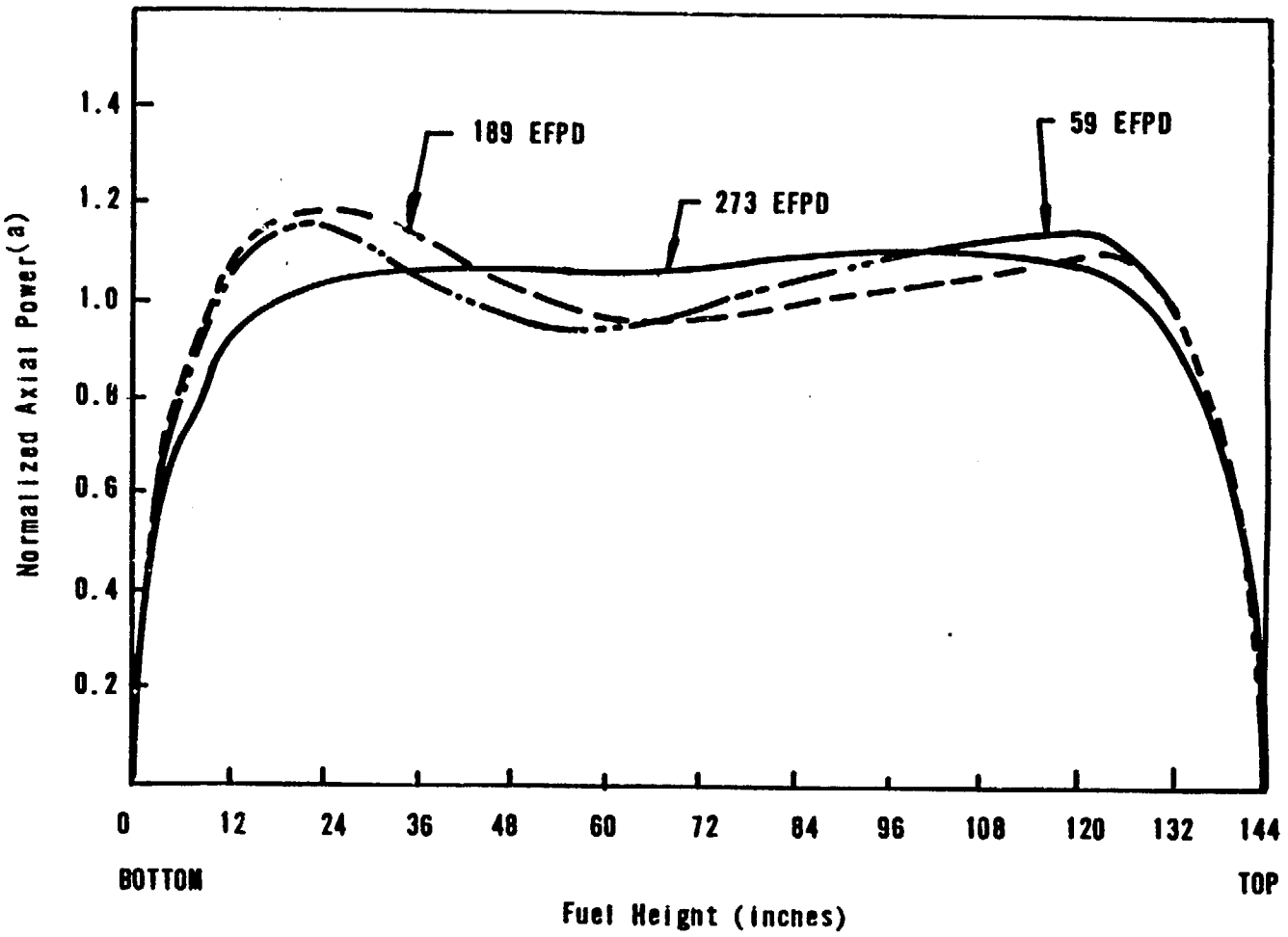

(a) NORMALIZED TO AN AVERAGE VALUE OF 1.0

Figure A-10. Axial Power Profile -- Assembly 1D45, Oconee 1 Cycle 4

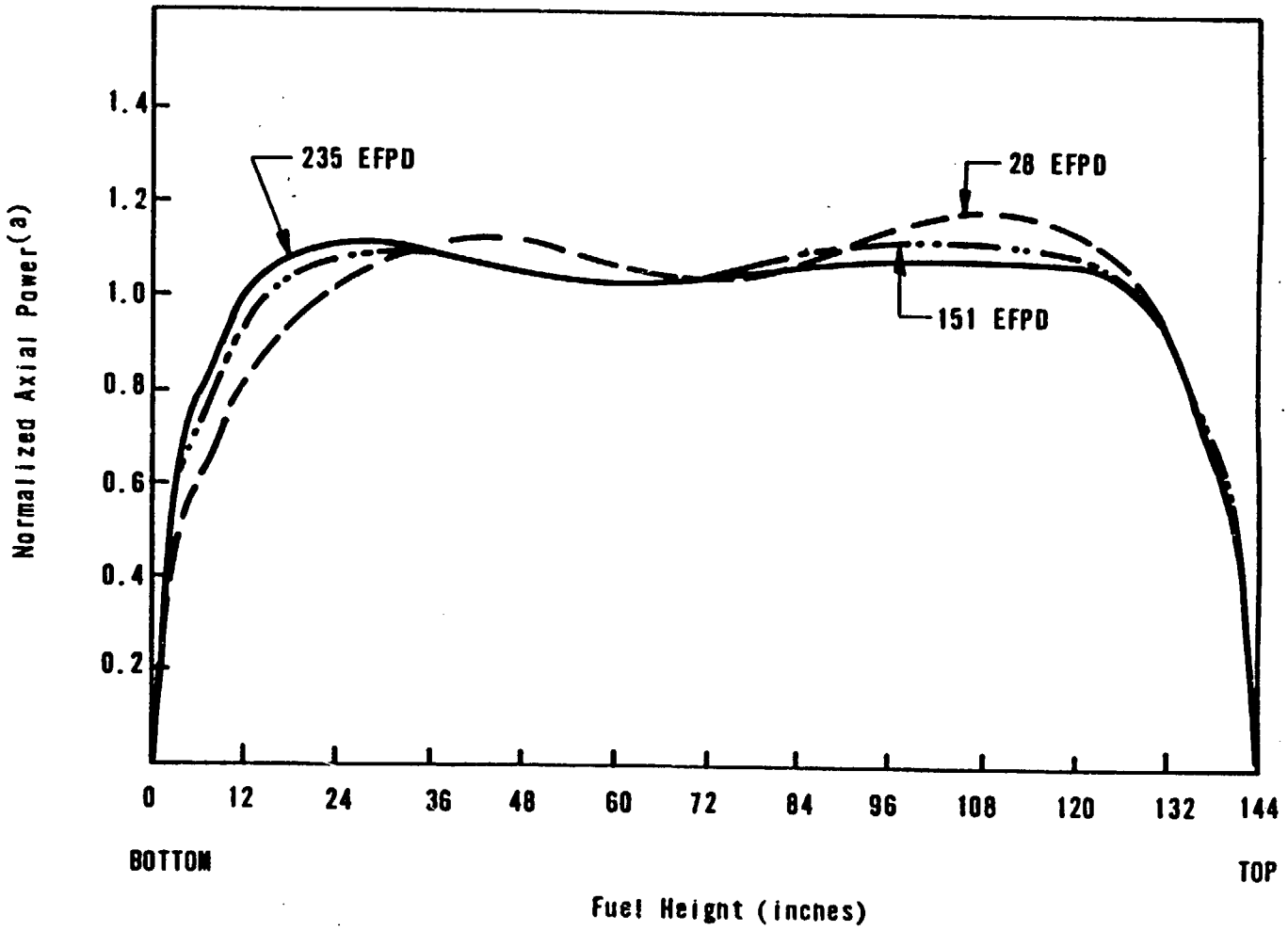

(a)NORMALIZED TO AN AVERAGE VALUE OF 1.0

Figure A-11. Axial Power Profile -- Assembly 1D45, Oconee 1 Cycle 5

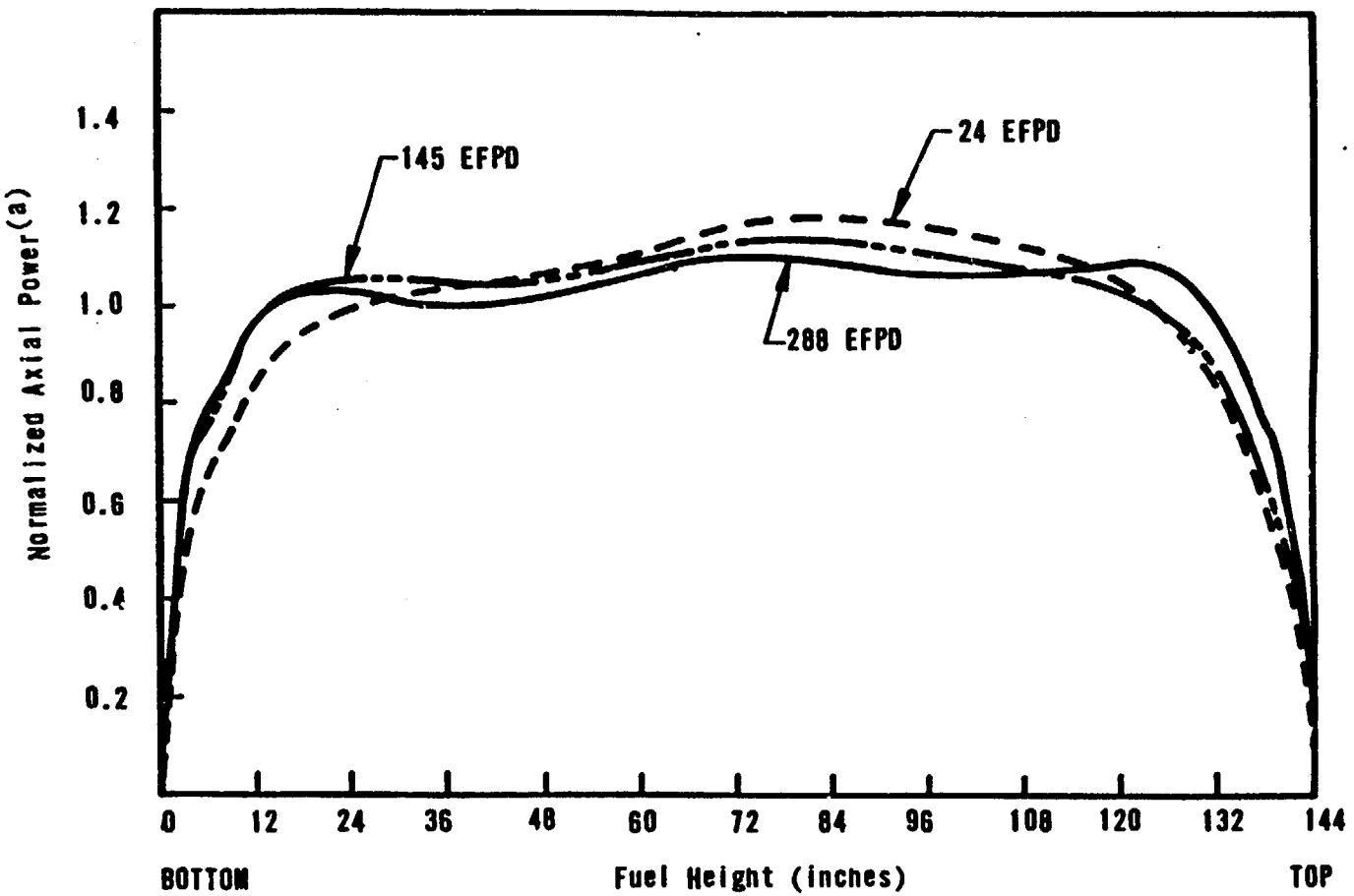

(a)NORMALIZED TO AN AVERAGE VALUE OF 1.0

Figure A-12. Axial Power Profile -- Assembly 1D45, Oconee 1 Cycle 7

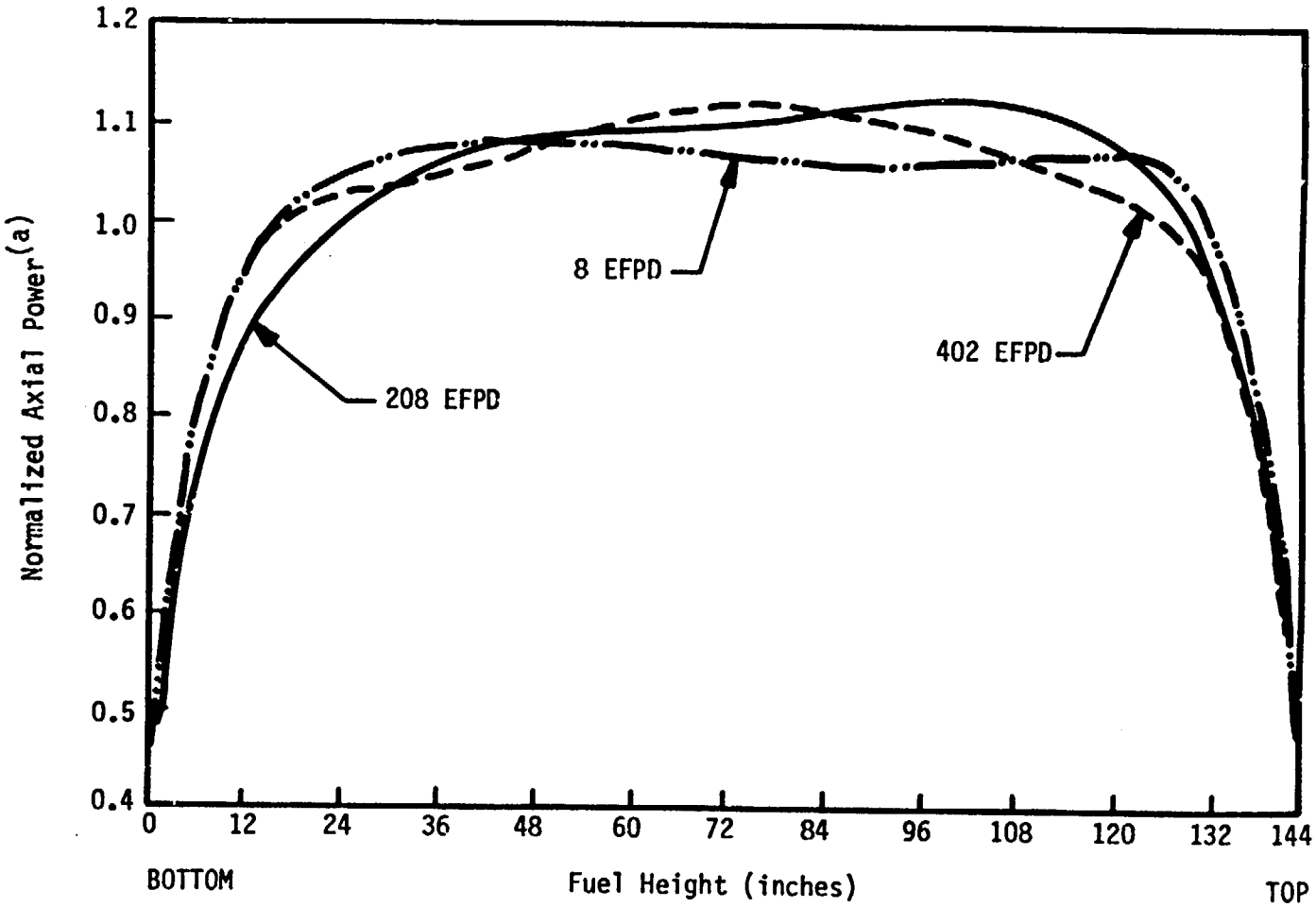

(a)Normalized to an average value of 1.0.

Figure A-13. Fast Fluence ($E > 1.0$ MeV) for Assembly 1D45 (10^{21} n/cm^2), Oconee 1 EOC 7

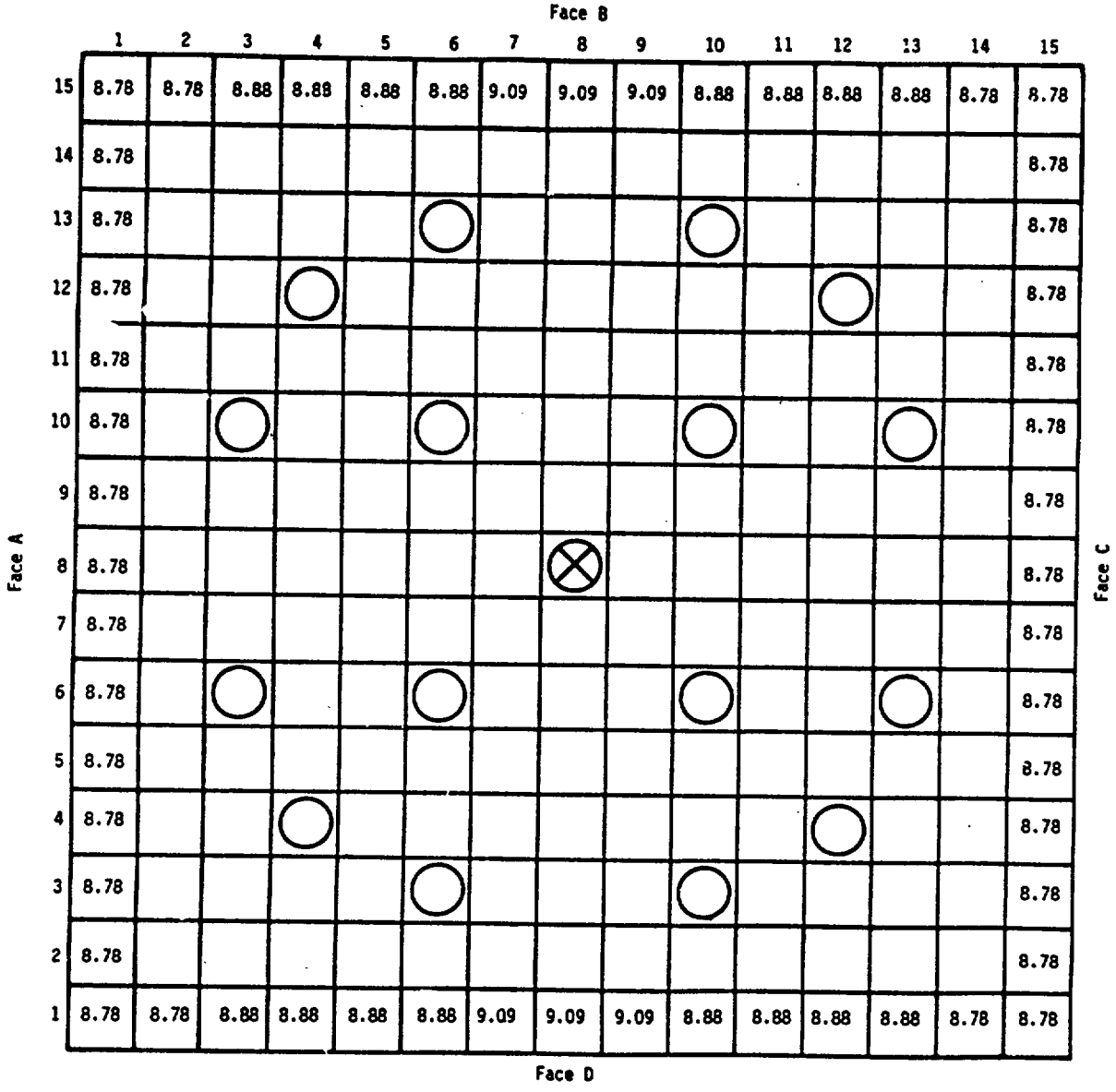

Assembly average fast fluence = 9.17×10^{21} n/cm^2.

APPENDIX B

Tensile Tests of Unirradiated Hydrided Zircaloy-4 Tubing

Tensile properties of unirradiated Zircaloy-4 tubing with nominal hydrogen levels of 15, 150, 400, and 700 ppmH were measured in air at 650F. Specimens were prepared from 20-inch lengths of tubing and etched with circumferential grid lines to allow measuring the final gage length at fracture. Four specimens with each hydrogen level were tested. The specimens with 15 ppmH were taken from standard tubing lot number 3ME13.

The results of the tensile tests at 650F on unirradiated, hydrided tubing are shown in Table B-1. The results indicate that the yield strength, ultimate strength, and uniform plastic strain are not affected by hydrogen content (up to 700 ppmH) in unirradiated Zircaloy-4 tubing. The total elongation and reduction of area are reduced at a hydrogen content above 150 ppmH. The results are illustrated by Figure B-1, which shows uniform elongation and total elongation versus nominal hydrogen content. The uniform elongation remains constant at about 5%, while the total elongation drops from 20% at 150 ppmH to about 15% at 400 ppmH then decreases slowly to 14% at 700 ppmH. The solubility limit at 650F for hydrogen in zirconium is approximately 150 to 200 ppm. The decrease in total elongation is associated with the formation of hydrides (ZrH_2). The effect is more pronounced with increasing volume fraction of the hydrides. The mechanism by which the hydrides reduce to fracture ductility was not investigated in this testing.

Table B-1. 650F Tensile Properties of Hydrided Zircaloy-4 Tubing

Specimen	Yield strength, (0.2% offset) ksi	Ultimate strength, ksi	Uniform plastic strain, %	Total elongation, %	Reduction of cross-sectional area, %
3ME13-9A	55.1	69.6	4.9	20.1	54.4
3ME13-9B	55.8	68.8	5.3	20.1	54.3
3ME13-9C	56.7	69.0	4.5	19.5	56.2
150H-1	53.2	66.5	4.7	21.4	55.7
150H-2	54.9	67.4	5.4	21.4	55.6
150H-3	54.4	67.5	5.1	19.0	55.5
400H-1	62.0	71.5	---	15.3	--
400H-3	59.7	72.1	---	14.7	--
400H-5	58.8	70.9	---	14.5	--
400H-7	55.4	68.9	---	15.9	--
700H-1	55.8	72.8	5.0	13.0	30.0
700H-2	53.6	69.9	5.1	14.3	38.5
700H-3	58.3	76.6	4.9	13.6	31.0

Strain rate through ultimate load = 0.005/min.
Initial gage length = 2.0 inch.
Nominal wall thickness = 0.0265 inch.

Figure B-1. Elongation Vs Hydrogen Content (Zircaloy-4 Tensile Tests Results at 650F)